Université du Québec
INRS Institut national de la recherche scientifique

Énergie Matériaux Télécommunications

EFFECT OF ION IRRADIATION ON THE MICROSTRUCTURE AND PHYSICAL PROPERTIES OF NANOPARTICLES

Par

Chao Wang

Thèse présentée pour l'obtention du grade de

Philosophiae Doctor (Ph.D.)

en sciences de l'énergie et des matériaux

Jury d'évaluation

Président du jury et examinateur interne	Emanuele Orgiu INRS-EMT, Université du Québec
Examinateur externe	Mohamed Siaj Université du Québec à Montréal
Examinateur interne	Rafik Naccache Concordia University
Directeur de recherche	Federico Rosei INRS-EMT, Université du Québec

© Droits réservés de Chao Wang, 2021

ACKNOWLEDGEMENTS

First, I would like to especially thank my supervisor Prof. Federico Rosei, who gave me the possibility of working within his dynamic and productive research group. I am extremely grateful for his unconditional support for providing me with opportunities to attend international conferences and seminars. He guided me through the whole journey of study and research. Under his supervision, I not only made progress in the academic field but also developed and polished my personality. Without Federico, I would not be able to accomplish my goal.

I would like to express my sincere gratitude to my group leader Dr. David Barba for many discussions about the project. His help on ion implantation and photoluminescence measurements was most appreciated. Besides, he gave me a bunch of suggestions in terms of study field that I need to explore deeper and academic direction that I need to work toward more. A special thank to Prof. Haiguang Zhao, who provide me quantum dots for radiation experiments. I would like to thank him for the meaningful comments and guidance.

I would like to thank my collaborators, Dr. Hui Zhang, Jiabin Liu, Dr. Xin Tong, Dr. Gurpreet Singh Selopal, and Dr. Mert Celikin for inspiring discussions and constant supports. I would also thank all the Nano-Femto Lab (NFL) group members.

I also thank all staff at INRS-EMT, particularly Christophe Chabanier, Tatiana Brahmi, Helene Sabourin, Michelle Marcotte, Louise Hudon, and Sylvain Gingras. Besides, I am grateful to Jean-Philippe Masse for training on focused ion beam.

I would like to express my appreciation to my friends at INRS-EMT center, Daling Cu, Yang Fan, Shengyun Huang, Xin Chai, Xin Jin, Xiaohua Yang, and many others for all the fun we had in the past five years.

Last but not least, special thanks to my parents. Thank them for the patience and understanding they have shown me even in the most difficult periods.

ABSTRACT

Irradiation of solids with energetic particles, such as electrons or ions, gives rise to the formation of atomic defects that can strongly modify the properties of materials. Both the understanding and the quantification of the effects induced by these radiations in nanostructured semiconductors provide physical insights and relevant information regarding their structural integrity, tunability, long-term degradation, and stability for numerous applications in materials science and optoelectronics. Beyond the natural protection provided by the Earth's atmosphere, various types of ionizing radiation (mainly composed of protons, alpha particles, gamma, and X-rays) can be encountered. This kind of environment is usually known to disrupt electronic systems and instrumentation. Therefore, it is important to evaluate the change in performance and test the stability of any system based on advanced materials.

In the first part of this thesis, proton irradiation experiments were performed on "giant" core-shell (g-CS) CdS/CdSe quantum dots (QDs) using low-energetic (< 10 keV) ion beams. A simple three-layer model was built for Stopping and Range of Ions in Matter (SRIM) simulations. It shows that 1.5 and 10 keV proton irradiations create almost the same rate of vacancies inside the CdSe core, while 1.5 keV proton irradiation creat 30% higher vacancies in the CdS shell than that of 10 keV protons. The density of nanocavities observed by transmission electron microscopy (TEM) was found to be consistent with the rate of vacancies generated during irradiation. Both the photoluminescence (PL) intensity and lifetime of QDs decrease after irradiation. By comparing the measurements obtained for experiments conducted with ion beams of 1.5 keV and 10 keV, the reduction of these two parameters appears to vary linearly with the concentration of surface defects/traps

created by impinging protons into the CdS shell. The I-V curves of QDs deposited on Si and irradiated with 1.5 and 10 keV H^+ show that the semiconductor bandgaps and the charge carrier exchanges inside and outside QDs differ from the I-V response of the substrate. Proton irradiation can be implemented to enhance photocurrent generation in g-CS QDs.

In the second part, a detailed description of the atomic structure of $CuInSe_xS_{2-x}$/CdSeS/CdS QDs and the effect of e-beam irradiation is presented. Size, three-dimensional (3D) shape, and inner structure of the formed hetero-QDs were characterized through in-depth high-resolution transmission electron microscopy (HRTEM). An epitaxial growth mechanism of the hetero-QDs was proposed, based on monitoring particle morphology and size at different stages of their growth process. The epitaxial relationship between the $CuInSe_xS_{2-x}$/CdSeS core and CdS shell was determined to be $[110]_{\mathrm{core}}//[110]_{\mathrm{shell}}$, $\{112\}_{\mathrm{core}}//\{111\}_{\mathrm{shell}}$. In addition, *in situ* HRTEM observations show that the screw dislocation inside the hetero-QDs can be efficiently repaired by e-beam irradiation (~ 15 min), whereas the stacking fault remains unchanged, even after 20 min of e-beam exposure.

In the last part, Er/Si nanoparticles (NPs) were synthesized in co-implanted fused silica after thermal annealing between 1000 ^oC and 1200 ^oC. TEM images show that the diameter of the formed NPs increases with temperature. At 1000°C and 1100 ^oC, the implanted Si and Er were found to nucleate separately, leading to stronger photoemission signals in both visible (VIS) and near-infrared (NIR) spectral ranges. At 1200 ^oC we observed nanoscale aggregates that are less optically active due to the formation of $ErSi_2$ NPs in localized sample regions. PL measurements conducted on samples exposed to

proton beam aiming at reproducing space radiative environment in vacuum chamber show that the optical emission of hybrid systems containing Er-np and Si nanocrystals (NCs) is more intense and survives longer to ion-induced damaging than unmixed nanoclusterized systems. These results can be described in terms of an increase of the photocarrier transfer occurring between Si NCs and NIR Er emitting levels, which partially compensates for the optical losses induced by structural damage.

Keywords: ionizing radiation; ion implantation; nanoparticles; quantum dots; microstructure; crystal defects; photoluminescence; photocurrent; transmission electron microcopy.

RÉSUMÉ

L'irradiation des solides par des particules de haute énergie (par exemple des électrons ou des ions) génère des défauts atomiques qui modifient considérablement les propriétés physiques du matériau. La compréhension et la quantification des effets induits par de tels rayonnements dans les semi-conducteurs nanostructurés apportent des informations utiles pour de nombreuses applications en science des matériaux, optoélectronique, technologie spatiale et la conversion d'énergie. Plusieurs types de rayonnements ionisants, composés principalement de protons, de particules alpha, de rayons gamma et de rayons X, sont rencontrés en dehors de la protection naturelle fournie par l'atmosphère terrestre. Ces derniers détériorent les systèmes électroniques et les instruments équipant les satellites et autres modules lancés dans l'espace. C'est pourquoi, il est très important de connaître leurs effets sur la performance et la stabilité des matériaux avancés employés dans ces systèmes embarqués.

Dans la première partie de cette thèse, des points quantiques (QDs) de CdSe enrobés d'une fine couche de CdS ont été exposés à des faisceaux de protons visant à reproduire les conditions rencontrées dans l'espace. Un modèle à trois couches a été développé pour simuler l'effet de ces radiations au niveau de la structure atomique du matériau-cible, à l'aide du logiciel Stopping and Range of Ions in Matter (SRIM). Nos résultats montrent qu' en faisant varier l'énergie d'accélération des protons incidents, il est possible de modifier la concentration relative de défauts structurels induits séparemment dans le cœur de CdSe et la couche de CdS. Alors que la proportion de lacunes générées dans le cœur de CdSe par des faisceaux de 1.5 keV et 10 keV reste inchangée , nous montrons que celle-ci est de 30% plus élevée dans la couche de CdS pour des protons de 1.5 keV

En faisant varier la dose d'irradiation, nous mettons en évidence la formation de nanocavités à l'aide d'un microscope électronique à transmission (TEM). Leur vitesse de formation est conforme aux taux de décapage ionique calculés dans le matériau-cible, à partir des paramètres de faisceaux que nous avons employés. L'intensité de photoluminescence (PL) et la durée de vie des émissions lumineuses provenant des QDs étudiés diminuent après irradiation. En comparant les mesures effectuées avec des faisceaux ioniques de 1.5 et 10 keV, il apparaît que la réduction de ces deux quantités varie linéairement avec la concentration de défauts générés par les protons incidents dans la couche externe de CdS. Des mesures de courant-tension effectués sur des points quantiques déposés sur un substrat de Si, montrent comment la bande interdite du semi-conducteur et le transfert des porteurs de charge à l'intérieur et à l'extérieur des QDs sont affectés par les irradiations.

La deuxième partie de ce travail décrit en détail la structure atomique de points quantiques de $CuInSe_xS_{2-x}$/CdSeS/CdS et s'intéresse aux effets de faisceau d'électrons sur leur microstructure. La taille, la morphologie tridimensionnelle et la structure interne des points quantiques hétérogènes préparés sont caractérisés par microscopie électronique en transmission de haute résolution (HRTEM). En étudiant la morphologie et la taille des particules formées à différents stades de leur synthèse, un mécanisme de croissance épitaxiale est proposé pour la formation de ces hétérostuctures quantiques. L'alignement des couches atomiques composant le noyau de $CuInSe_xS_{2-x}$/CdSeS et la couche-coquille de CdSe est déterminée comme suit: $[110]_{\text{noyau}}//[110]_{\text{coquille}}$, $\{112\}_{\text{noyau}}//\{111\}_{\text{coquille}}$. Au moyen d'observations HRTEM *in situ*, nous montrons qu'une irradiation par faisceau d'électrons de 200 kV permet de réparer efficacement les

dislocations structurelles au sein de ces hétérostructures au bout de 15 minutes, mais que les défauts d'empilement restent toujours inchangés après 20 minutes d'exposition.

Dans la dernière partie, des nanoparticules (NPs) Er/Si ont été synthétisées dans une matrice de silice fondue par implantations ioniques successives de Si et d'Er, suivies de recuits effectués entre 1000 °C et 1200 °C. Les images TEM montrent que le diamètre des NPs formés augmente avec la température. À 1000 °C et 1100 °C, le Si et Er implantés se sont nucléés séparément, conduisant à des émissions PL plus intenses dans les gammes spectrales visible (VIS) et proche infrarouge (NIR). A 1200 ℃, on a observé des agrégats à l'échelle nanométrique ayant une faible activité optique due à la formation de nanoparticules de $ErSi_2$. Les mesures effectuées sur des échantillons exposés à différents faisceaux de protons, visant à reproduire en laboratoire les conditions radiatives rencontrées dans l'espace, ont montré que les systèmes hybrides contenant des nano-cristaux de silicium (NCs) et des Er-np émettent plus de lumière et survivent plus longtemps aux effets induits par ce type d'irradiations. Ces propriétés peuvent être associées à une augmentation des transferts de charges entre nanocristaux de Si et nanoparticules d'Er, qui compensent une partie des pertes de lumière résultant des dommages structurels.

Mots clefs: radiation ionisante; implantation ionique; nanoparticules; points quantiques; microstructure; défaut cristallin; photoluminescence; photocourant; microscopie électronique en transmission.

CONTENTS

ACKNOWLEDGEMENTS ..... **III**

ABSTRACT ..... **V**

RÉSUMÉ ..... **IX**

CONTENTS ..... **XIII**

LIST OF FIGURES ..... **XVII**

LIST OF TABLES ..... **XXIII**

LIST OF EQUATIONS ..... **XXV**

LIST OF ABBREVIATIONS ..... **XXVII**

1 INTRODUCTION **1**

1.1 IONIZING RADIATION 1

1.1.1 Types of ionizing radiation *1*

1.1.2 Natural background radiation in space *3*

1.1.3 Artificial radiation on the Earth *4*

1.2 INTERACTION OF IONIZING RADIATION WITH MATTER 4

1.2.1 Heavy ions *7*

1.2.2 Light ions *7*

1.3 ION IMPLANTATION 8

1.3.1 Depth-distribution of implanted ions *8*

1.3.2 Plasma source and beam ion implantations *10*

1.3.3 Application of ion implantation *11*

1.4 NANOPARTICLES 13

1.4.1 Colloidal quantum dots *13*

1.4.2 Si nanoparticles *14*

1.5 EFFECT OF IONIZING IRRADIATION ON THE NANOPARTICLES 15

1.5.1 The morphological evolution of nanoparticles under radiation *15*

1.5.2 Effect of ionizing irradiation on optical properties *17*

1.6 RESEARCH OBJECTIVES AND ORGANIZATION 18

1.6.1 Research objectives *18*

1.6.2 Thesis organization *20*

2 EXPERIMENT METHODS **23**

2.1 ION IMPLANTATION PROCESS 23

2.2 SRIM-TRIM SIMULATIONS 25

2.3 FOCUSED ION BEAM 27

2.3.1 Sputtering process *28*

2.3.2 Steps to prepare TEM sample using FIB *29*

2.4 Characterization methods 31
2.4.1 Transmission electron microscopy 31
2.4.2 Energy-dispersive X-ray spectroscopy 36
2.4.3 Optical properties measurements 37
2.4.4 X-ray photoelectron spectroscopy 39
2.4.5 Ellipsometry 40
2.5 Sample preparation 41
2.5.1 Colloidal QDs for ion irradiation and optical measurements 41
2.5.2 Samples for current-voltage measurements 42
2.5.3 Synthesis of Er/Si NPs embedded SiO_2 layer 43
2.6 Data analysis 44

3 EFFECT OF PROTON IRRADIATION ON CORE/SHELL QUANTUM DOTS 47
3.1 Motivation 47
3.2 SRIM simulations for irradiation damage on g-CS QDs 48
3.2.1 Simulations for g-CS QDs under H^+ irradiation 48
3.2.2 Simulations for g-CS QDs under He^+ irradiation 51
3.3 Structural damages arise from proton irradiation 53
3.3.1 TEM analysis of QDs after proton irradiation 53
3.3.2 Formation of nanocavities inside QDs 57
3.4 Effects of proton irradiation on optical properties of g-CS QDs 57
3.4.1 Evolution of PL emission after irradiation 57
3.4.2 Evolution of PL lifetime after irradiation 60
3.5 Effects of protons irradiation on photocurrent of g-CS QDs 64
3.5.1 Photoelectric properties analysis 64
3.5.2 Bandgap alignment in MoO_3/QDs/Si systems 68
3.5.3 Photocarrier transfer between different layers 70
3.5.4 Enhanced photocurrent in MoO_3/QDs/Si systems 72
3.6 Summary 74

4 EPITAXIAL GROWTH OF HETEROSTRUCTURED QUANTUM DOTS AND DEFECTS REPAIR BY E-BEAM 75
4.1 Motivation 75
4.2 Morphology of $CuInSe_xS_{2-x}$/CdSeS/CdS hetero-quantum dots 76
4.2.1 2D outlines of hetero-QDs in TEM 76
4.2.2 Hetero-QDs observed along different zone axes 78
4.3 Growth mechanism of hetero-quantum dots 80
4.3.1 Growth of hetero-QDs 80
4.3.2 Epitaxial relationship between core and shell 83

4.4 DEFECTS IN CISESS/CDSES/CDS HETERO-QDS 85

4.4.1 Stacking faults and twin boundaries 85

4.4.2 Screw dislocations repaired by e-beam irradiations 86

4.5 THE TEMPERATURE UNDER E-BEAM IRRADIATION 87

4.6 SUMMARY 89

5 ENHANCED RADIATION RESISTANCE OF PHOTOLUMINESCENCE EMISSION INDUCED BY NANOCLUSTERING 91

5.1 MOTIVATION 91

5.2 DISTRIBUTION OF SI AND ER IN SiO_2 LAYER 92

5.3 MORPHOLOGICAL AND MICROSTRUCTURAL INVESTIGATIONS 94

5.3.1 Morphology of the NPs after annealing 94

5.3.2 Microstructure and composition of the NPs after annealing 97

5.3.3 Chemical composition analysis by EDS line scans 99

5.4 SRIM SIMULATIONS FOR PROTON IRRADIATION 100

5.5 PHOTOLUMINESCENCE MEASUREMENTS 104

5.5.1 PL intensity after annealing 104

5.5.2 Degradation of PL intensity after proton irradiation 106

5.5.3 Absorbance spectra before and after proton irradiation 108

5.6 PHENOMENOLOGICAL ANALYSIS ABOUT THE ENHANCED PL EMISSION 109

5.6.1 Degradation of PL under proton irradiation 109

5.6.2 Photocarriers transfer between Si and Er NPs 111

5.7 SUMMARY 112

6 CONCLUSIONS AND PERSPECTIVES 115

6.1 CONCLUSIONS 115

6.2 PERSPECTIVES 118

7 BIBLIOGRAPHY 121

8 ANNEXE I 139

8.1 THE STOPPING AND RANGE OF IONS IN MATTER SOFTWARE 139

8.2 DIGITALMICROGRAPH™ SCRIPTING 141

9 ANNEXE II 142

SOMMAIRE RÉCAPITULATIF 142

LIST OF FIGURES

FIGURE 1.1 CATEGORIZATION OF NON-IONIZING AND IONIZING RADIATION.[1] 1

FIGURE 1.2 SEVERAL TYPES OF IONIZING RADIATION AND THEIR INTERACTION WITH MATTER. THE PATHS OF ALPHA, BETA, NEUTRON PARTICLES ARE INDICATED BY SOLID STRAIGHT LINES AND GAMMA RAYS ARE REPRESENTED BY WAVY LINES. THE IONIZATION THAT OCCURS INSIDE THE MATERIALS IS INDICATED BY UNFILLED CIRCLES.[6] 2

FIGURE 1.3 ALTITUDE OF VAN ALLEN RADIATION BELTS AROUND THE EARTH.[14] 4

FIGURE 1.4 ELASTIC COLLISION BETWEEN TWO ATOMS. 5

FIGURE 1.5 BRAGG CURVE FOR PROTONS IN RELATIVE STOPPING POWER; THE SHARP DEPOSITION OF ENERGY SHOWN IN THE CURVE IS KNOWN AS THE BRAGG PEAK.[6] 6

FIGURE 1.6 SCHEMATIC DIAGRAM OF PLASMA SOURCE ION IMPLANTATION[44] 11

FIGURE 1.7 EMISSION COLORS AND PL SPECTRA OF CDSE QDS. THE SIZE OF QDS RANGING FROM ~1NM TO ~10 NM[66] 13

FIGURE 1.8 THE EXCITATION AND RELAXATION PROCESSES OF ELECTRONS IN (A) DIRECT AND (B) INDIRECT BAND GAP MATERIALS. THE PHONON-ASSISTED PROCESS IS SEEN IN THE LATTER CASE IN ORDER TO CONSERVE THE MOMENTUM CHANGE.[91] 14

FIGURE 1.9 THE SHAPE EVOLUTION OF AU NPS AS A FUNCTION OF INITIAL SIZE AND IRRADIATION FLUENCE. THE SCALE BAR IN (A) IS 20 NM. SAMPLES (B1), (D1), AND (F1) ARE PREIRRADIATED BY AU IONS AT 5×10^{15} IONS/CM^2 WITH ENERGY OF 4 MEV. SAMPLE (A2) TO (F2) ARE IRRADIATED BY KR IONS AT 10^{14} IONS/CM^2 WITH ENERGY OF 74 MEV. SAMPLE (A2) TO (F2) HAVE BEEN IRRADIATED BY KR IONS AT 5×10^{14} IONS/CM^2 WITH ENERGY OF 74 MEV.[107] 16

FIGURE 2.1 SCHEMATIC DIAGRAM OF ION IMPLANTATION SYSTEM IN OUR LAB 23

FIGURE 2.2 SCHEMATIC DIAGRAM OF ION BEAM SYSTEM. 25

FIGURE 2.3 RADIO-FREQUENCY PLASMA SOURCE 25

FIGURE 2.4 ELECTRONIC AND NUCLEAR STOPPING POWER AS A FUNCTION OF ION ENERGY FOR PROTON 26

FIGURE 2.5 SCHEMATIC DIAGRAM OF THE SPUTTERING PROCESS IN FIB. ENERGETIC GA^+ HAS COLLISIONS WITH THE SURFACE OF THE SAMPLE AND SPUTTER THE MATERIAL.[127] 29

FIGURE 2.6 STEP TO PREPARE THIN TEM SAMPLES THROUGH FIB MILLING. (A) DEPOSIT PROTECTING LAYER OF TUNGSTEN, (B) MILL TRENCH AROUND THE DESIRED LOCATION, C) SEPARATE SAMPLE FROM THE BULK MATERIAL BY U-CUT, (D) IN-SITU LIFT-OUT SAMPLE BY MICROMANIPULATOR, (E) TRANSFER THE SAMPLE TO TEM GRID AND FIX IT BY TUNGSTEN, (F) POLISH THE SAMPLE UNTIL THIN ENOUGH FOR ELECTRON TRANSPARENCY.[128] 30

FIGURE 2.7 SCHEMATIC DIAGRAM SHOWS TWO BASIC IMAGING MODES IN THE TEM. (A) IMAGE MODE AND (B) DIFFRACTION MODE. 33

FIGURE 2.8 SCHEMATIC DIAGRAM SHOWS THE DETECTOR SETUP FOR HAADF ADF AND BF IMAGES.[129] 35

FIGURE 2.9 SCHEMATIC DIAGRAM OF THE PRINCIPLE OF EDS. 36

FIGURE 2.10 (A) PRINCIPLE OF THE PHOTOLUMINESCENCE PROCESS; (B) SCHEMATIC DIAGRAM OF SETUP FOR PL MEASUREMENTS. 37

FIGURE 2.11 (A) MEASUREMENT OF START AND STOP TIMES BY TCSPC; (B). TYPICAL HISTOGRAM MEASURED BY TCSPC.[135] 38

FIGURE 2.12 SCHEMATIC DIAGRAM OF PHOTOELECTRON GENERATION. 39

FIGURE 2.13 SCHEMATIC DIAGRAM OF SETUP FOR ELLIPSOMETRY MEASUREMENTS. 40

FIGURE 2.14 FILM THICKNESS PROFILE MEASURED BY PROFILOMETRY. 41

FIGURE 2.15 SCHEMATIC DIAGRAM OF THE DEVICE FOR I-V MEASUREMENTS. 43

FIGURE 2.16 CROSS-SECTIONAL HAADF IMAGE OF SILICON SUBSTRATE WITH ~ 200 NM SiO_2 LAYER AFTER THERMAL OXIDATION. 44

FIGURE 3.1 THREE-LAYER MODEL FOR SRIM-TRIM SIMULATIONS, THE THICKNESS OF EACH LAYER IS 3 NM 48

FIGURE 3.2 VACANCY DISTRIBUTION CALCULATED FROM SRIM-TRIM SIMULATIONS, INSIDE G-CS QDS EXPOSED TO 1.5 KEV (A) AND 10 KEV (B) PROTON BEAMS. 49

FIGURE 3.3 VACANCY DEPTH-DISTRIBUTION CALCULATED FROM SRIM-TRIM SIMULATIONS, INSIDE TWO STACKED G-CS QDS EXPOSED TO 1.5 KEV (A) AND 10 KEV (B) PROTON BEAMS. 50

FIGURE 3.4 IMPLANTATION DEPTH-PROFILES OF H^+ AND He^+ WITH DIFFERENT ENERGY ARE CALCULATED BY SRIM-TRIM SIMULATIONS. THE TARGET MATERIAL IS CDS WITH A DENSITY OF 4.82 G/CM^3. 51

FIGURE 3.5 VACANCY DISTRIBUTION OF G-CS QDS EXPOSED TO 3.1 KEV (A) AND 10 KEV (B) He^+ IRRADIATION, WHICH IS CALCULATED BY SRIM SIMULATIONS. 52

FIGURE 3.6 BF IMAGES, HRTEM IMAGES AND INTENSITY PROFILES OF G-CS QDS: (A) AND (B) BEFORE IRRADIATION; (C) AND (D) AFTER 1.5 KEV PROTON IRRADIATION AT 1×10^{17} H^+/CM^2; (E) AND (F) AFTER 10 KEV PROTON IRRADIATION AT 1×10^{17} H^+/CM^2. 54

FIGURE 3.7 TEM IMAGES OF G-CS QDS AFTER 10 KEV H^+ IRRADIATION SHOWING THE EVOLUTION OF THE QDS STRUCTURE FOR FLUENCES OF 1×10^{16} H^+/CM^2 (A), 5×10^{16} H^+/CM^2 (B) AND 1×10^{17} $H+/CM^2$ (C), RESPECTIVELY. 55

FIGURE 3.8 TEM IMAGES AND SKETCHES OF G-CS QDS AFTER 10 KEV PROTON IRRADIATION WITH FLUENCE OF 1×10^{16} H^+/CM^2 (A, D), 5×10^{16} H^+/CM^2 (B, E) AND 1×10^{17} H^+/CM^2 (C, F), RESPECTIVELY. 56

Figure 3.9 Evolution of the absorption and PL spectral emission in g-CS QDs exposed to1.5 keV (a) and 10 keV (b) proton irradiation, with the dose-dependence of the PL signal integrated between 550 and 700 nm (c), and as plotted as a function of the variation in CdS shell vacancy surface concentration calculated by SRIM (d). 58

Figure 3.10 Evolution of PL spectral emission for CdSe QDs exposed to 20 keV proton beam. 59

Figure 3.11 Evolution of the PL decay. g-CS QDs under 1.5 keV (a) and 10 keV (b) proton irradiation; (c) dose-dependence of PL lifetime and its variation upon the surface density of CdS shell vacancies calculated by SRIM (d). 61

Figure 3.12 Evolution of the absorption spectral. g-CS QDs under 1.5 keV (a) and 10 keV (b) proton irradiation. 62

Figure 3.13 Evolution of K_{ET} and K_{NET} of g-CS QDs under proton irradiation. 63

Figure 3.14 Mo $3d_{5/2}$ and $3d_{3/2}$ XPS peaks of MoO_3 films covering QD/Si implanted at 10 kV with $1x10^{16}$ H^+/cm^2 (a) and non-implanted QD/Si (b). 65

Figure 3.15 I-V characteristics of MoO_3/QDs/Si and MoO_3/Si under dark and illumination, for QDs implanted at 1.5 kV (a) and 10.0 kV (b), as well as Si substrates implanted at 1.5 kV (c) and 10.0 kV (d). 67

Figure 3.16 (a) Schematic bandgap alignment along the Fermi level in MoO_3/QD/Si systems containing g-CS QDs, (b) donor/acceptor redistribution at CdS/Si-H and Si-H/Si interfaces leading to local electric fields E_1 and E_2. (c) Equivalent potential downshift, Φ given upon $E = E_1 - E_2$ and the biased voltage, VBIAS, with the enhanced photovoltaic process due to the delocalization of conduction electrons in the g-CS system. 68

Figure 3.17 (a) UPS analysis of the reference Si substrate and Si implanted with 10 keV protons at ion doses of $2x10^{15}$ H^+/cm^2 and $1x10^{16}$ H^+/cm^2. Secondary electron cut-off (a) and valence band edge (b) regions. 70

Figure 4.1 BF image (a), XRD pattern (b), UV-VIS and PL spectrum (d) of CISeS/CdSeS/CdS hetero-QDs, (c) corresponds to the rectangular region in (a), inset of (b) is the SAED pattern........ 76

Figure 4.2 PL spectra of heterostructured CISeS/CdSeS/CdS g-QDs at different growth stages. 78

Figure 4.3 HRTEM images of CISeS/CdSeS/CdS hetero-QDs. Each of the four panels (a-d) is composed of one representative HRTEM image for an isolated QD with a given projection, the corresponding FFT pattern of the HRTEM image (inset), the sketches and the atomic model. The detailed rotation modes between different zone axes are indicated by the blue arrows. (a)-(d) show the QDs viewed along <111>, <112>, <110> and <001> zone axes, respectively. 79

FIGURE 4.4 (A) HRTEM IMAGE OF CISES CORE; (B-D) HRTEM IMAGES OF THE HETERO-QDS FORMED AT DIFFERENT GROWTH STAGES........ 80

FIGURE 4.5 SAED OF HETEROSTRUCTURED CISES/CDSES/CDS G-QDS AT DIFFERENT GROWTH STAGES. (A) CUINSES QDS, (B) (C) AND (D) IS THE PRODUCTS AFTER INJECTION CD/S PRECURSOR OF 2.5 ML, 4 ML, AND 20 ML, RESPECTIVELY. 81

FIGURE 4.6 EDS SPECTRA OF HETEROSTRUCTURED CISES/CDSES/CDS G-QDS AT DIFFERENT GROWTH STAGES. 82

FIGURE 4.7 (A) IS THE UNIT CELL OF CISES, CDSES, AND DOUBLE UNIT CELL OF CDS; (B) THE INTERFACE OF THE CISES, CDSES, AND CDS VIEWED ALONG <110> ZONE AXIS. 83

FIGURE 4.8 HRTEM IMAGES OF CISES/CDSES/CDS HETERO-QDS. (A) PERFECT HETERO-QDS, (B) HETERO-QDS WITH STACKING FAULTS, (C) HETERO-QDS WITH TWIN BOUNDARIES, AND (D) FFT FILTERED IMAGE OF (C). 85

FIGURE 4.9 EVOLUTION OF DEFECTS UNDER E-BEAM EXPOSURE OBSERVED BY *IN SITU* HRTEM. (A) HRTEM IMAGE OF HETERO-QDS AT THE BEGINNING; (B), (C), (D), AND (E) ARE HETERO-QDS UNDER E-BEAM EXPOSURE OF 5 MIN, 10 MIN, 15 MIN, AND 20 MIN, RESPECTIVELY; (D) CORRESPONDS TO THE RECTANGULAR REGION IN (A). THE RADIUS OF E-BEAM DURING OBSERVATION IS ~30 NM........ 87

FIGURE 4.10 EVAPORATION OF HETERO-QDS AND CARBON FILM UNDER E-BEAM EXPOSURE. (A) HETERO-QDS BEFORE STRONG E-BEAM IRRADIATION, (B)-(E) HETERO-QDS AFTER 5S(B), 20S(C), 30S(D) AND 60S(E) E-BEAM IRRADIATION. THE RADIUS OF E-BEAM FOR IRRADIATION IS ~7 NM. 89

FIGURE 5.1 THE IMPLANTATION DEPTH-PROFILES OF 50 KEV SI AND 150 KEV ER IONS IN SiO_2 SUBSTRATE CALCULATED BY SRIM........ 93

FIGURE 5.2 BF TEM IMAGES OF SAMPLES ANNEALED AT 1000°C (A), 1100°C (B) AND 1200°C (C); WITH THEIR CORRESPONDING HAADF TEM IMAGES (D), (E) AND (F)........ 94

FIGURE 5.3 NANOPARTICLE SIZE-DISTRIBUTION OF SAMPLES ANNEALED AT 1000°C (A), 1100°C (B), AND 1200°C (C). 96

FIGURE 5.4 HRTEM IMAGES OF SAMPLES ANNEALED AT 1000°C (A), 1100°C (B) AND 1200°C (C), OBTAINED AT MAGNIFICATIONS OF ×600 000, ×600 000 AND ×400 000, RESPECTIVELY. 97

FIGURE 5.5 (A) AND (C) HRTEM IMAGES OF SAMPLES ANNEALED AT 1200 °C; (B) AND (D) ZOOMED IMAGES AT A MAGNIFICATION OF X 500 000, CORRESPONDING TO RECTANGULAR REGIONS OF IMAGES (A) AND (C), RESPECTIVELY. 98

FIGURE 5.6 EDS LINE-SCAN OF BRIGHT (A) AND DARK (B) NPS SYNTHESIZED AT 1200°C, SHOWING THE NEIGHBORING FORMATION OF ER-RICH SI-NC (A) AND PURE SI-NC (B). 99

FIGURE 5.7 IMPLANTATION DEPTH PROFILE OF 10 KEV H^+ IS CALCULATED BY SRIM-TRIM SIMULATIONS. THE TARGET MATERIAL IS SiO_2 WITH A DENSITY OF 2.30 G/CM^3. 102

FIGURE 5.8 VACANCY DISTRIBUTION INSIDE SI, ER AND O MIXED LAYER EXPOSED TO 10 KEV H^+ IRRADIATIONS, WHICH IS CALCULATED BY SRIM SIMULATIONS INSIDE A TARGET WHERE THE CONCENTRATION OF SI, O, AND ER IS THE SAME (A), AND THE ATOMIC RATIO BETWEEN ER, SI AND O IS 1:20:20 (B).. 103

FIGURE 5.9 PL SPECTRA OF THE NIR ER EMISSION (A) AND THE VIS SI EMISSION (B). 104

FIGURE 5.10 SCHEMATIC DIAGRAM FOR PHOTODYNAMICS BETWEEN SI AND ER NP. 105

FIGURE 5.11 EVOLUTION OF THE NIR PL SPECTRAL EMISSION OF ER/SI HYBRID SYSTEMS SYNTHESIZED AT 1100^oC UNDER PROTON IRRADIATION (A), WITH THE DOSE-DEPENDENCE OF THEIR CORRESPONDING INTEGRATED SIGNAL (RED SOLID CIRCLES) AND THE DECAY OF PL POWER EXPECTED IN SINGLE SYSTEMS (BLACK OPEN SQUARES) (B). 106

FIGURE 5.12 ABSORBANCE SPECTRA MEASURED BEFORE AND AFTER PROTON IRRADIATION IN PRISTINE FUSED SILICA AND FUSED SILICA WHERE SI-NCS HAVE BEEN PRODUCED BY 50 KEV Si^+ IMPLANTED AT A FLUENCE OF 2.10^{17} Si^+/cm^2. THE INSETS SHOW THE VARIATIONS OF ABSORBANCE AROUND THE LASER WAVELENGTH EXCITATION (405 NM) AND AROUND 1.54 MM (BETWEEN 1510 AND 1580 NM). 109

LIST OF TABLES

TABLE 1.1 PROJECTED RANGE AND STRAGGLE OF DIFFERENT IONS IMPLANTED INTO SI SUBSTRATE................. 9

TABLE 2.1 COMPARISON LIST BETWEEN THE ACCELERATING VOLTAGE, THE WAVELENGTH OF AN ELECTRON, THE VELOCITY OF AN ELECTRON, AND THE RATIO OF THE VELOCITY OF AN ELECTRON TO THE VELOCITY OF LIGHT[129] 32

TABLE 4.1 ATOM CONCENTRATION OBTAINED FROM EDS ANALYSIS. 82

TABLE 5.1 PROJECTED RANGE AND STRAGGLE OF SI AND ER IONS INTO SiO_2 SUBSTRATE............................. 93

TABLE 5.2 ELECTRONIC STOPPING POWER, NUCLEAR STOPPING POWER, PROJECTED RANGE, AND STRAGGLE OF PROTON IMPLANTED IN SiO_2. 101

LIST OF EQUATIONS

$T = \frac{2M_1M_2}{(M_1+M_2)^2}E_i(1 - cos\theta)$	Eq. (1.1)
$N(x) = N_p \exp\left[-\left(x - R_p\right)^2\right]/2\Delta R_p$	Eq. (1.2)
$Q = \int_0^\infty N(x)dx$	Eq. (1.3)
$I_m = k\sqrt{Em}$	Eq. (2.1)
$D = \frac{It}{eS}$	Eq. (2.2)
$N_d = 0 \rightarrow T < E_d$	Eq. (2.3)
$N_d = 1 \rightarrow E_d \leq T < 2E_d$	Eq. (2.4)
$N_d = \frac{\beta T}{2E_d} \rightarrow T < E_d$	Eq. (2.5)
$\delta = \frac{0.61\lambda}{\mu \cdot sin\beta}$	Eq. (2.6)
$\lambda_e = \frac{h}{\sqrt{2m_0E(1+\frac{E}{2m_0c^2})}}$	Eq. (2.7)
$\sigma_R(\theta) = \frac{e^4Z^2}{16(4\pi\varepsilon_0E_0)^2}\frac{d\Omega}{sin^4(\frac{\theta}{2})}$	Eq. (2.8)
$\tau = \frac{\sum a_i\tau_i^2}{\sum a_i\tau_i}$	Eq. (2.9)
$E_B = E_P - (E_k + \phi)$	Eq. (2.10)
$\rho = \frac{R_p}{R_s} = \tan(\Psi)e^{i\cdot\Delta}$	Eq. (2.11)
$\mathrm{QY} = \frac{K_{et}}{K_{et}+K_{net}}$	Eq. (3.1)

$\tau = \frac{1}{K_{et}+K_{net}}$ Eq. (3.2)

$V = \frac{\sqrt{2}}{12} a^3$ Eq. (4.1)

$t/\lambda = \ln{(I_t/I_0)}$ Eq. (5.1)

$D = 1.602 \times 10^{-10} \Phi \frac{dE}{dx}$ Eq. (5.2)

$I = \tau_{PL} N_{ph}^{Er} (1 - \alpha)$ Eq. (5.3)

$\alpha = a \ \frac{n_{rec.}}{n} D$ Eq. (5.4)

$N_{ph}(D) = N_{ph}^{Er} + N_{ph}^{trans}(D)$ Eq. (5.5)

$\frac{I(D)}{I_0} \propto [1 + \beta(D)] e^{-D/\Delta_1}$ Eq. (5.6)

LIST OF ABBREVIATIONS

2D	two-dimensional
3D	three-dimensional
BCA	binary collisions approximation
BF	bright field
BFP	back focal plane
CISeS	$CuInSe_xS_{2-x}$
DF	dark field
DOS	density of states
DP	diffraction pattern
EDFAs	Er-doped fiber amplifiers
EDS	energy dispersive x-ray spectroscopy
FCC	face-centered cubic
FIB	focus ion beam
FFT	fast Fourier transform
GCR	galactic cosmic rays
GEO	geostationary orbit
g-CS	“giant” core-shell
GPS	global positioning system
HAADF	high-angle annular dark-field imaging
HCP	hexagonal-closed-packed
hetero-QDs	heterostructured quantum dots
HRTEM	high-resolution transmission electron microscopy
LED	light-emitting diodes

LEO	low-Earth orbit
LMIS	liquid metal ion source
NBOHC	non-bridging oxygen hole centers
NIR	near-infrared
NPPs	nuclear power plants
NPs	nanoparticles
NRT-dpa	Norgett−Robinson−Torrens displacements per atom
PSII	plasma source ion implantation
PL	photoluminescent
PV	photovoltaics
PVOH	polyvinyl alcohol
QDs	quantum dots
QY	quantum yield
SAED	selected-area electron diffraction
SCR	solar cosmic rays
SEM	scanning electron microscope
SF	stacking fault
SILAR	successive ionic layer adsorption and reaction
SRIM	Stopping and Range of Ions in Matter
TCSPC	time-correlated single-photon counting
TENG	triboelectric nanogenerators
TEM	transmission electron microscopy
TRIM	Transport of Ions in Matter
UV	ultraviolet

VIS	visible spectrum
VLM	visible-light microscope
WZ	wurtzite
XPS	X-ray photoelectron spectrometry
XRD	X-ray diffraction
ZB	zinc blend

1 INTRODUCTION

1.1 Ionizing radiation

1.1.1 Types of ionizing radiation

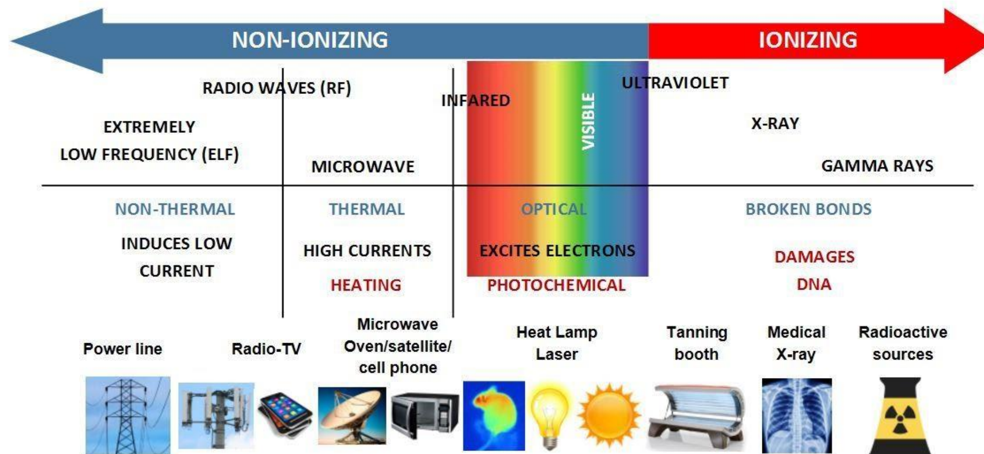

Figure 1.1 Categorization of non-ionizing and ionizing radiation.[1]

Ionizing radiations are energetic particles or electromagnetic waves that can remove one or several electrons from an atom, upsetting the balance between electron and proton and giving the atom a positive charge.[2-3] Figure 1.1 shows the categorization of ionizing and non-ionizing radiation. There are two types of electromagnetic waves which can ionize atoms: gamma-rays and X-rays.[1, 4] Gamma-rays have no mass and no charge, which makes them strong penetrating radiations.[5] X-rays have the same basic properties as gamma-rays, but most X-rays are produced by artificial methods instead of being emitted from radioactive substances. The energy of X-rays is lower than gamma rays. Therefore, they are less penetrating than gamma rays.

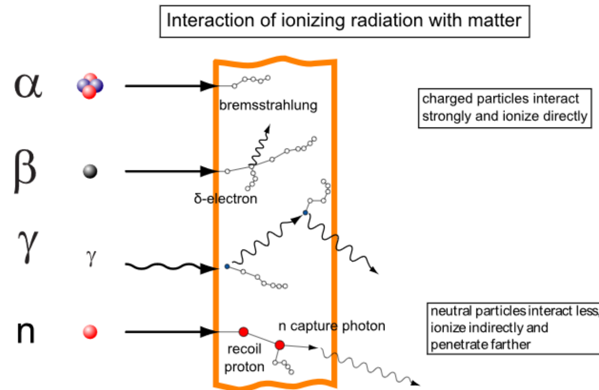

Figure 1.2 Several types of ionizing radiation and their interaction with matter. The paths of alpha, beta, neutron particles are indicated by solid straight lines and gamma rays are represented by wavy lines. The ionization that occurs inside the materials is indicated by unfilled circles.[6]

Besides electromagnetic waves like X-rays or gamma-rays, ionization can also be generated by ion irradiations. Ion irradiation consists of high-speed atomic or subatomic particles (electrons, protons, etc.) which carry energy in the form of kinetic energy.[3] The three most common ion irradiations are alpha radiation, beta radiation, and neutron radiation. Alpha radiations are energetic alpha particles made of two neutrons and two protons. Their penetrability is relatively weak compared with electromagnetic waves due to their charge and size.[6-7] Beta radiation consists of fast-moving negative charged electrons whose size is around 1/7000th of an alpha particle. Therefore, the penetrability of beta radiation is much stronger than alpha radiation. Beta radiation is more ionizing than gamma rays but less ionizing than alpha radiation.[8] Different from charged alpha or beta particles, neutrons are simply neutral particles. During atomic nuclear fission or nuclear fusion reactions, high-speed neutrons are usually ejected from the atomic nucleus.[6] Compared to charged particles, neutrons have a greater penetrability and can create relatively uniform damage inside the target materials. For example, for the particles

with an energy of MeV, the travel distance of neutrons in the air is close to 10^2 cm, while for protons, it is only about 10 cm.[9-10] However, neutrons can be effectively absorbed by materials containing hydrogen atoms, such as paraffin wax and plastics, which also contribute to reducing their travel distance. Several types of ionizing radiation and their interaction with matter are shown in Figure 1.2.

1.1.2 Natural background radiation in space

Cosmic rays are high-energy atomic nuclei that travel close to the speed of light in space. Depending on the energy, origin, and flux of these particles, cosmic radiation can be classified into three main types: solar cosmic rays (SCR),[11] galactic cosmic rays (GCR),[12] and the radiation from the Earth's Van Allen belts.[13] Among these cosmic rays, Van Allen radiations have the greatest impact on human activities, particularly on the artificial satellites surrounding the Earth. Figure 1.3 shows the Van Allen radiation belts, mainly consisting of protons and electrons captured by the Earth's magnetic field. In Van Allen radiation belts, the proton energy is up to several hundred MeV, while the electron energy is usually only a few MeV. Around the Earth, there are two van Allen radiation belts. The outer van Allen radiation belt is centered at ~22,0000 km from the surface of Earth, and the inner van Allen radiation belt is centered at only ~3,000 km. Most of the telecommunication satellites are operating in low Earth orbit (LEO), which corresponds to altitude ranges varying from 180 km to 2,000 km. Therefore, these satellites are strongly exposed to radiations originating from the inner van Allen radiation belts. For Global Positioning System (GPS) satellites in geostationary orbit (GEO) located at 35,786 km, radiations from the outer van Allen radiation belt dominate.[13]

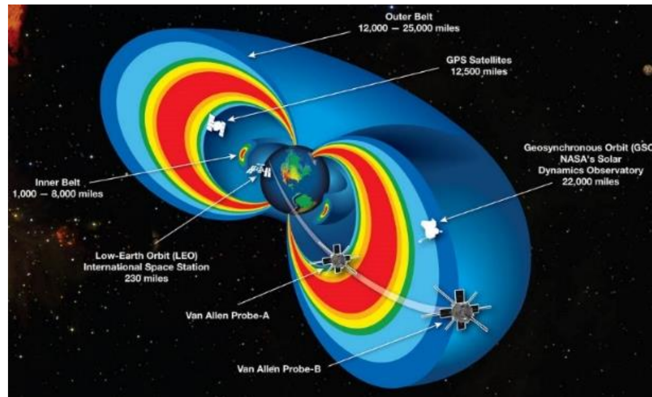

Figure 1.3 Altitude of van Allen radiation belts around the Earth.[14]

1.1.3 Artificial radiation on the Earth

Radiation has a variety of medical and industrial uses, including medical diagnosis, diseases treatments, density gauges, and nuclear gauges for the construction industry.[15-18] In medicine, X-rays are used to find broken bones and do chest tests. Radioactive isotopes are also implemented to treat cancers and other diseases.[15-16] In daily life, ^{226}Ra or ^{241}Am is applied in the smoke detector.[19] In nuclear power plants (NPPs), the heat released from the fission chain reaction of uranium is used to produce high-temperature steam, which can drive turbines to generate electricity. In these nuclear chain reactions, the energetic neutrons ejected from one split atom induce the fission of other neighboring atoms, resulting in additional neutrons. Many other types of radiation, such as X-rays, gamma-rays, also result from these nuclear chain reactions.[20]

1.2 Interaction of ionizing radiation with matter

The interaction between radiation and matter causes some unwanted changes to the microstructure and properties of the irradiated materials.[21] To develop systems suitable

for operation in a radiative environment, it is necessary to obtain both qualitative and quantitative insights regarding the irradiation-induced changes on the material. The interaction of impinging charged particles (alpha, beta, and protons) on the matter differs from that of neutral radiations (X-rays and gamma-rays). Charged particles can ionize atoms through Coulomb force, by repelling or attracting the electrons from their atoms.[22] This kind of interaction is named “direct ionization”. For uncharged particles, the radiation-matter interaction is dominated by the photoelectric effect, Compton effect, and pair production.[23] It is classified as “indirect ionization”.

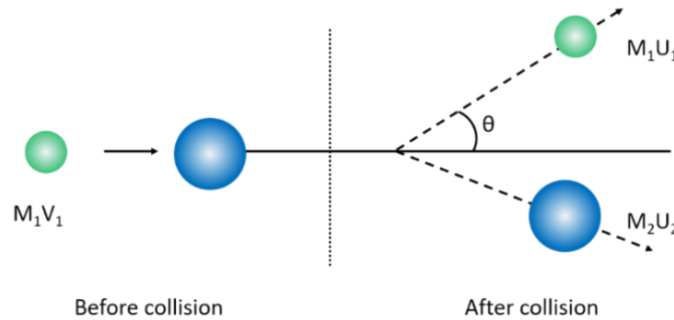

Figure 1.4 Elastic collision between two atoms.

High-energetic ions penetrating materials lose their energy via (i) elastic collisions with the target atom nuclei and (ii) interactions with the electron gas.[24] The probability of these impinging ions losing their kinetic energy through elastic collisions related to the nuclear stopping power. This process can be taken as elastic two-body scattering, as shown in Figure 1.4. After the collision, the energy transferred between two atoms can be calculated through

$$T = \frac{2M_1M_2}{(M_1+M_2)^2}E_i(1-cos\theta) \qquad \text{Eq. (1.1)}^{[24]}$$

where M_1 and M_2 are the atomic mass of two neighboring atoms, E_i is the initial energy of the incident atom, T is the energy transfer to the target atom, and θ is the scattering angle. The electronic stopping power mainly arises from the Coulomb repulsion between the impinging atoms and the electrons of the target atoms. The electronic stopping power is dominating for particles with high energy.

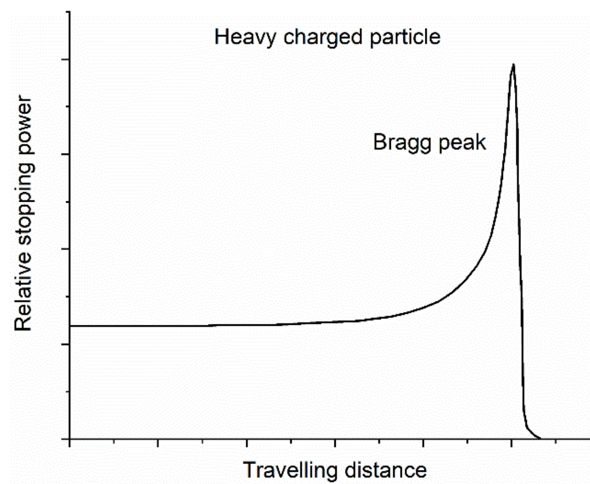

Figure 1.5 **Bragg curve for protons in relative stopping power; the sharp deposition of energy shown in the curve is known as the Bragg peak.[6]**

The Bragg curve can be obtained by plotting the energy loss of the particles as a function of their penetration depth. A typical Bragg curve of the incident proton is shown in Figure 1.5. The peak in relative stopping power observed at large penetration depths occurs right before the particle stopped and is defined as the Bragg Peak. The cross-section of interaction increases with the decrease of the particle's kinetic energy. During this process, the numerous collisions between impinging particles and atom nuclei create numerous structural damages. Such a relative stopping power given by the Bragg curve provides several practical applications in radiation therapy for cancer treatments. For

example, it becomes possible to set the energy deposition of the charged particles in a specific area, by focusing on cancer cells while minimizing the damage generated on the surrounding tissues.[25-26]

1.2.1 Heavy ions

Heavy ions are the particles whose atomic mass is much greater (at least hundreds of times) than that of an electron. Their penetration path is shorter than light ions due to their greater interaction with the medium. The energy of ions decreases with their traveling distance inside the matter, which is due to their great number of collisions with the target atoms. The interactions between the heavy charged particles and the bound electrons are inelastic, as a small part of the kinetic energy is lost[27] to overcome the binding energy of the target electrons.

1.2.2 Light ions

Light-charged particles, such as beta particles, lose energy while traveling through matter in a manner quite similar to heavy charged particles, primarily interacting with matter through the Coulomb force. However, the difference in the mass of light and heavy charged particles makes a difference in the energy losses between these two types. Light charged particles, especially electrons, will experience Bremsstrahlung radiation[28] which is electromagnetic radiation emitted by the deceleration of the charged particles. Their interactions with the electric fields of the atomic nuclei result in stronger elastic scattering effects, which lead to the greater deflection of their traveling path compared to heavy ions.[29-30]

1.3 Ion implantation

Ion implantation is a technique by which ions are accelerated to designed energy and then incorporated into a target material. During the process, the incident ions lose their kinetic energy and finally stop at a specific depth. In the early 1980s, the ion implantation technique was implemented to modify the surface of the materials and fabricate semiconductors of n-type or p-type.[31] In more recent studies, ion implantation has been found to be a reliable technique to modify the properties of thin films,[32-34] nanostructure materials,[34-37] polymers[38-39], and biocompatible materials.[38, 40-41] Such a technique can also be regarded as a relatively clean surface treatment, which brings fewer contaminations and less heating effect to the processed samples. In addition, ion implantation can maintain the geometrical parameters of the samples better than other techniques. Nevertheless, at the atomic scale, the crystal structure of the target materials can be strongly damaged or even destroyed as a result of the numerous collision cascades occurring between the impinging ions and the target atomic nuclei.

1.3.1 Depth-distribution of implanted ions

When energetic ions move in the matter, they collide with the target atomic nucleus and slow down by the surrounding electrons. The energy of the impinging ions decreases until the particles fully stop. Theoretically, the spatial in-depth distribution of the implanted ions can be described by a Gaussian distribution:

$$N(x) = N_p \exp\left[-\left(x - R_p\right)^2\right] / 2\Delta R_p \qquad \text{Eq. (1.2)}$$

where N_p is the peak concentration of the implanted ions, R_p is the projected range corresponding to the average path of impinging ions inside the materials, and ΔR_p is straggle corresponding to the standard deviation of the implanted ion distribution.

Table 1.1 Projected range and straggle of different ions implanted into Si substrate.

Ion	Energy Level keV	projected range R_p(nm)	Straggle ΔR_p (nm)
H	10	133.7	51.8
	50	468.4	81.1
	100	865.9	98.7
He	10	103.6	60.3
	50	417.9	126.1
	100	677.0	148.4
N	10	29.4	16.9
	50	129.7	51.0
	100	243.5	75.2
Si	10	17.3	8.7
	50	71.1	28.6
	100	137.0	47.4
Er	10	11.9	3.4
	50	29.4	7.2
	100	46.2	10.5

The projected range and straggle are connected to the ion energy, ion species, and the density of target materials. The projected range and straggle of different ions implanted

into Si substrate are presented in Table 1.1, showing their evolution upon the ion energy. For the same energy, ions having larger atomic mass tend to have smaller projected ranges and straggles, except for He^+ ion. The implanted dose (Q) can be calculated by integrating the distribution over the whole thickness of the implanted layer (Eq. 1.3). For most practical applications presented in this thesis, the implanted dose will vary between 10^{10} and 10^{18} ions/cm^2.

$$Q = \int_0^\infty N(x)dx \qquad \text{Eq. (1.3)}$$ [42]

1.3.2 Plasma source and beam ion implantations

In common ion implantation equipment, the typical process of implantation can be typically described as follows. A gas is first introduced into a radio-frequency plasma chamber to be used as a plasma source, from which the charged ions are extracted and accelerated to form an ion beam. The energetic ions are then orientated towards the target materials, using various electric and magnetic fields. The target surface exposed to the ion beam is relatively small with a typical beam size of around 1 cm^2. Obviously, such conventional ion implantation equipment is not suitable for material modification and/or fabrication at an industrial scale. Fortunately, the implementation of ion implantations using plasma immersion techniques (PSII) should more suitable to treat samples over larger areas. As shown in Figure 1.6 where the basic principle of this experimental method is presented, positive ions are accelerated by the electric field applied between the right and central electrodes (in dark blue) and then injected into the sample directly. A significant disadvantage of PSII is its relatively low accelerating voltage, which is around 100 kV in ideal circumstances. Compared to the classical ion

beam implantation technique, PSII is cost-effective and enables to treat sample areas of 50-100 cm^2.[43]

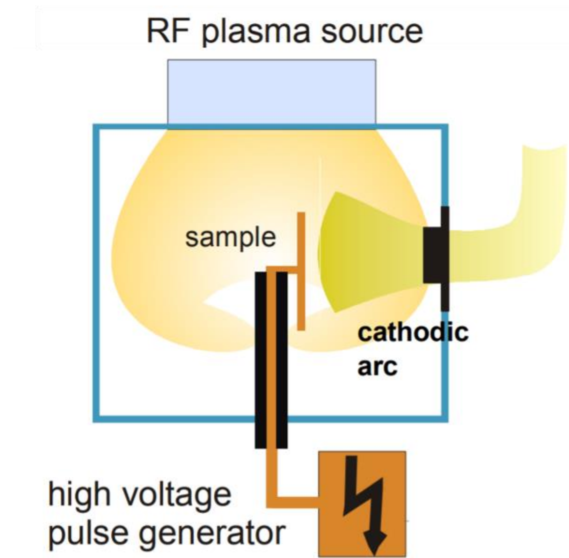

Figure 1.6 Schematic diagram of plasma source ion implantation[44]

1.3.3 Application of ion implantation

Ions with energy ranging from several keV up to hundreds of MeV can be generated by different types of ion implanters. The energy of ions can be adjusted to reproduce various experiment conditions and meet the requirement of specific applications. For example, low-energy ion implantation is widely used for surface treatment,[45] medium-energy ion implantation is commonly used for doping,[46-47] and high-energy ion implantation is employed to produce radioisotopes for medical applications.[48] The focused ion beam (FIB) is a technique used in this thesis. It can be classed as a low-energy ion implantation technique, where energetic heavy ions (such as He^+, Ar^+, and Ga^+) are accelerated for micromachining. Nowadays, FIB has been widely applied to fabricate nanodevices or prepare thin samples for TEM observation.[49]

Sometimes, it is quite difficult to prepare doped nanomaterials via conventional chemical methods. Ion implantation provides new strategies for achieving new materials with numerous degrees of freedom. Moreover, ion implantation can also be applied for welding nanowires, nanotubes, or integrating nanomaterial to nanodevices.[37, 50-51]. Li *et al.*[39] developed a surface modification method for triboelectric materials of triboelectric nanogenerators (TENG) devices based on He^+ implantations conducted at high doses. He *et al.*[33] showed that the defects introduced by ion irradiation can significantly affect the properties of the single-layer MoS_2, leading to considerable changes in its PL characteristics and electrocatalytic behavior.

In addition, ion implantation is a method for synthesizing nanoparticles (NPs), such as Si,[52-53] Ge,[54-55] Ag[56-57], Au[58-59], inside the dielectric materials (Si, SiO_2, GeO_2, and Al_2O_3). Desired ions are incorporated by ion implanter into a great variety of target substrates. The depth profile and concentration of implanted ions can be controlled from the implantation energy and dose. The nucleation of implanted ions and the growth of NPs inside the target substrate are performed using thermal annealing treatments. At the beginning of the clustering process, these NPs grow through the Oswald ripening mechanism,[53, 60-61] in which smaller particles dwindle and larger particles grow. The thermodynamically-driven spontaneous process of large particles more energetically favorable. At high implantation doses, the coalescence of small NPs into large nanoclusters may occur and lead to the formation of bigger NPs.[52-53] In general, the final size of the as-synthesized NPs is mainly depending on the annealing temperatures and durations.

1.4 Nanoparticles

In the past few decades, nanostructured materials have been the subject of intense research activities due to their unique and outstanding physical properties, which can significantly improve the performance of systems used in electronics, photoelectronic, and biology.[62-65] For the majority of materials, when their size becomes smaller than 100 nm, their optical, magnetic, and electronic properties changed significantly. Generally, nanomaterials can be divided into three categories, including zero-dimensional (NPs), one-dimensional (nanowires), and two-dimensional (thin films) nanostructured materials. Lots of efforts have been conducted for improving the optoelectronic properties of semiconductors NPs, as well as the fundamental explaining these size-dependent properties.

1.4.1 Colloidal quantum dots

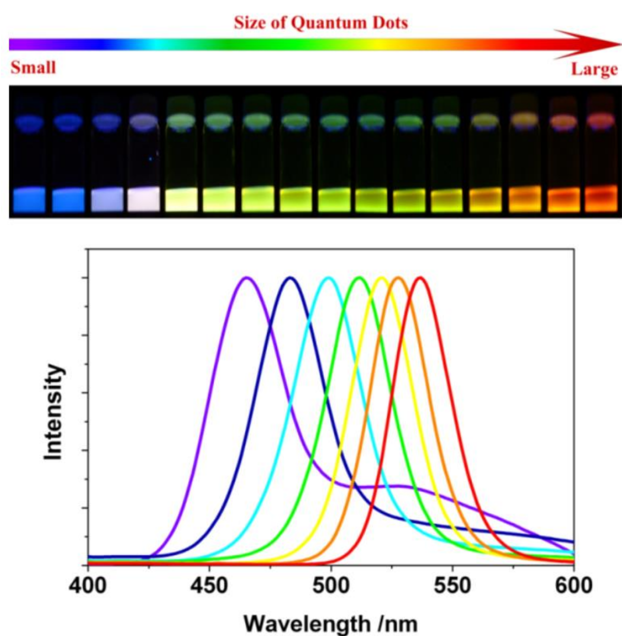

Figure 1.7 Emission colors and PL spectra of CdSe QDs. The size of QDs ranging from ~1nm to ~10 nm[66]

Colloidal quantum dots (QDs) are zero-dimensional systems, which have a sharp density of states (DOS).[67] In QDs, one extra electronic charge will repel the other charge, which makes the DOS like a staircase. Figure 1.7 shows that the wavelength of CdSe QDs is proportional to the reciprocal of the QDs diameter.[66] The properties can be tuned by changing the diameter of QDs, without modification of the chemical composition.[66]

Colloidal QDs can be used as building blocks for many applications, because of their size/shape-dependent optoelectronic properties[68] QDs-based optoelectronic devices, including photovoltaics (PV),[69-74] radiation sensors,[75-77] luminescent solar concentrators,[78-81] and light-emitting diodes (LED),[82-84] can be potentially used for future technologies because of their unique properties and low fabrication costs. The band alignment of core-shell QDs can be tuned through changing the size of core and shell, which can increase the spatial exciton separation. When the dissociation of electron-hole pairs has a large spectral range, the charge transfer will be improved.[85-87] Such manipulation of band alignment can be used to produce high photocurrent [87-88] and modify the optoelectronic properties of QDs.[87, 89-90]

1.4.2 Si nanoparticles

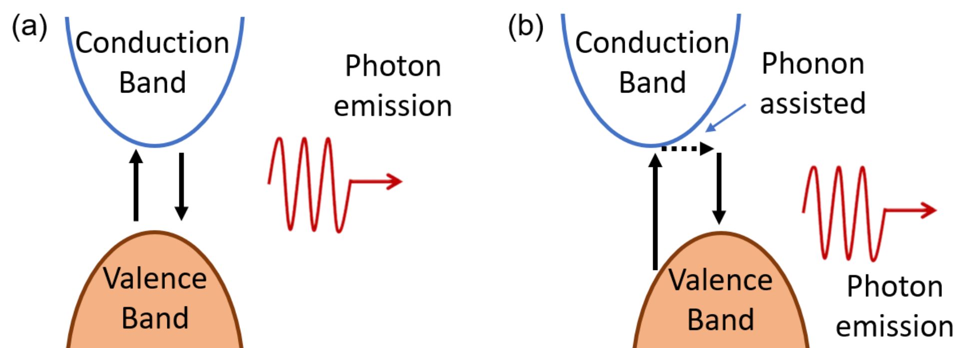

Figure 1.8 **The excitation and relaxation processes of electrons in (a) direct and (b) indirect band gap materials. The phonon-assisted process is seen in the latter case in order to conserve the momentum change.[91]**

Since the discovery of the bright red-orange fluorescence arising from electrochemically etched nanoporous silicon upon ultraviolet (UV) excitation,[92] intensive investigations have been conducted on heavy metal-free Si NPs. Compared to Cd-based materials, Si is much safer for in vitro applications, which requires the use of low toxicity or nontoxic materials.[93] The comprehensive superiorities open a new avenue for the application of Si NPs to energy sources,[94-96] sensors,[97-98] catalysis[99-100], and biomedical purposes[101-104].

Different from other semiconductor materials studied in this thesis, silicon has an indirect bandgap. The excitation and relaxation processes of the electrons bound in direct and indirect band gap materials are depicted in Figure 1.8. When an electron excites or releases in the indirect bandgap material, it will be accompanied by absorption or emission of a phonon, in order to conserve momentum. The intensity of photoluminescent (PL) can be remarkably improved, if more electrons release through band-gap transitions rather than indirect band-gap transitions. The Bohr radius of Si is around 4 nm. When the size of Si NPs is closed to the Bohr radius, strong changes are reported in its optical and electronic properties.[92] Most of these features are explained by the combination of the surface states effects and quantum confinement effects.[105-106]

1.5 Effect of ionizing irradiation on the nanoparticles

1.5.1 The morphological evolution of nanoparticles under radiation

The irradiation has been found to affect the structure of NPs, which has been investigated for several types of metal or bimetallic alloys NPs.[107-108] Previous works showed that ion bombardment can modify the shape of the irradiated NPs.[107-110] Figure 1.9 shows the

shape evolution of NPs embedded in SiO_2. In Figure 1.9, X-axis and Y-axis are the initial size and irradiation fluence, respectively. The arrow on the left of figure 1.9 (a) indicates the direction of the ion beam. It is shown that the final morphology is closely interconnected with the initial size of NP. Several different deformation regimes are also observed.

(i) NPs with diameters between 10nm and 30 nm. Nanoparticles expand along ion beam direction and their spherical shape transforms into nanorods.

(ii) NPs with diameters between 30 nm and 70 nm. After high-fluence irradiation, these NPs can be ion-shaped and tend to evolve toward facetted NPs.

(iii) NPs with diameters larger than 70 nm. No distinct deformation is observed, even after high-fluence irradiation of 5×10^{15} ions/cm^2.

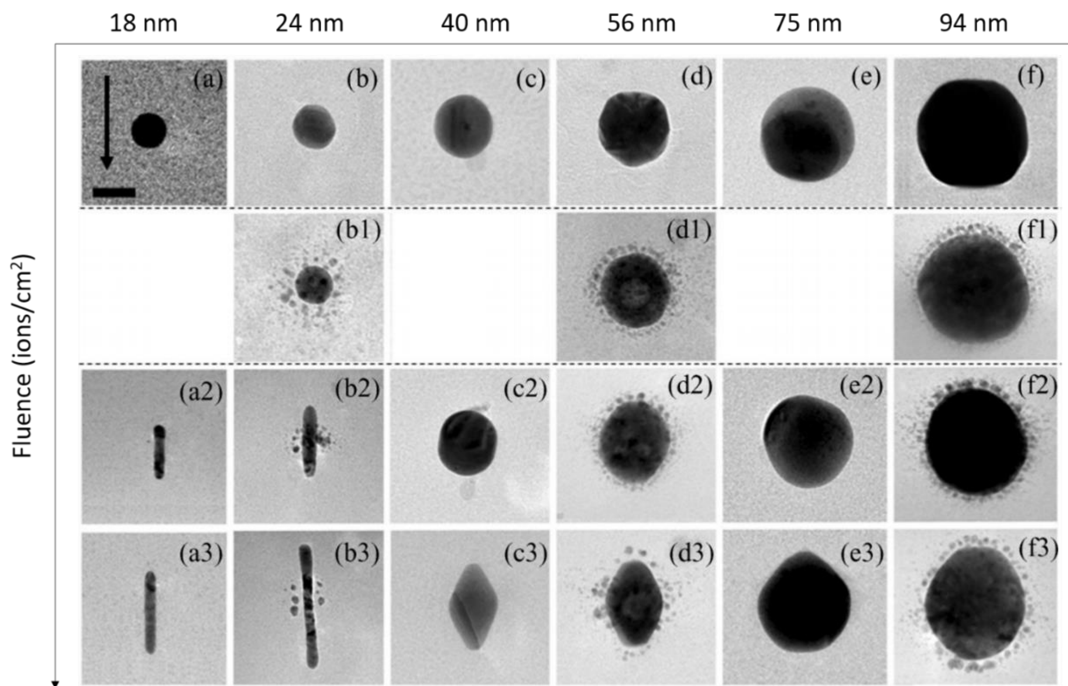

Figure 1.9 The shape evolution of Au NPs as a function of initial size and irradiation fluence. The scale bar in (a) is 20 nm. Samples (b1), (d1), and (f1) are preirradiated by Au ions at 5×10^{15}

ions/cm^2 with energy of 4 MeV. Sample (a2) to (f2) are irradiated by Kr ions at 10^{14} ions/cm^2 with energy of 74 MeV. Sample (a2) to (f2) have been irradiated by Kr ions at 5×10^{14} ions/cm^2 with energy of 74 MeV.[107]

In addition to the changes of shapes, some researchers also proved that ion irradiation could generate defects or even induce structural phase transitions.[111-113] For example, in the study of FePt NPs, it found that multiply twinned icosahedral NPs can transform to single-crystalline face-centered cubic (FCC) NPs after He ions irradiation.[113] Such structural transformation is due to the generation of Frenkel pairs, which contribute to the removal of twin boundaries. Jarvi *et al.*[111] showed that the untwining process under ion irradiation experiences transient amorphization, which is supported by experiments and simulations. Such structural transformation only occurs in bimetallic alloys NPs, because alloy NPs are more easily amorphized than bulk.

1.5.2 Effect of ionizing irradiation on optical properties

The changes of optical properties on the NPs after irradiation are quite different, which not only depends on the chemical composition but also the embedding medium. Ion irradiation (H, He, Si, Ge, and Au ions) experiments performed on Si NPs embedded in SiO_2[114] showed that the PL intensity and PL lifetime of Si NPs decreased with the increase of radiation fluence. However, proton irradiation experiments conducted on single-layered InGaAs/GaAs QDs[115-116] and multilayered InAs QDs[117-118] indicated that the PL emission was enhanced after irradiation. In the study of colloidal core-shell CdSe/ZnS QDs embedded in polymers[119], it was found that the PL intensity of QDs can increase and decrease with the proton fluence. For a fluence of 10^{13} H^+/cm^2, the PL

intensity of QDs decreased and was accompanied with the reduction of PL lifetime, which can be explained by the quenching of photocarriers. After irradiation performed at a fluence of 5×10^{13} H^{+}/cm^{2}, the PL intensity of CdSe/ZnS QDs recovers partially, which has been associated with the transfer of photocarriers between QDs and radiation-induced defects. When the irradiation fluence is up to 10^{14} H^{+}/cm^{2}, the PL intensity of CdSe/ZnS QDs is found to exceed the one measured in the original samples. The energy transfer between the QDs and surroundings was proved by probing the lifetime of donor and acceptor, which indicates that the embedding medium was important for both the PL emission and the PL lifetime of QDs under radiative environments.

1.6 Research objectives and organization

1.6.1 Research objectives

Novel NPs-based devices have significant advantages compared to traditional systems used in space missions, due to their light weight and energy-saving. However, the responses of these NPs-based devices to space radiations are not well understood. It is thus necessary to investigate the evolution of their structure and properties, before their implementation in radiation-prone environments. Some irradiation experiments were performed on Si NPs, single-layer InGaAs/GaAs QDs, and multilayer InAs QDs. After exposure to various ion beams, the PL emission intensity was found to increase or decrease depending on the radiation dose. However, there are few studies on the radiation-induced damages on the microstructure of semiconductor NPs. Irradiation effects on the morphology of NPs are usually limited to metal or bimetallic alloys NPs of diameters larger than 18 nm. There is also an important lack of research related to the effect of ion irradiation on complex nanostructures, such as core-shell structures. In this

thesis, the two main objectives are to get a fundamental understanding of radiation-induced alterations in NPs and study their effects on the material properties. The changes in microstructure shall be connected to the variations of the NP optical emission and photocurrent after irradiation. More specifically, our work aims to:

(1) Synthesize and characterize stable and radiation-resistant Er/Si NPs inside fused silica substrates as a function of different fabrication parameters, such as implanting dose, implanting energy, and annealing temperature.

(2) Conduct irradiation experiments using both e-beam and proton beam on different types of NPs.

(3) Study the effect of ion irradiations on the microstructure and physical properties of NPs, including (but not limited to):

(a) the in-depth characterization of the radiation-induced structural damaging by HRTEM analysis and Stopping and Range of Ions in Matter (SRIM) simulations, to connect the microstructural changes with the changes of several materials properties.

(b) the investigation of both the PL emission and its decay after ion irradiation.

(c) the investigation of photocarrier transfers in Er/Si systems and “giant” core-shell (g-CS) CdSe/CdS QDs.

(d) the use of ion irradiation to generate different damaging rates into g-CS structures and tune their physical properties by setting the energy of ions.

(e) the use of e-beam irradiation to study the light ions radiation effect on $CuInSe_xS_{2-x}$/CdSeS/CdS QDs

(4) Develop a new strategy to improve nanomaterials’ properties and stability.

1.6.2 Thesis organization

This thesis is divided into six parts and organized as follows:

Chapter 1 introduces the basics, background, and motivation of this project.

Chapter 2 describes experimental method details and the main characterizations.

Chapter 3 presents the effects of proton irradiation on both structural and physical properties of "giant" CdSe/CdS core/shell QDs. The publication related to this chapter is:

***C. Wang**, D. Barba, G. S. Selopal, H. Zhao, J. Liu, H. Zhang, S. Sun; F. Rosei, Enhanced photocurrent generation in proton-irradiated "giant" CdSe/CdS core/shell quantum dots, Advanced Functional Materials, 2019, 29,1904501.*

Chapter 4 presents the growth of heterostructured $CuInSe_xS_{2-x}$/CdSeS/CdS QDs and proves some types of defects can be repaired by e-beam irradiation. The publication related to this chapter is:

***C. Wang**; D. Barba; H. Zhao; X. Tong; Z. Wang, F. Rosei, Epitaxial growth and defect repair of heterostructured $CuInSe_xS_{2-x}$/CdSeS/CdS quantum dots, Nanoscale, 2019, 11, 19529-19535.*

Chapter 5 presents an alternative approach for the development of advanced Er light sources with superior radiation resistance and longer operating times in ionizing irradiation environment. The publication related to this chapter is:

***C. Wang**, D. Barba, S. Slim, Y.Q. Wang, F. Rosei, Enhanced radiation resistance of near-infrared photoluminescence emission induced by Er/Si nanoclustering, Materials & Design, 2017, 126, 57-63.*

Chapter 6 briefly summarizes the important contributions of this work and states future challenges in this field.

2 EXPERIMENT METHODS

2.1 Ion implantation process

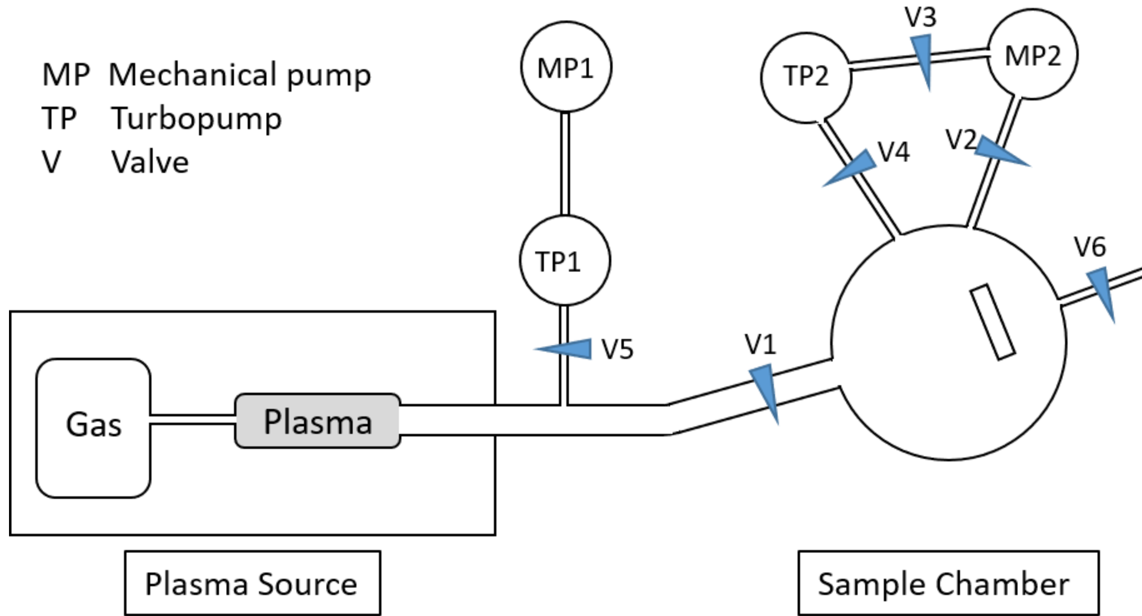

Figure 2.1 Schematic diagram of ion implantation system in our lab.

For this research, ion radiation experiments were performed inside a low-energy accelerator, equipped with a magnet mass separator and a radio frequency gas source. The acceleration voltages of ions were set between 1 kV and 20 kV. The samples were implanted over an area of 0.81 cm^2 using a collimator. Figure 2.1 presents a schematic diagram of the ion implanter, which mainly consists of a plasma source system, alignment system, and vacuum system. There are two sets of pumps in this ion implanter. One set is pumping for the plasma source, and the other one is pumping for the sample chamber. Each set of pumps has one turbopump and one mechanical pump. The ion implantations were conducted under ultra-high vacuum about 5×10^{-6} mbar.

A schematic diagram of the ion beam system is shown in Figure 2.2. Hydrogen is introduced into a radio-frequency plasma source (Figure 2.3) where positive ions are generated by stripping away electrons orbiting around the atomic nuclei. These positive ions are accelerated, focused, and filtered using several electromagnets, to be then oriented towards the target sample. The size of the generated ion beam diameters is very small. In order to incorporate the impinging ions uniformly into the target materials, two pairs of parallel metallic plates are placed before the sample and connected to a modulated tension source for XY scanning. The relation between magnet current (I_m) and the energy (E) of selected ion can be described as following:

$$I_m = k\sqrt{Em} \qquad \text{Eq. (2.1)}$$

where k is constant (k = 1.774) and m is the atomic mass of the ion. The implantation dose (D) can be calculated by Eq. (2.1)

$$D = \frac{It}{eS} \qquad \text{Eq. (2.2)}$$

where I is the measured current in A, t is the time for implantation in seconds, e is the elementary charge ($e = 1.6 \times 10^{-19} C$) and S is the area collimator ($S = 0.81\ cm^2$). The distance between the collimator and samples is about 3 cm. A -200 V polarisation is applied on the collimator for removing secondary electrons ejected from the target atoms. The charge arising from the accumulation of energetic ions on the sample is measured by a coulometer, and the generated current (I) is measured by an ammeter.

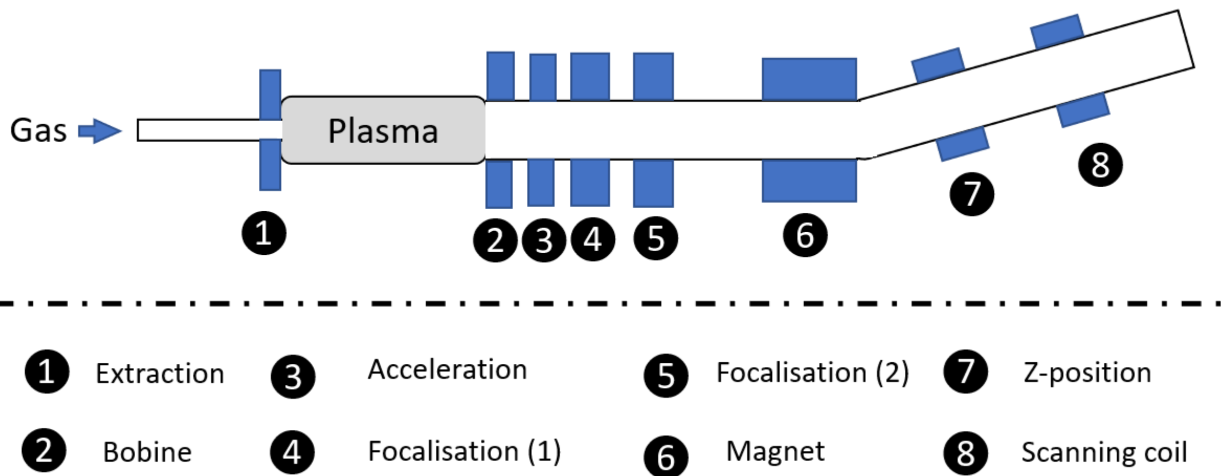

Figure 2.2 Schematic diagram of ion beam system.

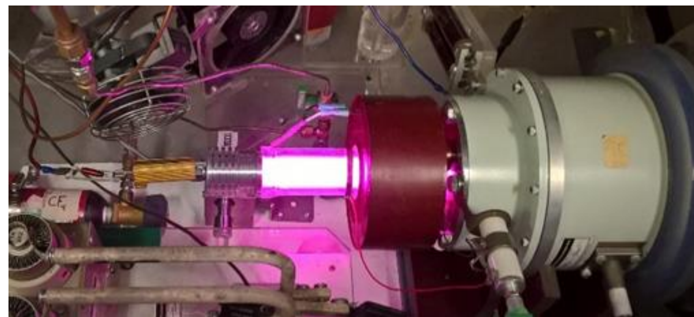

Figure 2.3 Radio-frequency plasma source.

2.2 SRIM-TRIM simulations

The SRIM software is a freeware developed in the 1980s to determine *ab initio* the ion beam implantation experiments and the ion beam processing of materials through the statistical simulations of the collisions between impinging ions and target atoms.[9] This software uses Monte Carlo algorithms. It is based on the binary collision approximation (BCA) approach, which assumes that the path of impinging ions between two successive interactions with the target atom is linear. It uses a statistical calculation to determine how the moving ions lose their energy inside the target matter. Typical applications include ion

stopping powers, straggle, projected range, the determination of damaging rates, and surface sputtering rates. SRIM investigations can also be implemented to describe ion erosion effects and design complex multi-layered systems. Transport of Ions in Matter (TRIM) is a part of the SRIM package, providing information, such as damage, recoil distribution, depth profiles of implanted ions. This SRIM-TRIM freeware has been developed by Ziegler and Biersack[9] and can be downloaded from the website: http://www.srim.org.

In this thesis, SRIM-TRIM was used to calculate the depth profiles of H^+ within different targets and collect information about the radiation-induced damage (such as vacancies or displacements per ion) inside the targets. Figure 2.4 shows the results obtained from SRIM-TRIM calculation in a silicon target exposed to proton beams of 0-100 keV, showing the electronic and nuclear stopping power as a function of the proton energy.

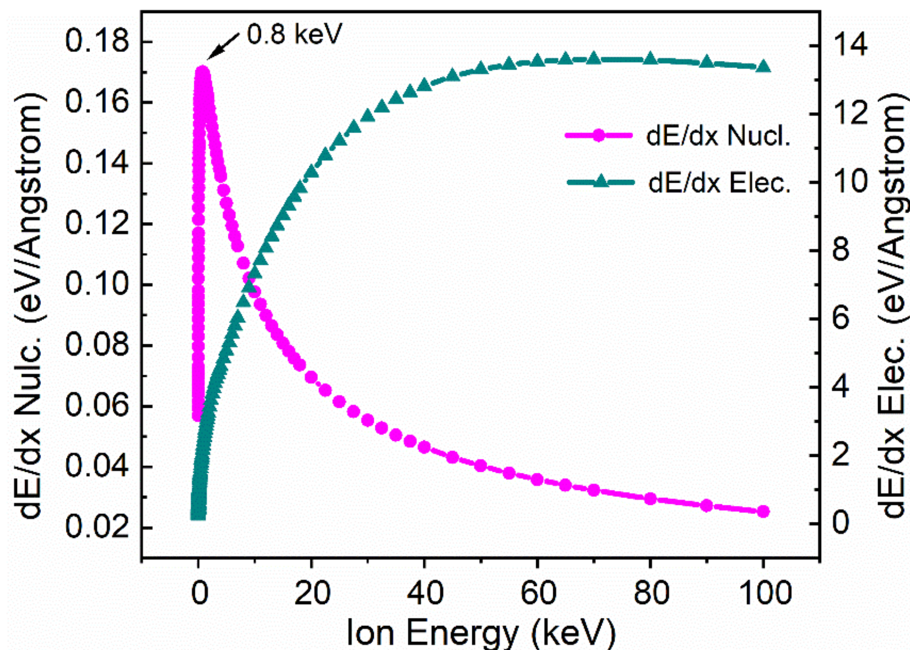

Figure 2.4 **Electronic and nuclear stopping power as a function of ion energy for proton**

TRIM-SRIM code provides the final spatial distribution of implanted ions in the target materials and the ion energy losses arising from backscattered or transmitted ions.[120] The depth profiles given by TRIM-SRIM can be compared to the calculated Norgett−Robinson−Torrens displacements per atom (NRT-dpa) [121]. In 1975, NRT-dpa standard was proposed by Norget, Torrens, and Robinson to determine the density of Frenkel pairs after collision[122]. This method has been incorporated into the ASTM E521[121] and implemented to calculate the damages generated in the materials after ion bombardments. Kinchin and Pease [123] expressed the following model (Eq. 2.3, 2.4, and 2.5) to describe ion-induced damaging:

$$N_d = 0 \rightarrow T < E_d \quad \text{Eq. (2.3)}$$

$$N_d = 1 \rightarrow E_d \leq T < 2E_d \quad \text{Eq. (2.4)}$$

$$N_d = \frac{\beta T}{2E_d} \rightarrow T < E_d \quad \text{Eq. (2.5)}$$

Where N_d is the number of displaced atoms; T is the damage energy, E_d is the minimum required energy to produce a stable Fraenkel pair and β is the factor determined from binary collision models to account for realistic scattering.

2.3 Focused ion beam

FIB can be classed as a low-energy ion implantation system, which is a powerful tool for nanodevices fabrication, nanomaterial sample preparation, atomic deposition, as well as thin TEM sample (less than 100 nm) preparation. FIB operates in a similar way with the scanning electron microscope (SEM). However, a focused ions beam, such as Ga^+ or Ar^+, is used instead of electrons.[124] The most widely used source is the liquid metal ion source (LMIS) which has the advantages of running reliability, easy fabrication, and good

manufacturability.[125] A high electric field is applied onto the gallium which is placed in the reservoir and in contact with the tungsten needle. After heating, the liquid gallium will flow to the tip of the tungsten needle. Then, gallium ions will be emitted due to the electric field ionization. Finally, the gallium ions beam is focused by several electromagnetic lenses and oriented to the target samples. Typically, the beam size is around 10 nm, which can be used for micro/nano-cutting. Due to the high intensity of secondary electrons generated by the ion beam, FIB has magnification around ×100,000, which can create images during the micro/nano-cutting. [126] Recently, most of the advanced FIB-SEM instruments have a dual-beam system. Besides the Ga^+ or Ar^+ beam, they are also equipped with another independently tunable electron gun. The extra electron gun can not only improve the quality of the image with less ion damage but also neutralizes the charge induced by positive ions.

2.3.1 Sputtering process

As shown in Figure 2.5, the energetic Ga^+ (red circles) will have strong collisions with the surface of sample after acceleration. A cascade of events, such as secondary ions (blue/green circles with "+"), secondary electrons, or other neutral atoms (orange circles), will be generated.[126] This process is known as "sputtering", which allows for the local milling of the sample. It is vitally important to manipulate the sputtering process during the operation of FIB.

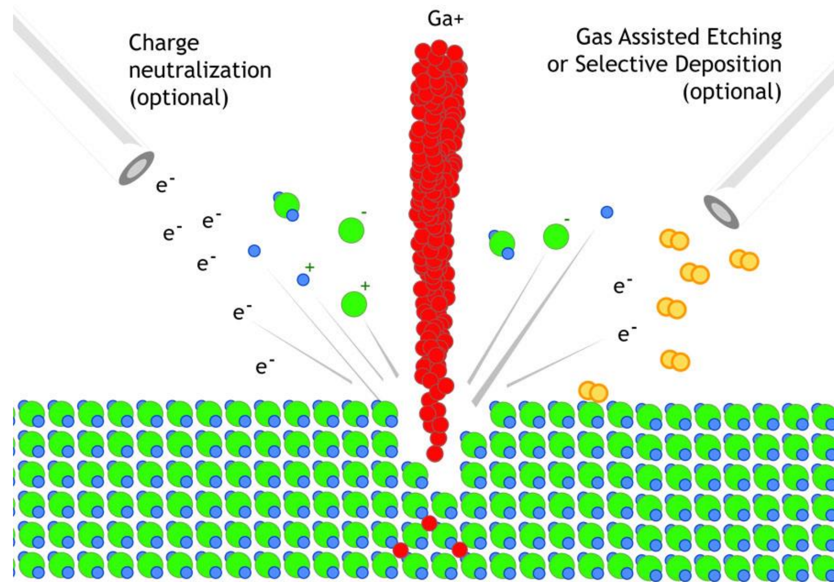

Figure 2.5 **Schematic diagram of the sputtering process in FIB. Energetic Ga^+ has collisions with the surface of the sample and sputter the material.[127]**

2.3.2 Steps to prepare TEM sample using FIB

(a) Tungsten is deposited on the desired locations of the sample to protect it in the following process steps. In addition, the deposited tungsten can stabilize the sample and prevent bending or braking effects due to internal stress or mechanical loads during sample moving, such as the in/out transfers from the FIB system or TEM. (Figure 2.6 a)

(b) Two patterns for trench milling are placed beside the tungsten. High voltage and current are applied in order to remove material quickly. (Figure 2.6 b)

(c) A so-called U-cut is used to separate the sample from the bulk material. The sample is tilted to cut the bottom and sides of the sample by the Ga^+ beam, without damaging the other parts. (Figure 2.6 c)

(d) Before the sample is completely removed by Ga^+ beam, the micromanipulator is placed on the top of the sample and fixed by deposition of tungsten. After that, the last intermediate between sample and bulk material can be milled, and then the sample can be lifted out by the micromanipulator. (Figure 2.6 d)

(e) The sample is transferred to a TEM grid and fixed by tungsten. Mill the tungsten between the micromanipulator and sample by Ga^+ beam, then remove the micromanipulator. (Figure 2.6 e)

(f) Low voltage and weak current are used for cleaning and flatting the surface of the sample. Finally, the sample is polished until thin enough for electron transparency. (Figure 2.6 f)

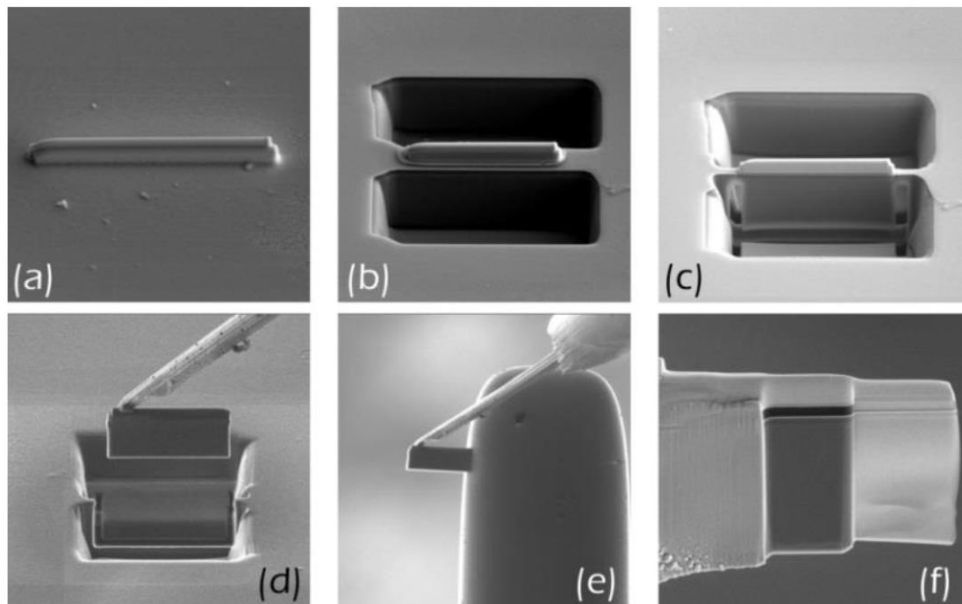

Figure 2.6 Step to prepare thin TEM samples through FIB milling. (a) deposit protecting layer of tungsten, (b) mill trench around the desired location, c) separate sample from the bulk material by U-cut, (d) in-situ lift-out sample by micromanipulator, (e) transfer the sample to TEM grid and fix it by tungsten, (f) polish the sample until thin enough for electron transparency.[128]

2.4 Characterization methods

2.4.1 Transmission electron microscopy

2.4.1.1 Resolution of TEM

TEM is a characterization technique whereby a beam of electrons transmits through an ultra-thin specimen and interacts with the atoms or molecules in the specimen.[129] The resolution of TEM is higher than visible-light microscope (VLM) due to the shorter de Broglie wavelength of electrons. Theoretically, the smallest distance which can be resolved (δ) is given by:

$$\delta = \frac{0.61\lambda}{\mu \cdot sin\beta}$$ Eq. (2.6)[129]

In Eq (2.6), λ is the wavelength of the beam, μ is the refractive index of the medium, and β is the semi-angle of collection of the magnifying lens. Take green light (λ = 550 nm) as an example. The limit of resolution is about 300 nm calculated by Eq. (2.6). According to Louis de Broglie's equation, the wavelength of electrons is related to their mass and kinetic energy. More specifically, the wavelength of one electron is inversely proportional to its momentum. Considering the relativistic effects, then the wavelength of an electron can be express as following:

$$\lambda_e = \frac{h}{\sqrt{2m_0E(1+\frac{E}{2m_0c^2})}}$$ Eq. (2.7)[129]

In Eq (2.7), λ_e is the wavelength of the electron, h is Planck's constant, m_0 is the rest mass of the electron, E is the kinetic energy of the electron, and c is the speed of light in a vacuum.

Table 2.1 Comparison list between the accelerating voltage, the wavelength of an electron, the velocity of an electron, and the ratio of the velocity of an electron to the velocity of light.[129]

Accelerating voltage (kV)	Wavelength of electron (pm)	Velocity of electron (m/s)	Ratio to the speed of light
30	6.9791	9.8445×10^{07}	0.32838
100	3.7014	1.6435×10^{08}	0.54822
200	2.5079	2.0845×10^{08}	0.69531
300	1.9687	2.3280×10^{08}	0.77653
500	1.4213	2.5868×10^{08}	0.86286
1000	0.87192	2.8213×10^{08}	0.94108

Table 2.1 provides the relationship between the acceleration voltage, the electron wavelength, the electron velocity, and the ratio of the electron's velocity to the velocity of light. Typically, for the TEM operating under 200 kV, the wavelength of the electron is around 0.0025 nm, which is much smaller than the diameter of an atom. However, it is almost impossible to build a 'perfect' TEM that can approach the wavelength-limited resolution calculated by Eq (2.4). Because there is a technical barrier for the fabrication of "perfect" electromagnetic lenses. Generally, the existence of aberrations in the electromagnetic lens, including chromatic aberration, astigmatism, and spherical aberration, will make the practical resolution much lower than the theoretical value. Recently, the design of advances electromagnetic lens improved significantly, where special aberration has been corrected, so that the sub-angstrom resolution can be achieved in aberration-corrected TEM.[130-131]

2.4.1.2 Imaging system in TEM

TEM has various imaging techniques through the manipulation of the electric current in different electromagnetic lenses. Bright-field (BF), dark field (DF), high-angle annular dark-field (HAADF), high-resolution TEM (HRTEM), and selected-area electron diffraction (SAED) are commonly used in TEM. These images are formed through different imaging principles. TEM BF and DF image is a type of amplitude contrast image, which results from variations in atomic mass and thickness of the sample. HRTEM image is a phase constant produced by the interference of e-beam. The diffraction spots in the SAED pattern correspond to the satisfied Bragg diffraction condition of the sample's crystal structure.

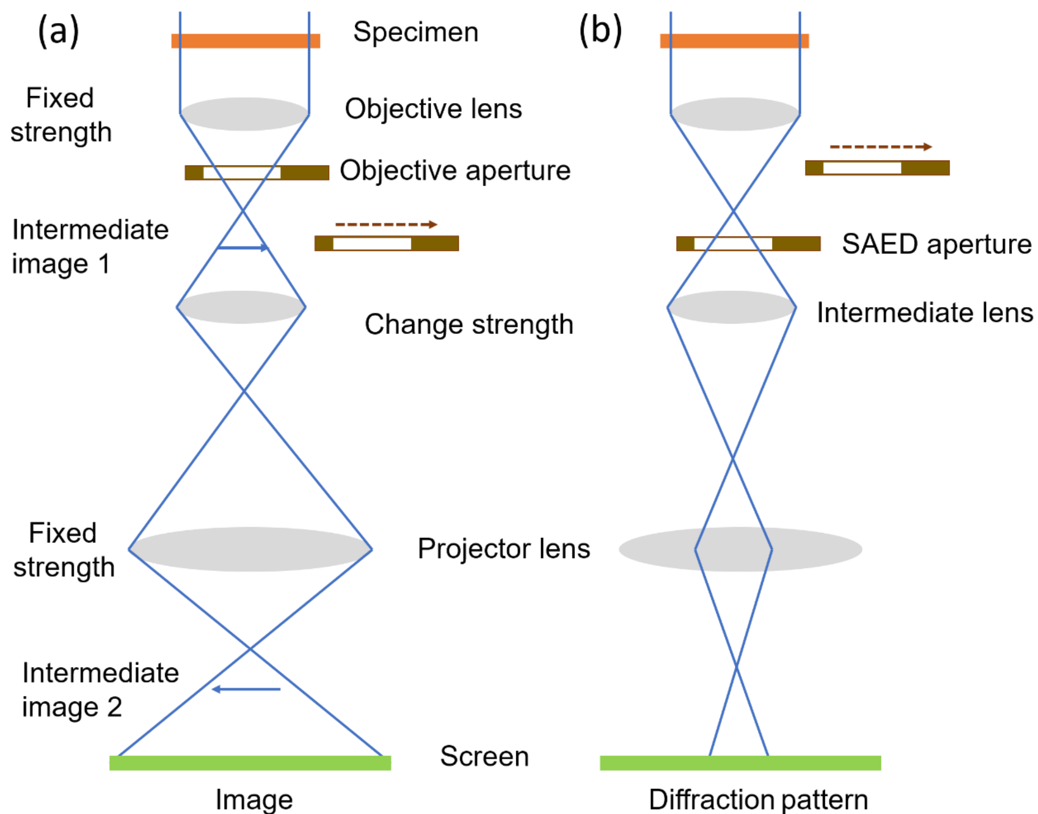

Figure 2.7 Schematic diagram shows two basic imaging modes in the TEM. (a) image mode and (b) diffraction mode.

The schematic diagram in Figure (2.7) shows the two basic imaging modes in TEM: imaging (Figure 2.7a) and diffraction (Figure 2.7b) modes. In imaging mode, the objective aperture is placed in the back focal plane (BFP) of the objective lens. The transmitted electrons or diffracted electrons are selected by the objective aperture to generate BF or DF image. A BF image will be created, if only transmitted electrons are selected by objective aperture, while the diffracted electrons are blocked. On the contrary, if only the diffracted electrons are selected while the transmitted electrons are blocked, a DF image will be received. In the BF image, regions without specimens are bright in the image, and regions with thick or dense specimens will be dark in the image. The contrast in DF is opposite to that of BF. The image formed by the objective lens in the intermediate image plane will be magnified and projected on the screen or camera through the converging of intermediate and projector lenses.

Figure 2.7(b) shows the diffraction mode, in which the objective aperture is removed, and the selected area aperture is inserted. Then the interesting area on the sample is selected to form diffraction pattern DP. The DP formed in the BFP is projected on the screen by changing the electric current in the intermediate and projected lens. Since the specimen is not uniform, the DP image will change locally. Diffraction is useful to reconstruct crystal cell and determine crystal orientation.

Another special DF image is the HAADF image, which is also named as Z-contrast image. Because the contrast in HAADF image is usually proportional to the square of the atomic number: Z^2. The differential cross-section, $\sigma_R(\theta)$, for classic scattering can describe by:

$$\sigma_R(\theta) = \frac{e^4 Z^2}{16(4\pi\varepsilon_0 E_0)^2} \frac{d\Omega}{sin^4(\frac{\theta}{2})}$$ Eq (2.8)[129]

In Eq (2.8), θ is the scattering angle, Z is the atomic number, E_0 is the initial energy of the electron, Ω is the solid angle of scattering, and ε_0 is the dielectric constant. Normally, the ADF detector cannot be used to analyze the crystalline specimens due to the Bragg scattering. However, if we decrease the camera length and avoid the Bragg electrons, an ADF image can be acquired. In this case, only electrons scattered at very high angles (> 50 mrad) are collected. It is also called HAADF image. As shown in Figure 2.8, different types of images are formed depending on the selection of the scattered electrons at different angles.

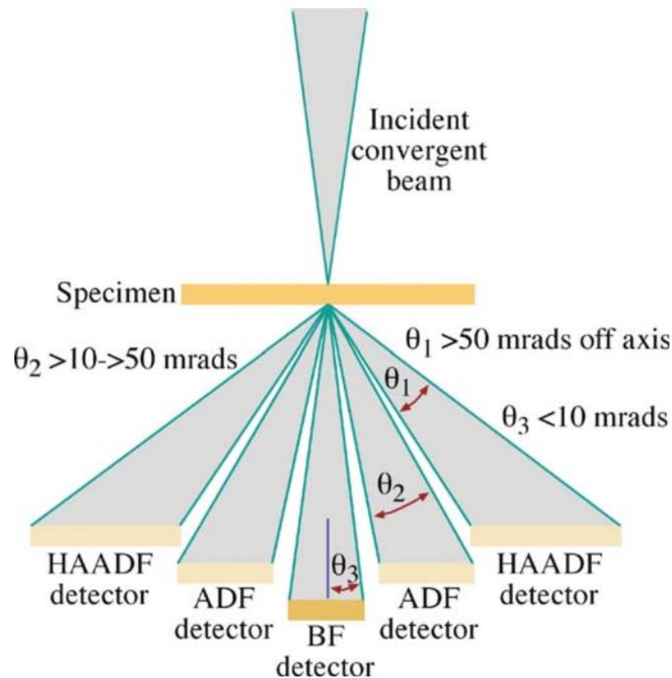

Figure 2.8 Schematic diagram shows the detector setup for HAADF ADF and BF images.[129]

HRTEM is an important imaging technique in TEM, from which we can obtain the atomic structure information from a specimen. HRTEM image is mainly caused by phase contrast, and it is produced by the interference of the transmitted beam with at least one

diffracted beam. When performing HRTEM experiments, we should select a larger objective aperture. The beam carrying with their amplitudes and phases will produce a phase-contrast image.

2.4.2 Energy-dispersive X-ray spectroscopy

Energy-dispersive X-ray spectroscopy (EDS) is a useful technique for the analysis of the elemental composition in the desired sample. As shown in Figure 2.9, inner electrons are kicked out from their nominal orbit through inelastic interactions with the electron beam. A hole will be formed and can be filled by the outer electron which has enough energy. During this relaxation process, specific energy will be released with the emission of characteristic X-rays. The energy is equivalent to the energy between two energy levels. The specific energy released during this relaxation process is applied to identify the element. The probability of X-ray emission is proportional to the atomic number (Z); therefore, EDS is more sensitive to heavy elements than light elements.[132]

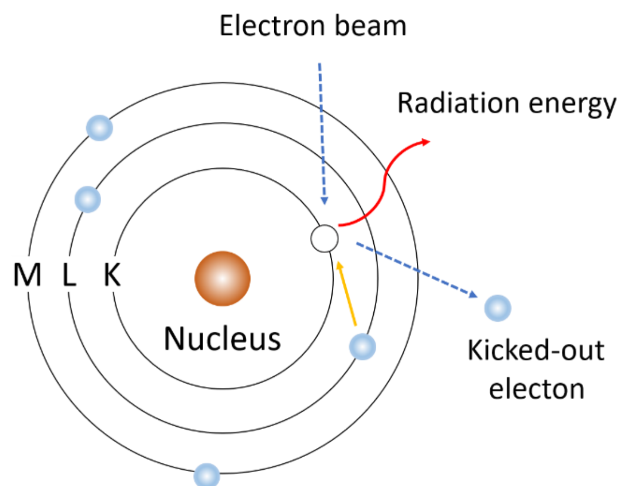

Figure 2.9 Schematic diagram of the principle of EDS.

2.4.3 Optical properties measurements

2.4.2.1 Photoluminescence spectroscopy

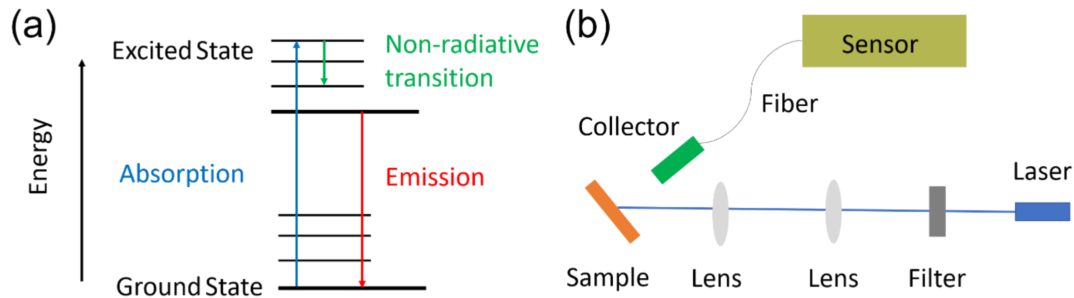

Figure 2.10 (a) Principle of the photoluminescence process; (b) Schematic diagram of setup for PL measurements.

As illustrated in Figure 2.10a, when the semiconductor absorbs a photon with energy higher than its energy band gap, the electron will be excited to the conduction band (excited state) with leaving a hole in the valence band (ground state). The excited electrons transit inside the conduction will relax through non-radiative mechanisms without photoemission. Only the excited electrons return to the ground state, which will be accompanied with photon emission. Such optical phenomenon is known as PL emission. In this thesis, PL spectroscopy measurements were conducted at room temperature using a 405 nm laser-diode excitation source. As shown in Figure 2.10b, the laser beam was focused on the sample using a series of lenses to obtain a spot with a Gaussian Intensity distribution of 1 mm diameter. The power of the laser is adjusted by the filter before lens (Figure 2.10b). The emitted light from the sample was collected by a lens in a 90° configuration and then transferred to an iDus InGaAs detector equipped with an ANDOR camera and a QE65000 Ocean optics detector, for measurements in the NIR

and visible (VIS) ranges, respectively. Before measurements, the noises that arise from the background and fused silica substrates are subtracted from the spectra. The acquisition time for each measurement is 300 ms.

2.4.2.2 Time-resolved fluorescence spectroscopy

In this thesis, the PL lifetime was measured by a time-correlated single-photon counting (TCSPC) mode with a 444 nm laser. In order to measure it in the time domain, the time-dependent PL intensity profile is recorded under the excitation of a short flash of light. Figure 2.11(a) illustrates the process of histogram formed over multiple cycles. Firstly, samples are excited by short laser pulses, then the time between excitation and emission is measured and sorted into a histogram. A typical result acquired by TCSPC is shown in Figure 2.11(b), which is a histogram with exponential decay of counts towards times. The measured decay curves are fitted by a triple exponential decay as following:

$$\tau = \frac{\sum a_i \tau_i^2}{\sum a_i \tau_i} \quad , \qquad \text{Eq. (2.9)}^{[133\text{-}134]}$$

In Eq. (2.9), τ is the life time and a_i is the coefficients of the fitting of PL triple exponential decay (i=1, 2, 3).

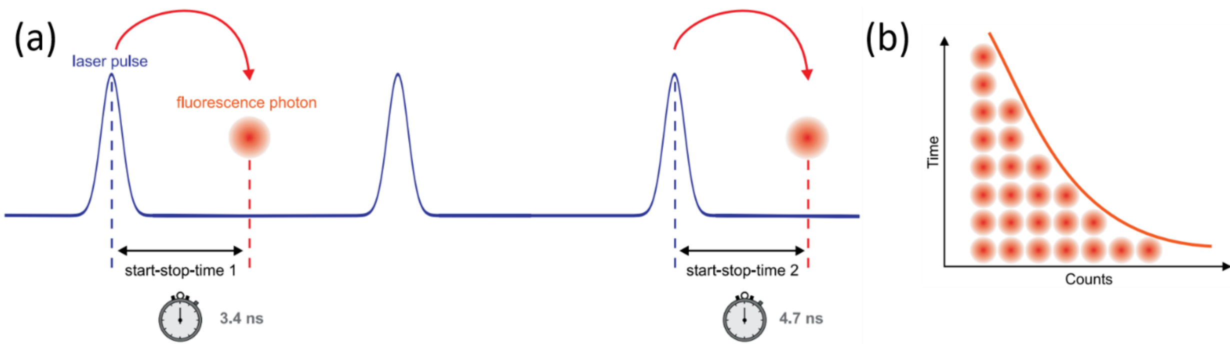

Figure 2.11 **(a) Measurement of start and stop times by TCSPC; (b). Typical histogram measured by TCSPC.[135]**

2.4.4 X-ray photoelectron spectroscopy

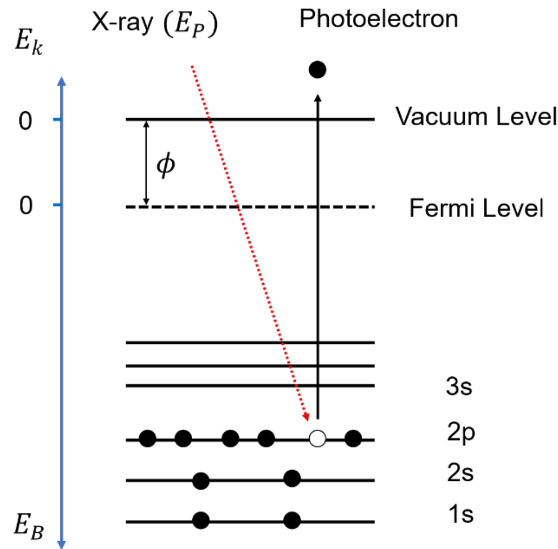

Figure 2.12 Schematic diagram of photoelectron generation.

X-ray photoelectron spectroscopy (XPS) is a powerful analysis technique, which is also known as electron spectroscopy for chemical analysis. XPS can be applied to a broad range of materials. It provides useful information regarding the elemental composition, the chemical state, the electronic structure, and the density of the electronic states resulting from the formation of specific atomic and/or molecular bonds inside the studied sample. The XPS experiments are conducted under ultra-high vacuum (10^{-7} Pa), and the typical depth of analysis is several nanometers. X-rays will interact with the surface atoms by releasing some of their electrons through photoelectric effect (Figure 2.12), according to the following relation:

$$E_B = E_P - (E_k + \phi) \ , \qquad \text{Eq. (2.10)}$$

where E_B is the binding energy, E_P is the energy of X-ray, E_k is the energy of electron measured and ϕ is the work function. The photoelectrons emitted from the sample are collected by an electron analyzer which can measure their kinetic energy (E_k), so that the binding energy (E_B) can be easily extracted from Eq. (2.10).

2.4.5 Ellipsometry

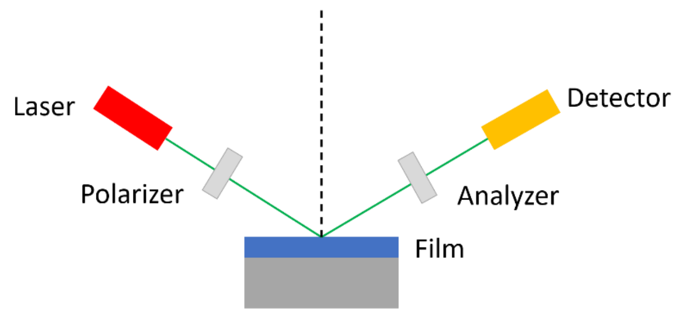

Figure 2.13 Schematic diagram of setup for ellipsometry measurements.

Ellipsometry is a non-destructive technique based on the measurement of the polarization of light (including amplitude ratio and phase difference). The change reported after optical reflection or transmission onto or through the studied materials is related to their nature and dielectric properties. Ellipsometry has been widely used to measure the thickness, roughness, the composition, and/or dopant concentration. The most well-known advantage of ellipsometry is its extreme sensitivity to very thin films. The VASE ellipsometer setup we have used for spectroscopic ellipsometry measurements is shown in Figure 2.13. Here, the incident light is emitted from a monochromatic source and reflected towards a CCD detector. Its polarization is measured after reflection using a rotating analyzer, which maximizes data accuracy near the "Brewster" condition. The

change in polarization state can be defined by the ratio of oscillating parallel to the sample surface (R_s) and the oscillating parallel to the plane of incidence (R_p), expressed in the term of ellipsometric parameters Ψ and Δ as following:

$$\rho = \frac{R_p}{R_s} = \tan(\Psi)e^{i \cdot \Delta}, \quad \text{Eq. (2.11)[136]}$$

where tan(Ψ) is the magnitude ratio upon reflection and Δ is the phase difference between R_p and R_s. As an indirect method, the Ψ and Δ ellipsometric parameters enable them to determine the dielectric function and the optical parameters of the studied medium. Such an analysis is based on a sample model where all sets of variables (related to the sample thickness, geometry, and composition) are fitted one at a time to match the experimental data. In this thesis, ellipsometry was mainly employed to measure the thickness of SiO_2 layers obtained after oxidation and thermal annealing.

2.5 Sample preparation

2.5.1 Colloidal QDs for ion irradiation and optical measurements

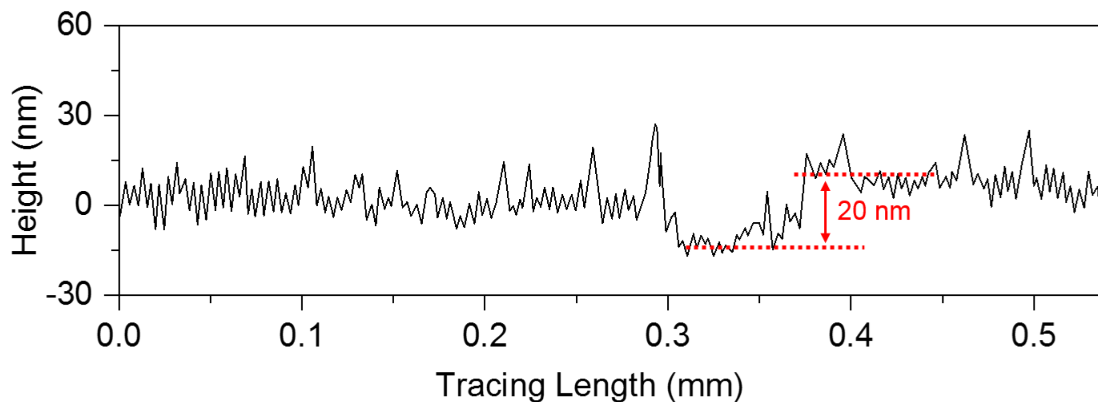

Figure 2.14 Film thickness profile measured by profilometry.

Colloidal g-CS CdSe/CdS QDs and $CuInSe_xS_{2-x}$/CdSeS/CdS QDs were synthesized using a two-step approach. The core was first prepared by hot injection[133] or thermal decomposition methods[137] followed by the growth of shell through a successive ionic layer adsorption and reaction (SILAR).[133, 137] The as-synthesized colloidal QDs were dispersed in toluene. These colloidal QDs were synthesized and provided by our collaborators. For proton irradiation experiments and optical measurements, the colloidal QDs were spin-coated on fused silica substrates for a rotating speed of 1500 r/min during 60 s. The thin QDs film formed on the top of silica substrates had a thickness of about 20 nm (Figure 2.14), which is confirmed by the profilometry measurements (Bruker, Dektak XT). The as-prepared thin QDs film has a relatively flat surface, whose surface roughness is much lower than its thickness. For TEM characterizations, freestanding QDs were dispersed on thin carbon film-coated Cu grids.

2.5.2 Samples for current-voltage measurements

I-V curves were recorded in pure Si substrates and for g-CS QDs dispersed on p-type Si wafers. Before measurements, all the samples were covered by a uniform MoO_3 layer of 20 nm thickness. As shown in Figure 2.15, 17 nm gold electrodes were then deposited by metal evaporation on the top of samples, whose bottom sides are bonded to a copper plate using silver paste. Under dark and light environment, the current through the devices was measured with the voltage between - 1.5 V and + 1.5 V. During the measurements, a tungsten tip was used to connected the upper Au electrode with the solar simulator class AAA (Sciencetech SLB-300A). The intensity of light was one sun simulated sunlight (1 sun = AM 1.5G, 100 mW/cm^2), which was calibrated by a silicon reference cell before tests. Each I-V curve was measured on 4-5 different Au electrodes which were deposited

on the same sample, in order to check the reproducibility of the measurements. Generally, we used the value measured from the middle Au electrodes, because sometimes there was a short circuit for the Au electrodes closed to the edge of samples.

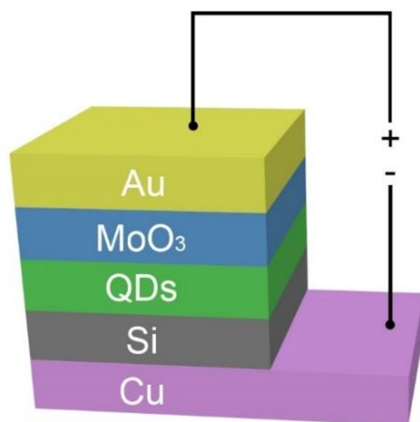

Figure 2.15 Schematic diagram of the device for I-V measurements.

2.5.3 Synthesis of Er/Si NPs embedded SiO_2 layer

SiO_2 layer with a thickness of ~200 nm was grown on Silicon wafers through thermal oxidation. A typical SiO_2 layer formed under 1100 ^oC with an oxygen flux of 4.3 is shown in the HAADF image of Figure 2.16. $^{28}Si^+$ ions were initially implanted in the SiO_2 layers at energy of 50 keV with fluence of 2.0×10^{17} ions/cm^2, then Er^{3+} ions were implanted at 150 keV with fluence of 5.0×10^{15} ions/cm^2. The ion implantation was performed by IMC commercial implanter. After implantation, samples were annealed inside a quartz tube furnace (Lindberg-Blue) with ultra-high purity N_2 flux at atmospheric pressure. The annealing time was 1 hour for all samples, and the annealing temperature was set up

between 1000 °C and 1200 °C. For TEM characterizations, cross-sectional TEM specimens were prepared by conventional ion thinning and FIB.

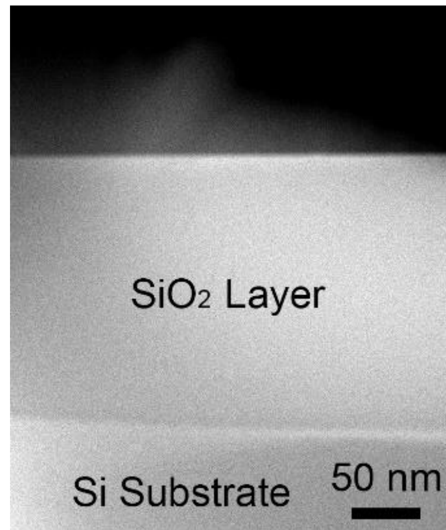

Figure 2.16 Cross-sectional HAADF image of silicon substrate with ~ 200 nm SiO_2 layer after thermal oxidation.

2.6 Data analysis

The original TEM dm3 files were analyzed and converted by DigitalMicrograph from Gatan company, which included indexing of SAED patterns, analysis of HRTEM images, and fast Fourier transform (FFT).

All measured curves and calculation results from SRIM were plotted and analyzed in Origin 2016. The intensity of the PL signal was acquired by integration of the peak areas after subtracting the optical background. Implantation depth profiles and vacancies distribution calculated by SRIM simulation was given after Gaussian fitting. Because ion erosion and swelling effects due to the introduction of ions into the target materials are low for the implantation doses chosen in our experiments.

The size-distribution analysis of the as-synthesized NPs was then completed by Nano Measurer 1.2. Typically, the number of NPs counted for statistical analysis was around 200.

3 EFFECT OF PROTON IRRADIATION ON CORE/SHELL QUANTUM DOTS

3.1 Motivation

Colloidal core-shell QDs are promising building blocks for next-generation optoelectronic devices, such as PV, LED, and radiation sensors. Novel core-shell QDs-based devices have significant advantages over traditional technologies for future space missions due to their light weight and energy-saving. In addition, core-shell QDs have unique electronic structure, in which the electron-hole spatial overlap can be manipulated by changing the chemical compounds or adjusting the size of both the core and the shell. The reduction in electron-hole spatial overlap can enhance the recombination time and promote the transfer of conduction electrons at the interface between QDs and their neighboring semiconductors. However, there is a lack of research aiming at determining the effects of ion irradiation on both the optical and electronic properties of core-shell QDs, where the presence of structural defects resulting from collisions between impinging ions and target atoms should have a strong impact.

In this chapter, we performed proton irradiation experiments on g-CS CdSe/CdS QDs system for the first time. These materials were chosen because of their high stability over time. We used the SRIM-TRIM Monte Carlo simulation code to evaluate the damage resulting from the ion-matter interaction for 1.5 and 10 keV energies and ion fluences up to 10^{17} H^{+} cm^{-2}, which corresponds to radiation exposure conditions for long-term operation on Earth and durations longer than several decades in outer space. The results indicate that ion implantation can be implemented to generate different damaging rates into core-shell structures by setting the acceleration energy of impinging ions. Most of the

results presented in this chapter have been previously published in Advanced. Functional Materials, 29 (46), 1904501, 2019.

3.2 SRIM simulations for irradiation damage on g-CS QDs

3.2.1 Simulations for g-CS QDs under H^+ irradiation

Ion beam implantation conditions and their processing parameters were guided by *ab initio* SRIM Monte Carlo calculations detailed in section 2.2. For the convenience of these simulations, we built a simple three-layer model. As shown in Figure 3.1, the thickness of each layer is set to 3 nm, which is defined by the shell thickness and the core diameter of the as-prepared g-CS QDs. Firstly, the proton bean will interact with the CdS layer, then the CdSe layer, and finally the CdS layer again. The rate of damage generated by impinging protons depends on their energy, tilt angle, as well as density and atomic composition of the target.

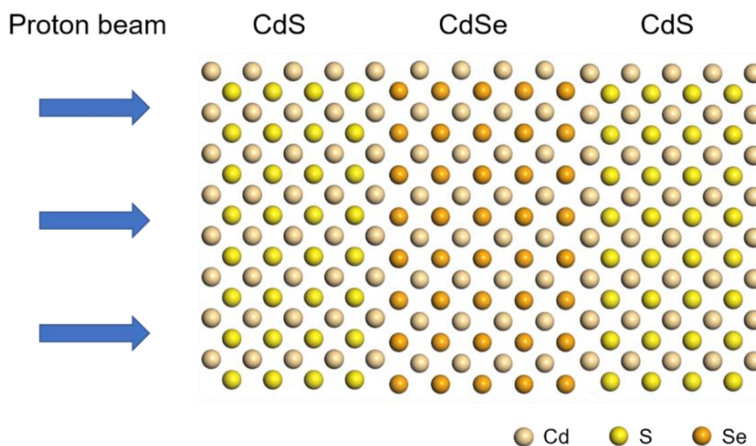

Figure 3.1 Three-layer model for SRIM-TRIM simulations, the thickness of each layer is 3 nm

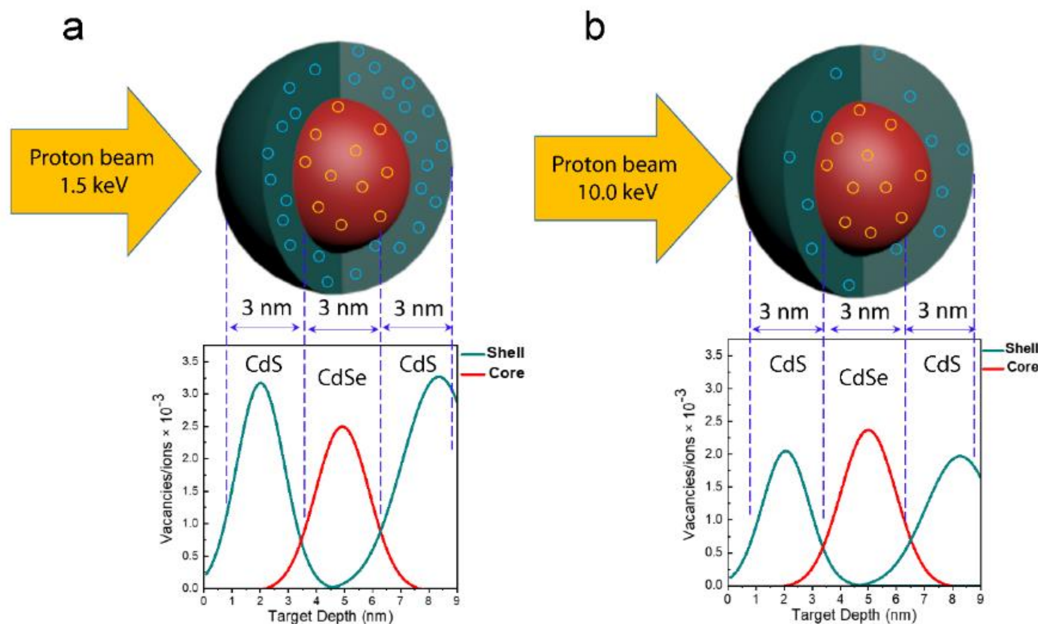

Figure 3.2 **Vacancy distribution calculated from SRIM-TRIM simulations, inside g-CS QDs exposed to 1.5 keV (a) and 10 keV (b) proton beams.**

Two different acceleration voltages of 1.5 and 10 keV were set, to promote the formation of vacancies either in the shell or in the core, respectively. For such energies, more than 89 % of the impinging protons entirely cross the g-CS QDs, according to SRIM simulations. SRIM 2013 full-cascade simulations performed with CdSe density of 5.82 g/cm^3 and CdS density of 4.82 g/cm^3 are presented in Figure 3.2. The maximum penetration depth of impinging protons is calculated using these simulations in the target. They are ~80 nm and ~260 nm, for acceleration voltages of 1.5 kV and 10 kV, respectively. Figures 3.2a and 3.2b show the depth-distribution of the vacancies created by 1.5 and 10 keV proton beams, respectively. Nuclear collisions are usually higher for low proton energies (Figure 2.3), so that implantation conducted for an acceleration voltage of 1.5 kV generates more vacancies. The latter is related to recoiled target atoms

that were displaced from their original site after elastic collision with impinging protons. The plot ordinate units are given in vacancy per ion, so that the total vacancy concentration can be directly obtained from the ion-beam current and the irradiation times that are measured during each experiment.

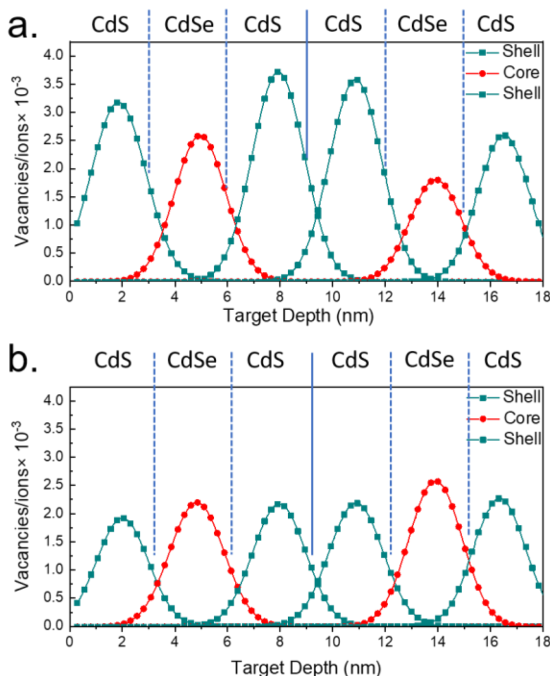

Figure 3.3 Vacancy depth-distribution calculated from SRIM-TRIM simulations, inside two stacked g-CS QDs exposed to 1.5 keV (a) and 10 keV (b) proton beams.

The results presented in Figures 3.2a and 3.2b indicate that 1.5 and 10 keV proton irradiations create almost the same rate of vacancies inside the CdSe core, while 1.5 keV proton irradiation creates 30% higher vacancies in the CdS shell than that of 10 keV protons. Such features remain qualitatively valid for two stacked g-CS QDs exposed to 1.5 keV and 10 keV proton beams, as shown by the SRIM damage profiles presented in Figure 3.3, where the solid lines in green refer to the relative fraction of vacancies

generated in the CdS shell, and the solid lines in red refer to the ones generated in the CdSe core. The density of vacancies created by proton irradiations in the second layer of g-CS QDs is close to that calculated in the first QDs layer. As shown by the red and green curves in Figure 3.3, the proportion of vacancies between core and shell remains almost unchanged. For 1.5 keV proton irradiations, the vacancies density is higher in the shell, while 10 keV proton irradiation is the opposite. Such results indicate that the ion implantation energies can be set to control the formation of structural defects in the different regions of the target samples, even for multilayered g-CS QDs.

3.2.2 Simulations for g-CS QDs under He^+ irradiation

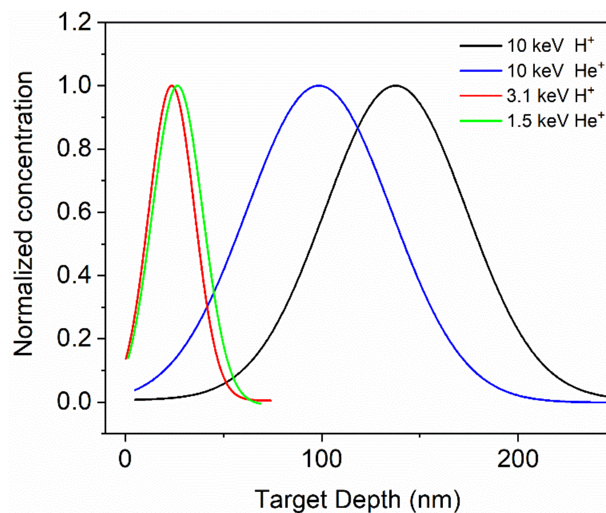

Figure 3.4 Implantation depth-profiles of H^+ and He^+ with different energy are calculated by SRIM-TRIM simulations. The target material is CdS with a density of 4.82 g/cm^3.

Besides the calculation for proton irradiation, we also carry out calculations on g-CS QDs under He^+ irradiation with different energy. The penetrability of He^+ is weaker than H^+, due to its large atomic mass. Therefore, the two energy levels we chose for SRIM-TRIM simulations are 3.1 keV and 10 keV, instead of 1.5 keV and 10 keV for experiments

conducted with protons. The implantation depth-profiles of H^+ and He^+ are compared in Figure 3.4, where the concentrations of ion-induced vacancies are normalized. In this figure, it can be seen that the depth-profile of He^+ implanted at an acceleration voltage of 3.1 kV is quite similar to that of H^+, accelerated at 1.5 kV. This means that for both implanted species, most of the impinging ions pass through the whole QDs layer.

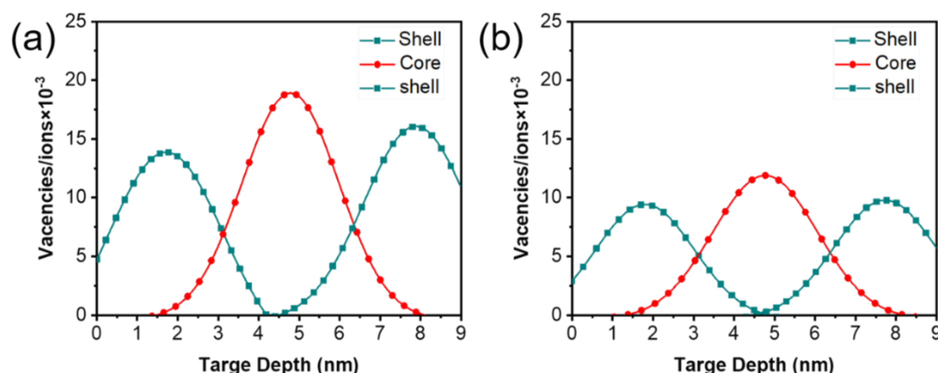

Figure 3.5 **Vacancy distribution of g-CS QDs exposed to 3.1 keV (a) and 10 keV (b) He^+ irradiation, which is calculated by SRIM simulations.**

The vacancy distribution in g-CS QDs under He^+ irradiation is shown in Figure 3.5. The solid lines in green and red refer to the relative fraction of vacancies generated in the CdS shell and the CdSe core, respectively. Obviously, higher energetic He^+ generates fewer vacancies inside the QDs, which results from the decrease of nuclear stopping power. In addition, helium ions generate more vacancies in the core than the shell for both acceleration voltages. To create more vacancies in the shell than the core, it would be necessary to further reduce the energy of impinging He^+. However, reducing the acceleration voltage of He^+ below 3.1 kV would not permit the impinging ions to completely cross the double layer of QDs, due to their weaker penetrability compared to H^+. As shown in Figure 3.4, the projected range of 3.1 keV He^+ is about ~ 25 nm, which

is already close to that of 1.5 keV H^+ (~ 23 nm). These features mean that for this kind of material, the use of He^+ beams to make the concentration of ion-induced structural defects higher in the CdS shell than in the CdSe core while maintaining the presence of He dopants negligible in the implanted g-CS is not possible.

3.3 Structural damages arise from proton irradiation

3.3.1 TEM analysis of QDs after proton irradiation

BF (Figure 3.6a) and HRTEM (Figure 3.6b) images show g-CS QDs with narrow size-distribution and clear crystalline lattice. The inset SAED pattern in Figure 3.6(a) demonstrates that the g-CS QDs have Wurtzite (WZ) crystal structure (JCPDS No. 00-041-1049). Three diffraction rings are found close to the transmission spots in SAED pattern. They are indexed as $\{10\bar{1}0\}$ $\{0002\}$ and $\{10\bar{1}1\}$. The strong diffraction rings also indicate the good crystallinity of QDs before and after proton irradiation. Before proton beam exposure, the individual QDs exhibit uniform TEM contrast, except for a few QDs that contain some structural defects, such as stacking faults (SF).[138] The crystal plane d-spacing shown in Figure 3.6b is measured to be ~3.16 Å and ~3.58 Å, with an angle between crystal faces of ~63.9°, which corresponds to the $(10\bar{1}1)$ and $(10\bar{1}0)$ plane of WZ crystal structure of CdS.[133] After proton irradiation of 1×10^{17} H^+/cm^2, the TEM contrast of individual QDs (Figured 3.6c and 3.6e) is not as uniform as the one reported before irradiation (Figures 3.6a and 3.6b). Both BF and HRTEM images reveal the appearance of small white spots, which are pointed out by arrows in Figures 3.6c and 3.6e. This feature is corroborated by the modulation of the HRTEM contrast intensities

along with the directions drawn on each image (Figure 3.6 b-f), indicating significant changes after irradiation.

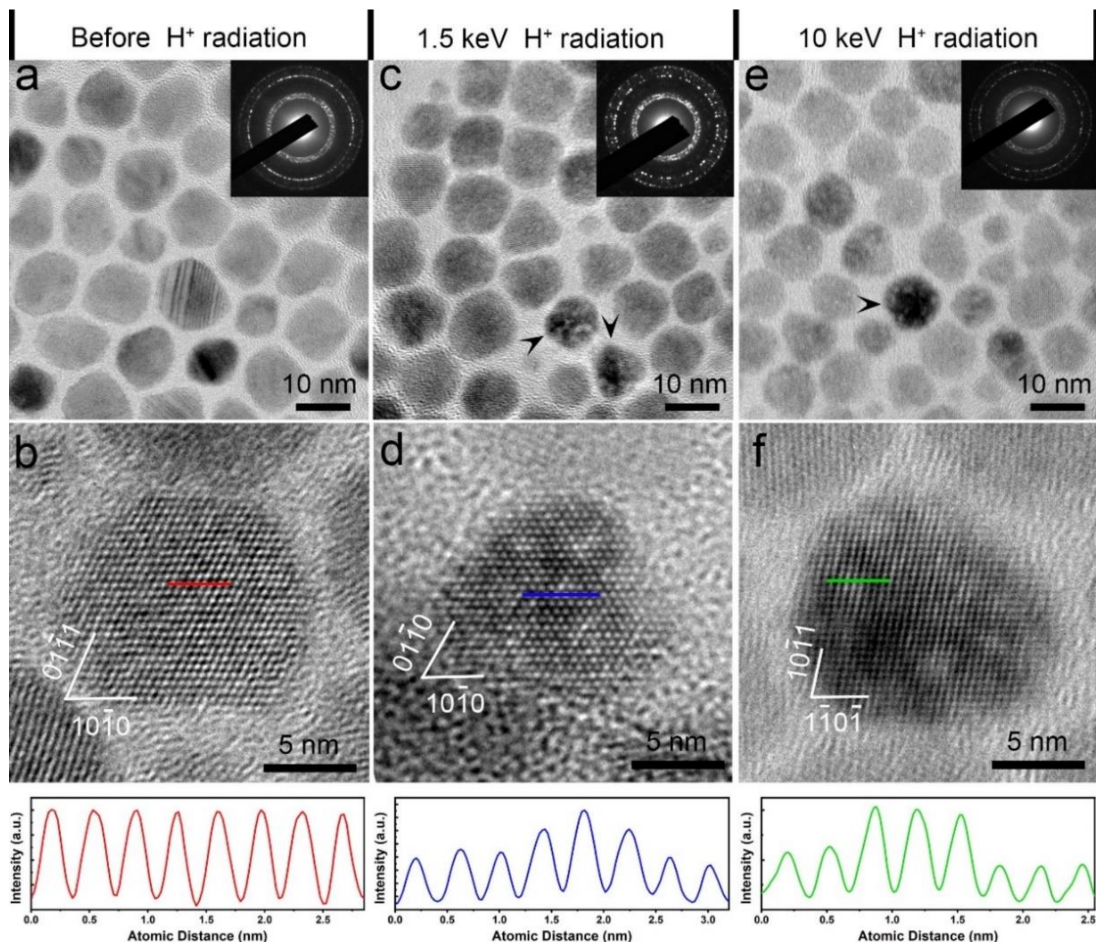

Figure 3.6 **BF images, HRTEM images and intensity profiles of g-CS QDs: (a) and (b) before irradiation; (c) and (d) after 1.5 keV proton irradiation at 1×10^{17} H^{+}/cm^{2}; (e) and (f) after 10 keV proton irradiation at 1×10^{17} H^{+}/cm^{2}.**

Nevertheless, Figures 3.6d and 3.6f show that the crystalline lattice is still ordered, showing $\{10\bar{1}0\}$ and $\{10\bar{1}1\}$ lattice planes that were used to determine both d-spacings and interplanar angles. After proton irradiation, no volume expansion is observed, since the crystal plane d-spacings are still consistent with the ones of bulk WZ CdS (JCPDS No. 00-041-1049). This confirms that the impinging protons go through the whole QDs.

According to the depth-profiles of protons calculated by SRIM-TRIM for the chosen acceleration voltage,[9] the projected range of 1.5 keV protons in CdS is about 23 nm (Figure 3.4). The integration of the proton spatial distribution curve between 0 and 9 nm accounts for about 8.6% of the total area, which means less than 10% of impinging protons are stopped inside the irradiated g-CS QDs. Such a value is consistent with the fact that no lattice expansion has been found in the measurement of d-spacings of irradiated QDs. The inset SAED patterns in Figures 3.6c and 3.6e also indicate the crystal structure of QDs survived to ion doses as high as 1×10^{17} H^+/cm^2. For defect-free QDs, the non-uniform TEM contrast mainly arises from mass-thickness contrast.[129] Therefore, the white spots formed in the QDs can be associated with nanoscale cavities.

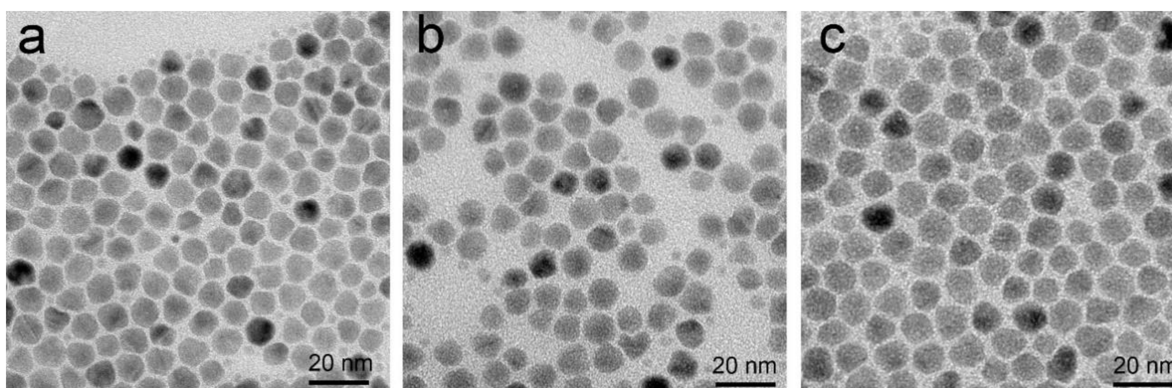

Figure 3.7 **TEM images of g-CS QDs after 10 keV H^+ irradiation showing the evolution of the QDs structure for fluences of 1×10^{16} H^+/cm^2 (a), 5×10^{16} H^+/cm^2 (b) and 1×10^{17} H+/cm^2 (c), respectively.**

To evidence the formation of nanocavities, proton irradiations were conducted for ion doses varying between 1×10^{14} H^+/cm^2 and 1×10^{17} H^+/cm^2, followed by TEM observations. The low magnification (×120,000) TEM images are presented in Figure 3.7 and those recorded at higher magnification (×400,000) are presented in Figure 3.8, for proton

irradiations conducted at fluences between 1×10^{16} H^{+}/cm^{2} and 1×10^{17} H^{+}/cm^{2}. These micrographs show that the sharpness of the nanocavities is non-uniform in the irradiated QDs. The contrast of TEM image finally obtained depends on the experimental parameters (beam intensity, magnification, and size of objective aperture), sample thickness and the crystal orientation of each QD. Therefore, even all irradiated QDs (Figure 3.8b and 3.8c) are damaged by the proton beam, nanocavities are only found in the QDs which are viewed along the zone axis. These QDs look dark compared to others, due to strong diffraction effects. Whereas, most of the nanocavities found in other QDs are blurred due to their higher brightness. The micrographs presented in Figures. 3.8a, 3.8b, and 3.8c show that the nanocavities start to form with implanted ion doses higher than 5×10^{16} H^{+}/cm^{2}, for 10 keV protons. In addition, the size of the formed nanocavities is found to increase with the proton fluence. For ion doses lower than 5×10^{16} H^{+}/cm^{2}, no significant change was observed in TEM images. This value defines a minimum threshold below which the ion-induced defects are not detectable using TEM.

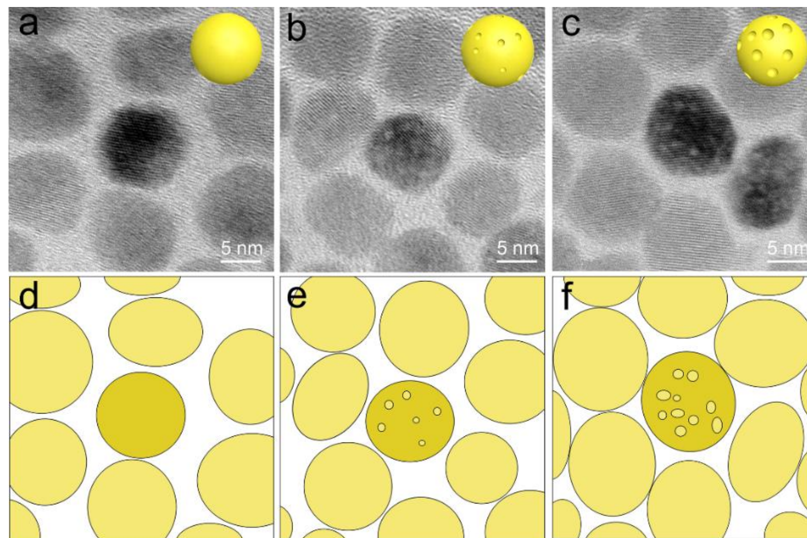

Figure 3.8 **TEM images and sketches of g-CS QDs after 10 keV proton irradiation with fluence of 1×10^{16} H^{+}/cm^{2} (a, d), 5×10^{16} H^{+}/cm^{2} (b, e) and 1×10^{17} H^{+}/cm^{2} (c, f), respectively.**

3.3.2 Formation of nanocavities inside QDs

The formation of nanocavities can be explained as follows: during irradiation experiments, the impinging protons have successive collisions with the target atoms of QDs. After the collision, if the energy transferred to the target atom is larger than the binding energy of a lattice atom to its site, a vacancy can form. In a particular area of QDs, a cavity can be found only if the number of atoms knocked out by impinging protons is large enough. Objects smaller than 1 nm are not accounted in this study because there are too close to the detection limit of the TEM (around 0.6 nm). We can nevertheless assume that nanocavities with diameters smaller than one nanometer can form during irradiation. The density of vacancies created by proton irradiations can be calculated from the product of proton fluence and the vacancies generated per ion (Figure 3.2b). For 10 keV proton irradiation at an ion dose of 1×10^{17} H^+/cm^2, the density of vacancies is about 2 per nm^2. For an average QD area of 65 nm^2, this corresponds to about 130 vacancies per QD. Considering that one nanocavity consists of 10-20 vacancies, the average number of nanocavities should be between 6 and 13. This rough estimation is consistent with the number of nanocavities observed by TEM (Figure 3.8c), where the surface concentration of nanocavities is found to be around 10 per QD. Such a feature remains also valid for proton irradiations conducted at lower fluences (Figure 3.2b).

3.4 Effects of proton irradiation on optical properties of g-CS QDs

3.4.1 Evolution of PL emission after irradiation

All samples were measured at room temperature with the same active area (~2 mm^2), to compare the optical properties of QDs before and after irradiation. Figures 3.9a and 3.9b

show the absorption and PL spectra of g-CS QDs before and after irradiation with 1.5 and 10 keV protons, for ion doses varying between 5×10^{13} H^+/cm^2 and 5×10^{15} H^+/cm^2. Before proton irradiation, the average quantum yield (QY) of as-synthesized g-CS QDs is found to be ~45%, as reported in the literature.[133] In Figures 3.9a and 3.9b, while the PL intensity of the irradiated QDs is found to decrease with the irradiation dose, neither shift nor spectral changes are measured.

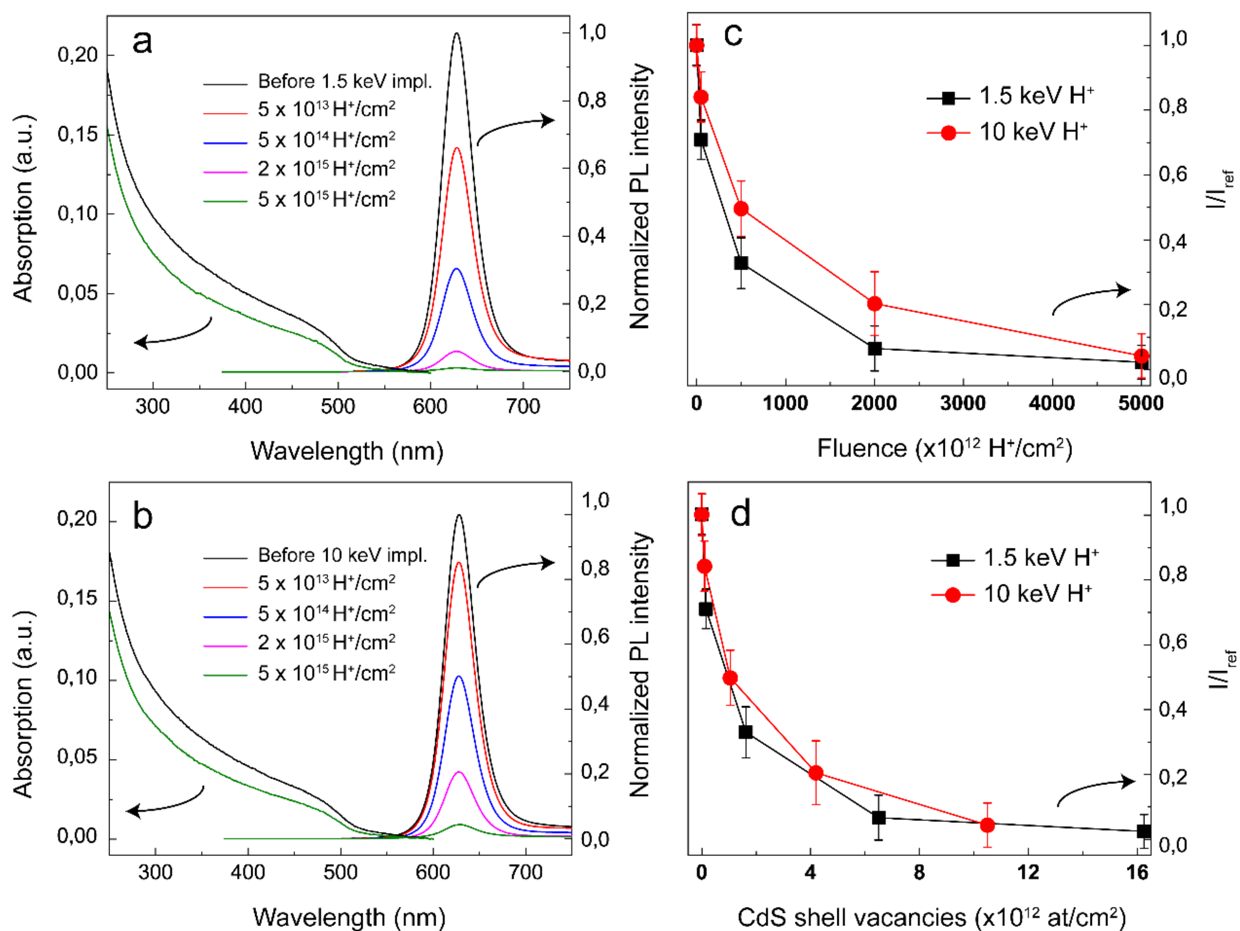

Figure 3.9 **Evolution of the absorption and PL spectral emission in g-CS QDs exposed to1.5 keV (a) and 10 keV (b) proton irradiation, with the dose-dependence of the PL signal integrated between 550 and 700 nm (c), and as plotted as a function of the variation in CdS shell vacancy surface concentration calculated by SRIM (d).**

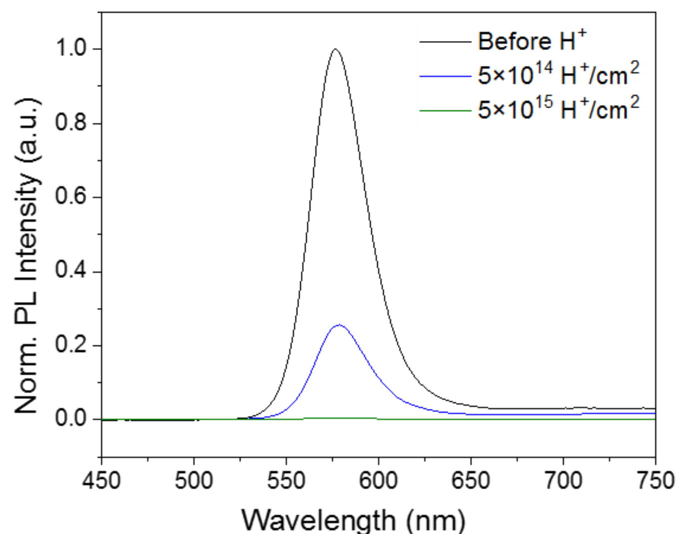

Figure 3.10 Evolution of PL spectral emission for CdSe QDs exposed to 20 keV proton beam.

Similar variation in PL emission was also recorded in preliminary studies conducted on core CdSe QDs exposed to 20 keV protons, as presented in Figure 3.10. The behavior reported in this work for g-CS QDs exposed to 1.5 kV and 10 kV proton beams differ from the results obtained by Zanazzi *et al.* for CdSe/ZnS QDs embedded in polyvinyl alcohol (PVOH),[119] who observed a decrease followed by an increase of the QD PL emission after 2 MeV proton irradiations, due to the activation of charge carrier transfers between the QDs and the irradiated matrix of PVOH. As the materials we have investigated by PL measurements are free-standing g-CS QDs dispersed on a silicon wafer, no contribution from their surrounding is expected before and after irradiation, so that their PL emission decreases continuously with the proton irradiation dose.

Our observation also highlights that both the size and band gap of g-CS QDs remain unchanged after irradiation.[133] This feature is qualitatively consistent with the slight decrease reported in optical absorbance after exposure to the proton beam. In Figures 3.9c and 3.9d, the normalized spectral intensity of each measured PL peak is reported

as a function of the proton fluence and the corresponding concentration of irradiated-induced vacancies that were determined within the CdS shell using the SRIM calculations presented in Figure 3.2. The intensity of the PL signal was obtained after subtracting the optical background contribution and numerical integration of the PL peak between 550 and 750 nm. As shown in Figure 3.9c, a 1.5 keV proton irradiation generates a slightly faster reduction of PL intensity than for the case of 10 keV. In Figure 3.9d, the linear decrease of the PL emission upon the concentration of vacancies generated by impinging protons inside the CdS shell indicates that the faster decrease reported for lower energy irradiations can be associated with the higher damaging rate and the greater nuclear collision cross-section between the 1.5 keV protons and the target atoms. Such a remark is consistent with the vacancy distribution calculated from SRIM-TRIM simulations in Figure 3.2a, as well as the nuclear stopping power presented as a function of the proton energy in Figure 2.4, where nuclear stopping power has a maximum value at 0.8 keV.

3.4.2 Evolution of PL lifetime after irradiation

The fluorescence decays of QDs under optical excitation at λ_{ex} = 444 nm are shown in Figures 3.11a and 3.11b. After proton irradiation, all PL lifetimes are found to decrease with the dose of implanted protons. The representative fluorescence decay curves of the PL peak centered at 627 nm of g-CS QDs were well fitted using triple exponential decay functions. The intensity-weighted average lifetime $<\tau>$ is estimated using the Eq. (2.7).[133-134] Before irradiation, the measured lifetime of as-prepared g-CS QDs is 66.6 ns. After 5×10^{15} H^+/cm^2 irradiation, the measured lifetimes decrease to 54.1 and 57.0 ns for 1.5 and 10 kV acceleration voltages, respectively. The normalized PL lifetimes of QDs after irradiation are plotted in Figure 3.11c and Figure 3.11d.

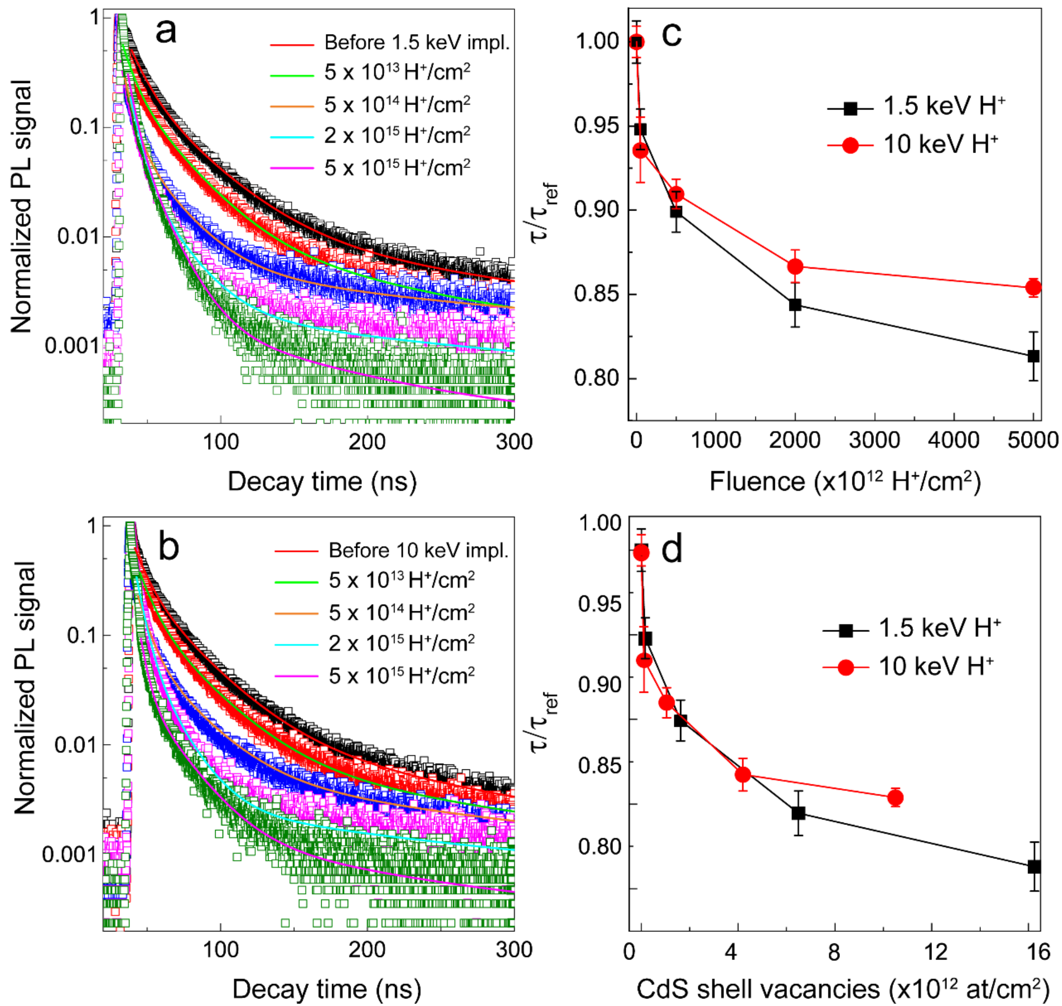

Figure 3.11 **Evolution of the PL decay. g-CS QDs under 1.5 keV (a) and 10 keV (b) proton irradiation; (c) dose-dependence of PL lifetime and its variation upon the surface density of CdS shell vacancies calculated by SRIM (d).**

As observed in Figure 3.9d for the variation of the PL intensity upon irradiation, a faster decrease of the average lifetime of photocarriers is observed after exposure to proton beams of lower energy in Figure 3.11d. Such a behavior is also qualitatively consistent with the higher formation rate of vacancies inside the g-CS QDs target for 1.5 keV impinging protons (Figure 3.2b and 3.2c). This confirms the role played by the

surrounding CdS shell on the g-CS QD luminescent properties, which is related to electron delocalization effects.[72, 115-116]

The variations of radiative decay rate (K_{et}) and non-radiative decay rate (K_{net}) after proton irradiations can be extracted from the fluorescence QY, which is related to the variations of lifetime measured by time-resolved PL spectroscopy,[81] as follows:

$$QY = \frac{K_{et}}{K_{et}+K_{net}}, \qquad \text{Eq. (3.1)}$$

where the measured lifetime is defined as:

$$\tau = \frac{1}{K_{et}+K_{net}} \quad . \qquad \text{Eq. (3.2)}$$

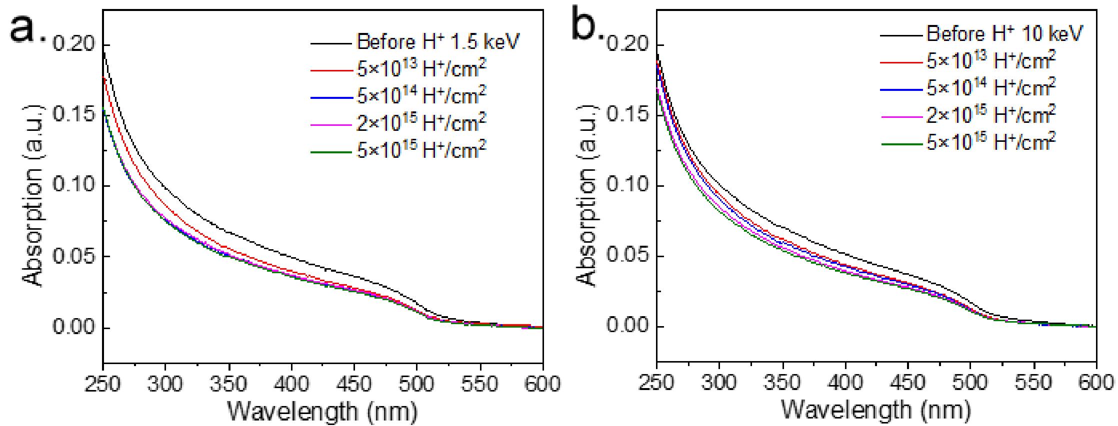

Figure 3.12 Evolution of the absorption spectral. g-CS QDs under 1.5 keV (a) and 10 keV (b) proton irradiation.

Based on the relative QY calculated through the variation of the measured PL intensities (Figure 3.9) and optical absorption (see Figure 3.12), the values of K_{et} and K_{net} can be calculated from equations (3.1) and (3.2). These results are shown in Figure 3.13, where the values of K_{et} are found to decrease with the proton fluence, while the values of K_{net}

increase. The higher non-radiative decay rate K_{net} arises from the formation of surface-defects/traps induced by ion/target atom collisions.[81, 114, 139] These surface-defects/traps will open up new non-radiative decay channels and highly affect the lifetime of photocarriers inside the core-shell heterostructure system. Ion irradiation experiments conducted on Si NPs [114] agree with our results, which also indicated that the decrease of PL intensity is accompanied by a concomitant lifetime quenching due to the rise of radiation-induced nonradiative phenomena. Even at a dose much lower than the one needed to amorphized Si, the Si NCs can lose their PL emission due to the radiation-induced damage. The occurrence of such effects is consistent with TEM images shown in Figure 3.6 and is also supported by SRIM simulations presented in Figure 3.2. This suggests that the nanocavities formed during irradiations can act as new non-radiative centers.

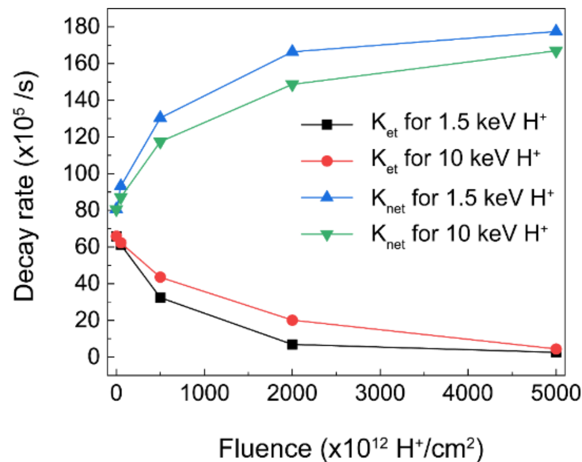

Figure 3.13 Evolution of K_{et} and K_{net} of g-CS QDs under proton irradiation.

In Figure 3.13, the increase of K_{net} is also found to be 10 % higher for 1.5 keV irradiations than for the ones at 10 keV. Such a variation is substantially lower than the increase by 30 % of the vacancies generated in samples exposed to a proton beam of lower energy.

This leads to two main observations: first, the number of non-radiative centers differs from the number of vacancies located within the medium;[139] second, the over damaging of the CdS shell shown for 1.5 keV proton irradiations (Figure 3.2b) should reduce the contribution of delocalized photocarriers to the PL emission process due to the generation of more non-radiative traps. This latter effect would be consistent with the results presented in Ref.[133] indicating that a fraction of about 40-50% of the optically excited photocarriers is delocalized over the whole core-shell systems and contributes to the increase in both global PL emission and average PL lifetime.

3.5 Effects of protons irradiation on photocurrent of g-CS QDs

3.5.1 Photoelectric properties analysis

The g-CS QDs were dispersed onto p-type Si substrates which are bounded to a copper plate using silver paste. In order to measure the effect of proton implantations on both the electrical properties and the photocurrent generation, the studied samples were covered by a 20 nm MoO_3 film, followed by a top Au electrode of 17 nm thickness. Both MoO_3 and Au layers were deposited by evaporation after ion exposure. To verify that the H^+ ions implanted into the QDs/Si targets did not contaminate or affect the chemical structure of the MoO_3 films,[140] their chemical composition has been investigated XPS measurements in non-implanted and implanted samples. As shown in Figure 3.14, no significant change is observed in the $3d_{5/2}$ and $3d_{3/2}$ valence bands of Mo. Both are found to be dominated by Mo^{6+} states. This agrees with the depth profiles of protons calculated by SRIM-TRIM simulations, which indicate most of the impinging protons go through the whole QDs.

The I-V curves of MoO_3/QDs/Si and MoO_3/Si systems under dark and one-sun solar-simulated illumination (AM 1.5G, 100 mW/cm^2) are presented in Figure 3.15, for applied BIAS voltages varying between -1.5 and +1.5 V. The Figures 3.15a and 3.15b correspond to samples containing QDs, before and after implantations performed at 1.5 and 10.0 kV, respectively. For each implantation energy, the doses of implanted protons were set to generate the same amount of vacancies inside the whole g-CS structure (Figure 3.2). Figures 3.15c and 3.15d are related to data recorded for pure silicon wafers exposed to similar proton beams.

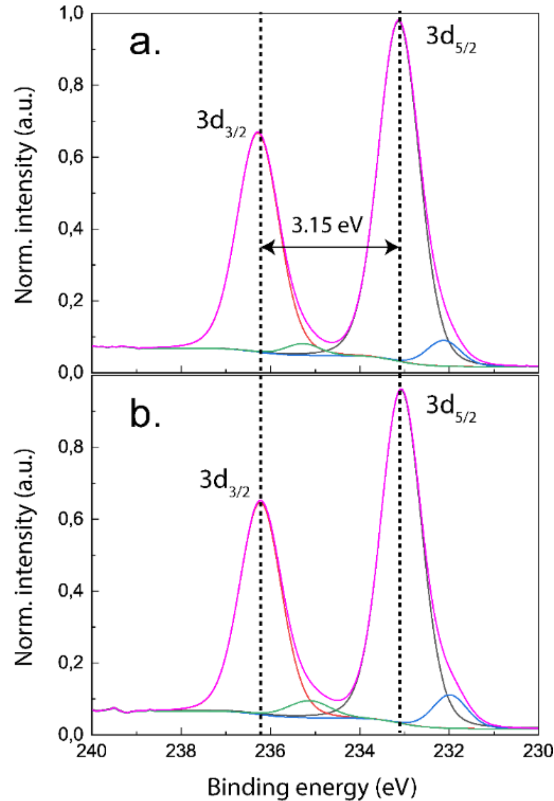

Figure 3.14 **Mo $3d_{5/2}$ and $3d_{3/2}$ XPS peaks of MoO_3 films covering QD/Si implanted at 10 kV with $1x10^{16}$ H^+/cm^2 (a) and non-implanted QD/Si (b).**

In the following discussion, the 'forward' (and 'reverse') BIAS polarization is defined as the positive (and the negative) terminals of the voltage generator connected with the

upper electrode. Accordingly, the right part of each figure related to applied voltages between 0.0 V and +1.5 V corresponds to forward bias I-V measurements, and the left one (between -1.5 V and 0.0 V), to the reverse ones, respectively. For all experiments conducted in dark conditions, the forward current passing through the MoO_3/QDs/Si or the MoO_3/Si systems is measured to be greater than the reverse current. A decrease in the reported values is also observed with the increase of the proton beam exposure. These two features appear to occur faster and/or to be more pronounced for implantations conducted at 1.5 kV and those conducted at 10.0 kV. For I-V curves obtained under illumination, the measurements strongly differ in the presence and absence of g-CS QDs. Two remarkable and very distinct trends are reported. First, almost no reverse biased photocurrent is detected in MoO_3/QDs/Si samples (left parts of Figures 3.15a and 3.15b), whereas a strong current is observed in the MoO_3/Si systems (left parts of Figures 3.15c and 3.15d). Second, while all measured photocurrents are found to decrease with the proton dose in implanted MoO_3/Si (Figures 3.15c and 3.15d), these photocurrents are found to increase continuously with the H^+ fluencies in MoO_3/QDs/Si (Figures 3.15a and 3.15b). This latter effect is highlighted by the four vertical arrows (in yellow) that have been directly reported in Figure 3.15.

The degradation of the biased current after proton-beam exposures and the decrease of its related photocurrent is consistent with the increase of structural “modification” and optical delocalization, both presented in the previous section. In such a scenario, the observed losses may result from the increase of current leaks in the conduction and valence bands of irradiated QDs, as well as in the upper part of the Si substrate where implanted protons are located. Nevertheless, a more detailed clarification is needed to

explain the difference in forward and reverse currents, as well as the significant improvement of the photocurrent generation reported for MoO_3/QDs/Si systems on Figures 3.15a and 3.15b.

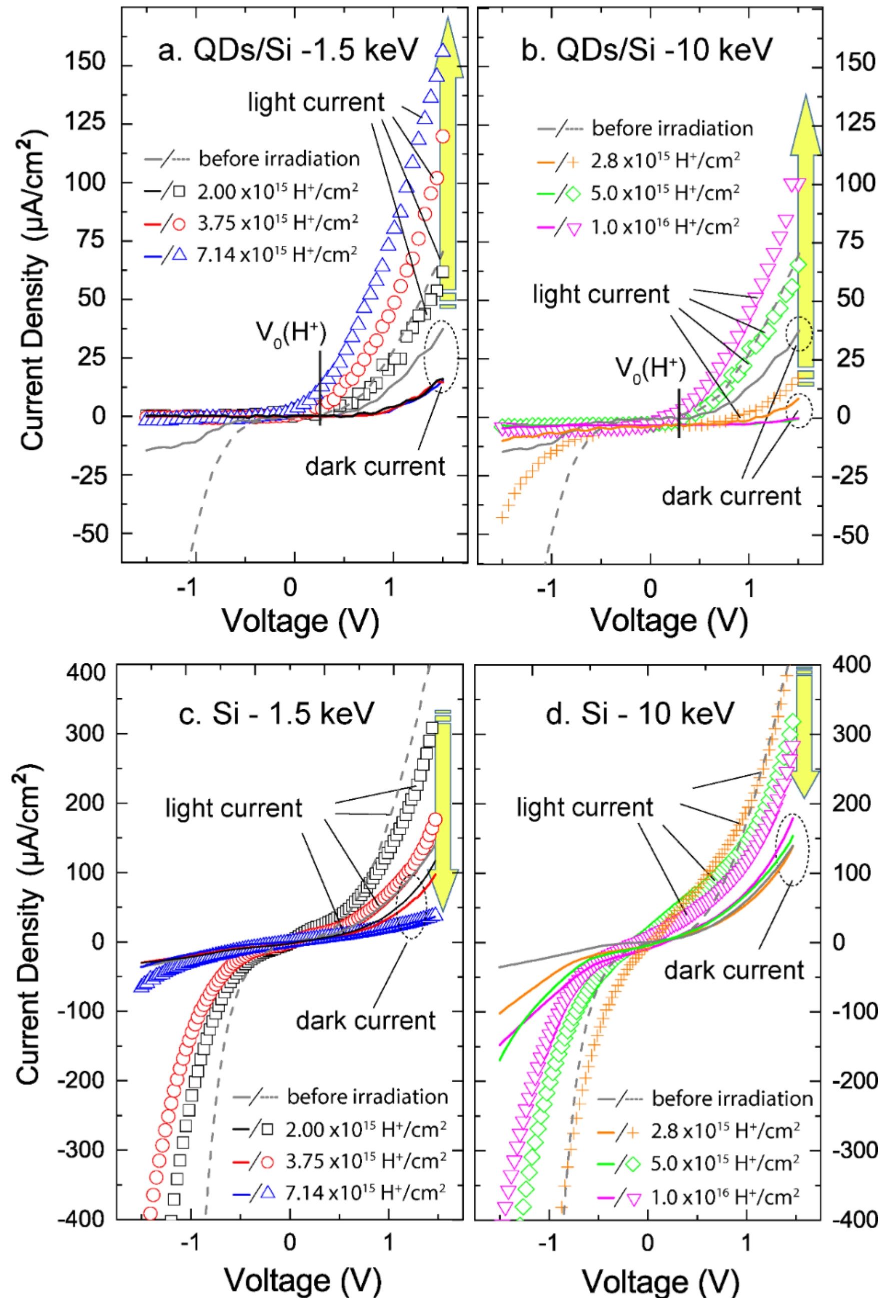

Figure 3.15 **I-V characteristics of MoO_3/QDs/Si and MoO_3/Si under dark and illumination, for QDs implanted at 1.5 kV (a) and 10.0 kV (b), as well as Si substrates implanted at 1.5 kV (c) and 10.0 kV (d).**

3.5.2 Bandgap alignment in MoO_3/QDs/Si systems

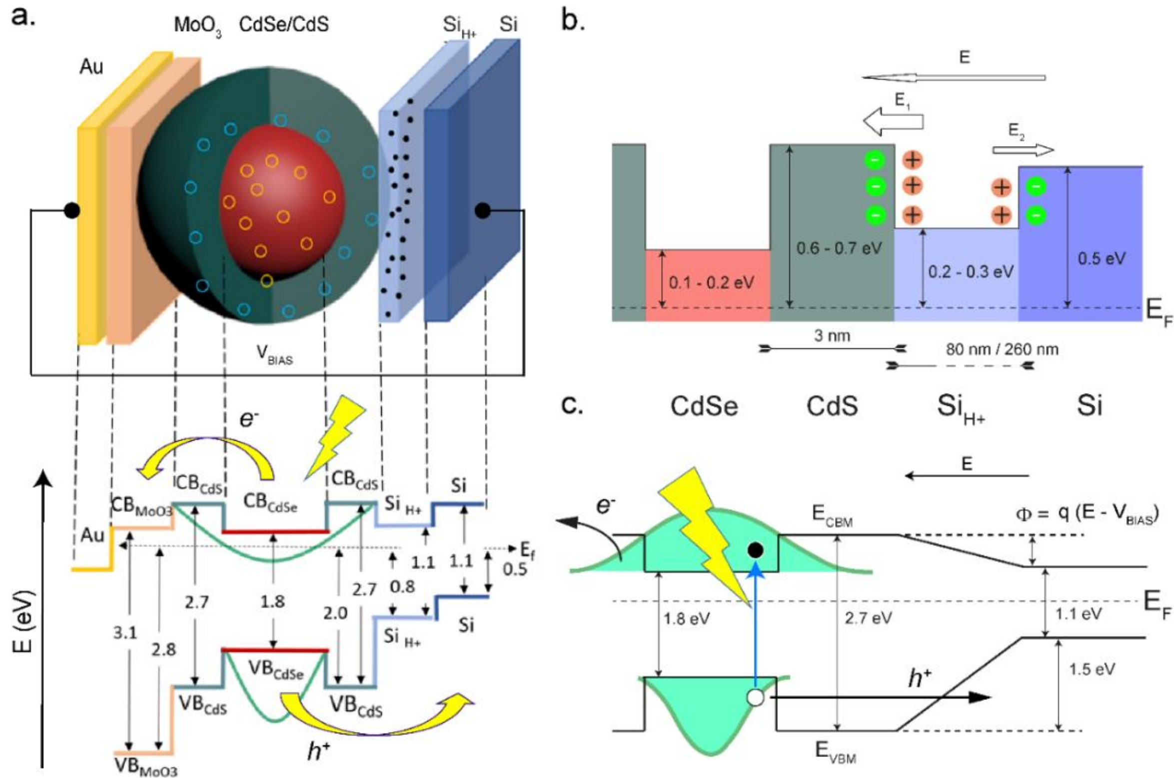

Figure 3.16 **(a) Schematic bandgap alignment along the Fermi level in MoO_3/QD/Si systems containing g-CS QDs, (b) donor/acceptor redistribution at CdS/Si-H and Si-H/Si interfaces leading to local electric fields E_1 and E_2. (c) Equivalent potential downshift, Φ given upon E = E_1-E_2 and the biased voltage, VBIAS, with the enhanced photovoltaic process due to the delocalization of conduction electrons in the g-CS system.**

In Figure 3.16a, we propose a complete description of the bandgap alignment occurring in MoO_3/QDs/Si systems, based on previous investigations conducted on g-CS QDs,[72] as well as UPS measurements carried out in silicon substrates before and after exposure to different H^+ beams (shown in Figure 3.17). On the left of Figure 3.16a, the type-II

heterojunction between MoO_3 and the CdS shell of the QDs is comparable to the bandgap interfaces of TiO_2/CdS[72] and bulk MoO_3/CdS layers found in the literature,[141-142] for given bandgap energies of 3.1 eV and 2.7 eV, in MoO_3 and CdS, respectively. The bandgap of the CdSe core is 1.8 eV, in agreement with the expected PL spectra presented in Figures 3.9a and 3.9b.[72, 143] A type-I junction is formed between the bottom side of the CdS shell and the top surface of the implanted Si layer, which has an indirect bandgap of 1.1 eV.[144] As the generation of bi-vacancies in implanted Si is known to increase the concentration of donor states inside the medium,[141] the increase of the valence band edge and the slight decrease of the sample work functions reported in Figure 3.16 indicate that the band structure of the Si substrate exposed to proton bombardment is upshifted by 0.2 to 0.3 eV with respect to one of non-implanted Si. The junction between the implanted Si layer (labeled 'Si_{H+}' on the figure) and non-implanted Si region located deeper than several hundreds of nm is assimilated to a type II energy barrier, as illustrated in the right part of Figure 3.16(a) and zoomed in Figure 3.16(b). According to SRIM calculations,[9] the thickness of the Si_{H+} layer is about 80 nm and 260 nm for 1.5 keV and 10.0 keV ion beams, respectively. For the whole system, the bandgap alignment is set with respect to the Fermi level shown by the horizontal dashed line on Figures 3.16(a)-(c).

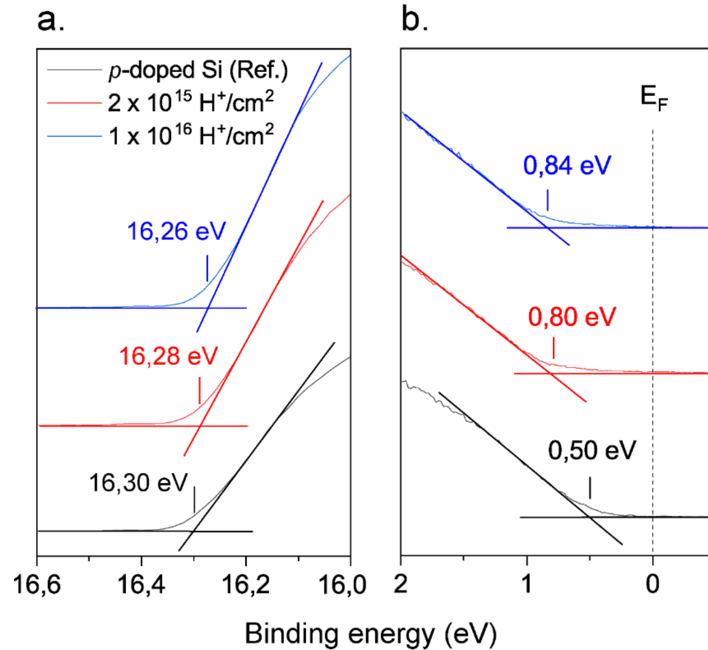

Figure 3.17 **(a) UPS analysis of the reference Si substrate and Si implanted with 10 keV protons at ion doses of 2x10^{15} H^{+}/cm^{2} and 1x10^{16} H^{+}/cm^{2}. Secondary electron cut-off (a) and valence band edge (b) regions.**

3.5.3 Photocarrier transfer between different layers

The presence of the CdS/Si_{H+}/Si interface can explain the evolution of I-V curves in reverse and forward polarizations. The lower value of the conduction band minimum in the Si_{H+} sublayer and the higher value of its valence band maximum create energy barriers for electrons passing through the implanted Si layer towards the CdS shell or the Si substrate. These barriers generate two local electric fields of opposite directions (labeled E_1 and E_2 in Figure 3.16b) resulting from the equilibrium of the donor/acceptor distributions across the Si_{H+}/Si and Si_{H+}/CdS junctions. The Si_{H+}/CdS interface has an energy barrier of about 0.5-0.6 eV, which is twice the one of Si-H/Si (~ 0.3 eV). In the first approximation, the total contribution of charge carrier redistribution can be averaged

inside the Si_{H+} ‘buffer’ layer as a positive electric field, E, oriented normal to the Si substrate (Figure 3.16b). In the right part of Figure 3.16c, a schematic representation of the CdS/Si_{H+}/Si heterojunctions is presented.

For reverse BIAS, the average energy barrier potential between the CdS core and the Si substrate: $\Phi = q(E - V)$ increases, so that the charge carrier transfers between QDs and Si decreases and the current passing through the MoO_3/QDs/Si system is reduced. These effects are evidenced in the left parts of Figures 3.15a and 3.15b, where reverse biased current densities are lower than 1.0 μA/cm^2. Conversely, the forward polarization favors the current flow through the device by reducing the energy barrier Φ. This feature leads to higher forward bias conductivity, as seen in Figures 3.15a and 3.15b. The applied voltage for which $\Phi = 0$ eV (labeled $V_0(H^+)$ on Figures 3.15a and 3.16b) refers to acceleration tension thresholds varying between +0.1 V and +0.2 V, above which forward biased current densities higher than 10 μA/cm^2 are recorded. Although this quantity was not found to vary continuously with the irradiation dose, its value should depend on the concentration of structural defects induced by proton bombardment.

The strong discrepancy between forward and reverse polarizations is not observed in MoO_3/Si systems without g-CS QDs. For this set of samples (Figures 3.15c and 3.15d), the measurement of greater reverse biased currents reveals the formation of a type-II junction between MoO_3 and Si_{H+}, as already stated for bulk MoO_3/Si heterojunctions.[144] After implantation, the presence of structural defects inside the Si substrate is found to have a limited impact on the I-V characteristics, because the conduction band minimum and the valence band maximum of the Si_{H+} sublayer remain always greater or equal to the ones of MoO_3 (Figure 3.16a).

3.5.4 Enhanced photocurrent in MoO_3/QDs/Si systems

Under one sun illumination, the photocurrent generation process occurring in MoO_3/QDs/Si systems is described in Figure 3.16c. As calculated by Selopal *et al*. in CdSe/CdS,[72] the excitons created inside the CdSe/CdS QDs are made of electrons whose spatial wavelength function is delocalized over the core-shell CdSe/CdS conduction band, and holes that are located within the valence band of the CdSe core. It also has been demonstrated that the increase of the CdS shell thickness reduces the electron-hole spatial overlapping and enhances the recombination time of these excitons. In g-CS CdSe/CdS, the electron in the conduction band of the QDs can transfer to the conduction band of their neighboring semiconductors more efficiently, due to the dissociation of the excited electron-hole pairs.[145] In proton irradiated g-CS systems, where the PL emission and optical properties of QDs indicate the occurrence of stronger delocalization effects, we infer that the presence of an increasing number of non-radiative structural defects favors electron exchanges between the superimposed and overlapped wavefunctions of the CdSe/CdS conduction bands. This enhanced electron delocalization over the core-shell system promotes the electron-hole pair separation induced by charge carrier transfers inside and at the QD interfaces. Such a feature would explain the generation of stronger forward light currents reported in Figures 3.15a and 3.15b, as well as the continuous increase of the current density upon the dose of implanted protons. From the variation in the forward current measured with an applied voltage of +1 V under solar illumination in irradiated systems, we found a significant increase in photocurrent density relative to the current density measured in non-implanted MoO_3/QDs/Si. This enhancement is higher than 100 % for QDs exposed to 1.5 keV protons that generate

stronger structural and optical changes in the materials, and around 50 % for 10 keV proton bombardments. Nevertheless, the QDs spread on the Si wafer before implantation and the deposition of MoO_3 do not form a homogenous layer of uniform thickness. The measurements conducted in MoO_3/QDs/Si samples and presented in Figures 3.15a and 3.15b also account for the contribution of MoO_3 that was directly deposited on the Si wafer or the Si_{H+} sublayer, due to the spacing existing between each QD. This makes thus impossible a precise quantification of both the photocurrent generation in QDs and its improvement caused by their proton irradiations. In any case, the fact that the light current increases in MoO_3/QDs/Si despite the presence of direct contact between MoO_3 and the Si_{H+}/Si layers that should contribute to its attenuation (as observed in samples containing no QD, Figures 3.15c and 3.15d), highlights the occurrence of enhanced photocurrent generation in irradiated g-CS QDs. These results also indicate that proton-based treatments can be implemented to modify both the interface and the structure of semiconductors. The proton treatments can be achieved by plasma immersion ion implantation which is a lower-cost implantation technique than traditional beam line implantation due to its simpler design, lower operating costs, and ability to run high doses (10^{14} – 10^{18} ions/cm^2) at low ion energies (20 eV – 10 keV).[146] Our study not only provides a better understanding of the proton irradiation effects on nanoscale devices, but it also promotes new technological routes based on wavefunction engineering to develop photovoltaic components with better light-to-current conversion efficiency, in particular, and tune the physical properties of QDs, in general.

3.6 Summary

In summary, we report the damaging effects of proton irradiations on the structural and optical properties of g-CS QDs. The SRIM Monte Carlo simulation demonstrated that the vacancies created in the shell by 1.5 keV proton irradiations are 30% higher than that of 10 keV proton irradiations. TEM investigations revealed the formation of nanocavities in QDs by proton irradiation, which are both found to increase with the dose of implanted protons. These TEM micrographs are the first evidence to confirm that proton irradiation can lead to the formation of nanocavities in QDs. PL and PL decay measurements demonstrated that both PL intensity and PL lifetime of the as-prepared QDs decrease linearly with the concentration of structural defects generated by impinging protons through the CdS shell. When more vacancies are created in the shell by the proton beam, the PL intensity and lifetime decrease faster. Such results give an original and detailed description of the proton irradiation effects on g-CS QDs as a function of the irradiation parameters. Using I-V measurements conducted in dark and light environments the exposure of g-CS QDs to proton irradiations is found to promote the photocurrent generation. This feature is associated with the delocalization of photoelectrons in the CdS shell, whose improvement with the formation of non-radiative structural defects inside the implanted QDs favors the electron-hole pair separation in g-CS QDs. In addition to providing physical insight regarding charge carrier exchanges, bandgap alignment and exciton dissociation in systems containing g-CS QDs, such a wave function engineering based on ion-implantation treatments generates new potential applications in energy conversion and optical tuning, as well as in the development of new functional nanomaterials.

4 EPITAXIAL GROWTH of HETEROSTRUCTURED QUANTUM DOTS AND DEFECTS REPAIR BY e-BEAM

4.1 Motivation

Heterostructured quantum dots (hetero-QDs) with outstanding properties can be used in various optoelectronic devices. Depending on the chemical compounds, size of core and shell, hetero-QDs can exhibit Type I, Type II, or quasi-Type II junction,[147-150] In order to promote the growth of shell and avoid interface defects, the core and shell components are generally chosen with the same crystal structure and small lattice mismatch.[149] Besides the defects located at the interface, screw dislocation, edge dislocation and stacking faults are frequently observed, especially in zinc blend (ZB) QDs.[151] These structural defects formed during the synthesis process can facilitate charge trapping. It is shown that some defects can be efficiently restored through heat treatment. However, many types of QDs, such as CdSe/CdS[152] and MnS/ZnS[153], tend to degrade at temperatures about several hundred degrees. Therefore, it is necessary to develop a new method to eliminate these structural defects.

In this chapter, the particle size, the three-dimensional (3D) shapes of $CuInSe_xS_{2-x}$/CdSeS/CdS hetero-QDs synthesized through a facile two-step method were studied by TEM. A detailed analysis of the epitaxial relationship between $CuInSe_xS_{2-x}$/CdSeS core and CdS shell was conducted using extensive HRTEM observations. *In situ* HRTEM observations show that the screw dislocation inside the hetero-QDs can be efficiently repaired by e-beam irradiation, whereas the stacking fault remains unchanged, even under e-beam exposure up to 20 min. These results may help to design hetero-QDs with high-quality interfaces and identify strategies for synthesizing defect-free hetero-QDs.

Some of the work described in this chapter has been previously published in Nanoscale, 11 (41), 19529-19535, 2019.

4.2 Morphology of $CuInSe_xS_{2-x}$/CdSeS/CdS hetero-quantum dots

4.2.1 2D outlines of hetero-QDs in TEM

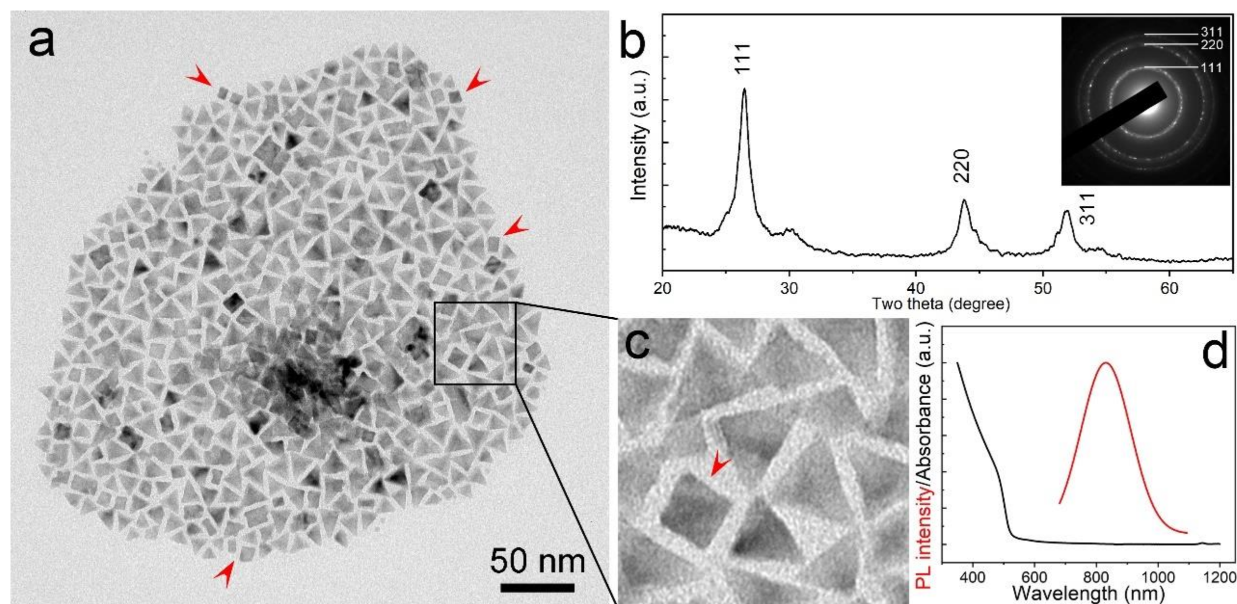

Figure 4.1 **BF image (a), XRD pattern (b), UV-VIS and PL spectrum (d) of ClSeS/CdSeS/CdS hetero-QDs, (c) corresponds to the rectangular region in (a), inset of (b) is the SAED pattern.**

Figure 4.1a shows typical ClSeS/CdSeS/CdS hetero-QDs TEM micrographs with × 50,000 magnification. The formed core/shell QDs display two-dimensional (2D) outlines, resulting from a combination of triangles and squares. The number of QDs with triangular 2D outlines is found to be significantly greater than the number of square QDs. Considering the different 2D outlines observed in TEM images, we infer that the morphology of the QDs can be consistent with regular tetrahedrons. The verification for

both the tetrahedral shapes and the crystal facet determination of the QDs are discussed in more detail in the following section.

According to statistical analysis of around 200 individual QDs, the average edge length (a) of QDs is 14 nm with a mean squared error of 2 nm. The volume (V) of the regular tetrahedron can be calculated as following:

$$V = \frac{\sqrt{2}}{12} a^3 \qquad \text{Eq. (4.1)}$$

The volume of as-synthesized g-QDs calculated by Eq. (4.1) is 320 ± 50 nm^3. This latter quantity is equivalent to spherical QDs having an average diameter of 8.5 nm. Figure 4.1b refers to the x-ray diffraction (XRD) and SAED patterns taken from the QDs shown in Figure 4.1a, which can be indexed using the lattice parameters (a = 5.82) of CdS (PDF No. 00-001-0647). The as-synthesized hetero-QDs exhibit strong absorption in the UV-VIS region (below 500 nm) and PL emission at 830 nm,[137] as evidenced in Figure 4.1d. The PL spectra of hetero-QDs recorded at different growth stages are presented in Figure 4.2, showing significant energy shifts of their PL emission peak related to their change in size and chemical composition. In the beginning, the CISeS QDs exhibits a typical emission peak at 957 nm. After adding 2.5 ml of Cd and S precursors, a significant blue shift (from 957nm to 830 nm) is measured. Such a blue shift is attributed to the decreasing size of CISeS due to the core-etching effect at the early growth stages.[137] Then a slight shift of the PL peak is shown in Figure 4.2, which is caused by electron delocalization effects induced by the growth of the CdSeS and CdS shells.

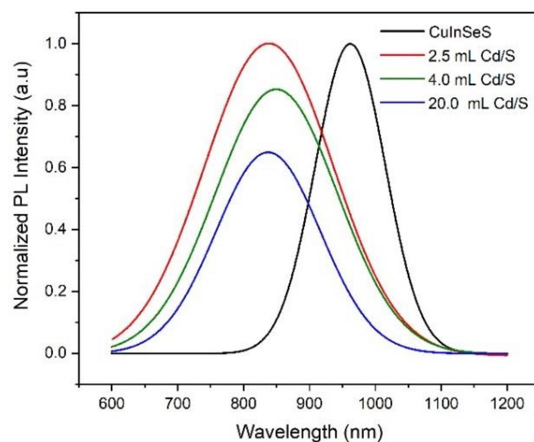

Figure 4.2 PL spectra of heterostructured CISeS/CdSeS/CdS g-QDs at different growth stages.

4.2.2 Hetero-QDs observed along different zone axes

Figure 4.3a shows a hetero-QD having an equilateral triangle shape and atomic cross-fringes with a measured d-spacing of 2.06 Å, which is associated with the $\{220\}$ planes of ZB CdS. This suggests that this particle is viewed along the [111] zone axis. When observed along the [112] and [110] zone axes (Figure 4.3b and 4.3c), the QD appears as an isosceles triangle whose apex angles of 63° and 71° are consistent with theoretical values of 62.96^{o} and 70.5^{o}.[154] The d-spacing of the crystal plane presented in Figure 4.3b is measured to be ~3.36 Å and ~2.06 Å with an angle of ~90°, corresponding to the (111) and (220) plane families of ZB crystal structure of CdS, respectively. Figure 4.3c shows the particle viewed along the [110] zone axis and displaying the $\{111\}$ planes. The cross-fringes in this projection exhibit an angle of 71° (Figure 4.3c), which is in agreement with the theoretically calculated value of 70.5°.[154] A low proportion ($\sim$10%) of QDs is observed with square projections (Figure 4.3d). When viewed along the [001] zone axis, these particles have rectangular cross-fringes from their $\{200\}$ plane families with

measured d-spacings of 2.9 Å. In addition, both the 2D outline of QDs shown in the HRTEM image and the corresponding FFT pattern perfectly match the atomic model in the corner of each figure. The included angles between different zone axis indicated in Figure 4.3 are consistent with the rotation angles of the tetrahedron in the corner. For example, the included angle between [111] and [001] is 54.73°, which is equal to the rotation angles between the tetrahedron lying on their base (Figure 4.3 a) and the tetrahedron lying on their edge (Figure 4.3 d). In the TEM observations, the 2D projections of tetrahedral QDs are equilateral triangles for QDs lying on their base and rectangles for the QDs lying on their edge, respectively. These results demonstrate and validate experimentally the 3D shape of CISeS/CdSeS/CdS unequivocally, as well as their crystal facets and their atomic orientations.

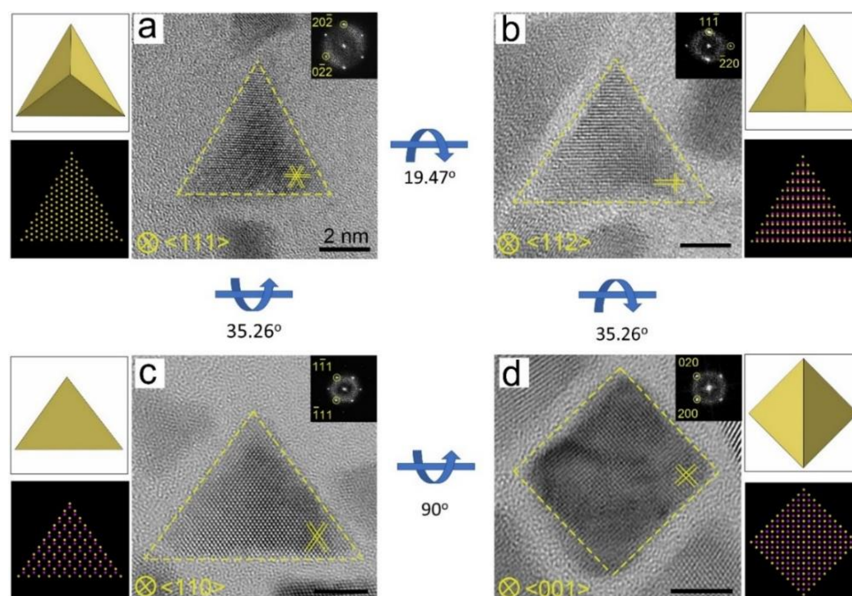

Figure 4.3 **HRTEM images of CISeS/CdSeS/CdS hetero-QDs. Each of the four panels (a-d) is composed of one representative HRTEM image for an isolated QD with a given projection, the corresponding FFT pattern of the HRTEM image (inset), the sketches and the atomic model. The detailed rotation modes between different zone axes are indicated by the blue arrows. (a)-(d) show the QDs viewed along <111>, <112>, <110> and <001> zone axes, respectively.**

4.3 Growth mechanism of hetero-quantum dots

4.3.1 Growth of hetero-QDs

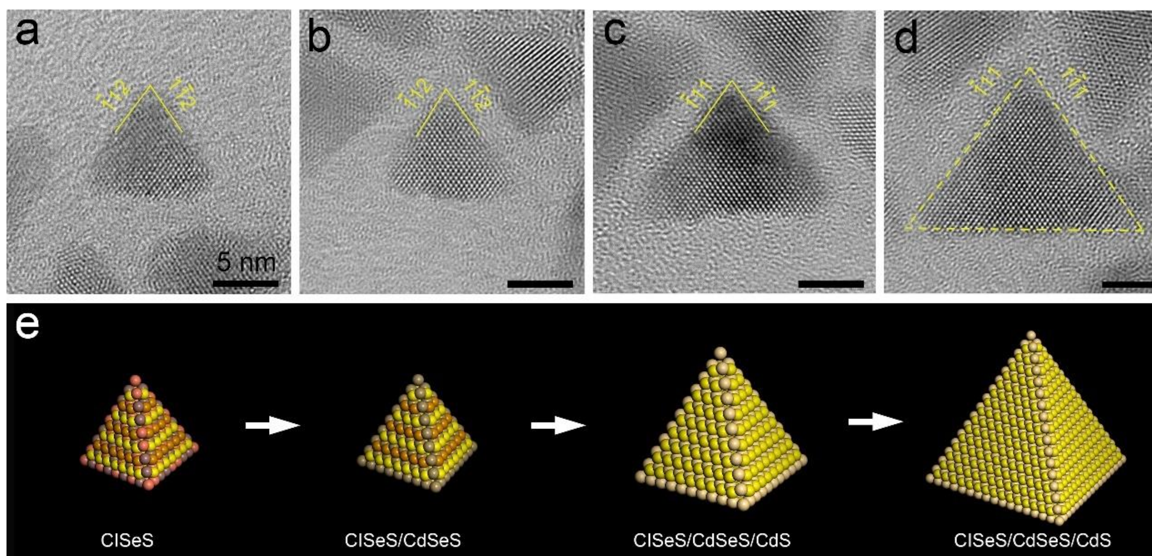

Figure 4.4 (a) HRTEM image of CISeS core; (b-d) HRTEM images of the hetero-QDs formed at different growth stages.

To investigate the growth mechanism of hetero-QDs, intermediate products formed at different growth stages were extracted and observed by HRTEM. Figure 4.4a shows atomic cross-fringes with a measured d-spacing of 3.25 Å, related to the $\{112\}$ planes of CISeS core (PDF No. 00-036-1311), which is consistent with the SAED pattern presented in Figure 4.5a. After injection of 2.5 mL Cd/S precursors, a thin layer of CdSeS was grown on the surface of CISeS core by the cation exchange process. In the meantime, the size of QDs is found to slightly decrease due to the cation exchange at the early stages of growth, which is also evidenced by the significant blue shift of their PL emission peak presented in Figure 4.3. The atomic cross-fringes in Figure 4.4b and the SAED pattern of Figure 4.5b still consist of CISeS structures, having a d-spacing of 3.3 Å that is slightly greater than the one measured in Figure 4.4a (3.25 Å). Such an expansion results from

the growth of CdSeS, whose structural lattice has a larger d-spacing than that of CISeS.[137]

After injection of 2.5 mL Cd/S precursors, the EDS spectra shown in Figure 4.6 reveal the presence of an additional peak related to Cd, which may result from the cation exchange between Cd and Cu/In. At the early growth stage, only several atomic layers of CdSeS form at the surface of the CISeS core, therefore the crystal structure of QDs still remains unchanged. With the volume of the injected Cd/S precursor increases, the deposition of CdS onto the surface of CISeS/CdSeS core increases the size of the synthesized crystallite, as shown in Figure 4.4c. The average size of hetero-QDs increases from 6.4 ± 0.5 nm to 7.4 ± 0.5 nm. In the meantime, the d-spacing also further expands to 3.33 Å. When the volume of injected Cd/S precursor reaches 20 mL, the d-spacing is 3.36 Å (Figure 4.4d), which is equal to the d-spacing in CdS (PDF No. 00-001-0647).

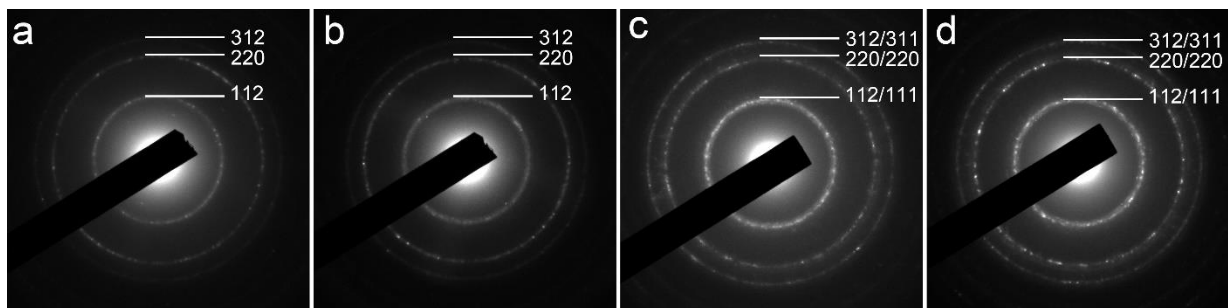

Figure 4.5 SAED of heterostructured CISeS/CdSeS/CdS g-QDs at different growth stages. (a) CuInSeS QDs, (b) (c) and (d) is the products after injection Cd/S precursor of 2.5 mL, 4 mL, and 20 mL, respectively.

The intensity of Cd peak also increases with the injection volume of Cd/S precursors. (Figure 4.6) The concentration of Cu, In, Se, S, and Cd found in hetero-QDs TEM samples was measured by EDS. The data reported in Table 4.1 show that the density of both Cd

and S increases continuously with the injection of the Cd/S precursor. These features are consistent with the growth process proposed herein, stating that the thickness of both the inner CdSeS and outer CdS shells increase with the volume of injected precursor.

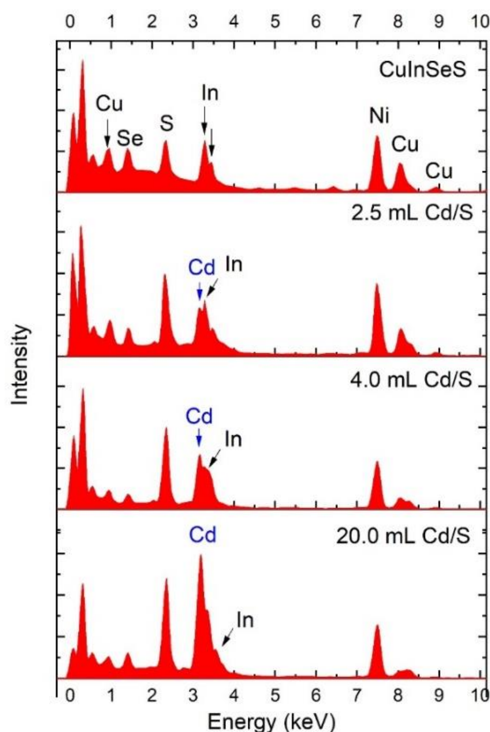

Figure 4.6 **EDS spectra of heterostructured ClSeS/CdSeS/CdS g-QDs at different growth stages.**

Table 4.1 **Atom concentration obtained from EDS analysis.**

	Cu (Atomic%)	**In (Atomic%)**	**Se (Atomic%)**	**S (Atomic%)**	**Cd (Atomic%)**
CuInSeS	24±3	22±3	24±3	30±4	0
2.5 mL Cd/S	15±2	21±3	11±1	33±5	20±3
4.0 mL Cd/S	10±1	13±2	9±1	40±6	29±4
20.0 mL Cd/S	5±1	3±1	8±1	41±6	44±6

4.3.2 Epitaxial relationship between core and shell

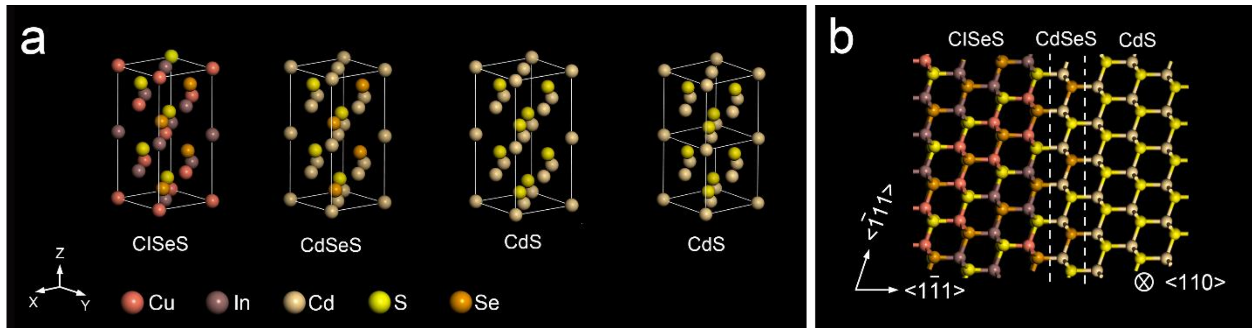

Figure 4.7 **(a) is the unit cell of CISeS, CdSeS, and double unit cell of CdS; (b) the interface of the CISeS, CdSeS, and CdS viewed along <110> zone axis.**

Different from many other types of hetero-QDs (CdSe/CdS,[150] InP/ZnS[155]) which have the same crystal structure, the as-synthesized CISeS/CdSeS/CdS hetero-QDs have a core of tetragonal lattice structure surrounded by a shell of the cubic lattice structure. The HRTEM analysis from Figure 4.4(a-c) indicates that the epitaxial relationship between core and shell is $[110]_{\mathrm{core}}//[110]_{\mathrm{shell}}$, $\{112\}_{\mathrm{core}}//\{111\}_{\mathrm{shell}}$. Usually, large amounts of misfit dislocations will appear at the interface of different crystals, due to the lattice mismatch.[156] However, such misfit dislocations are not observed in the as-synthesized CISeS/CdSeS/CdS hetero-QDs. We infer that this feature can result from the lattice parameters and the atomic arrangement of the CISeS and CdS crystals. As CISeS has a tetragonal structure with crystal cell parameters of a=b=5.666, c=11.317, α=β=γ=90°, and CdS has a cubic structure with crystal cell parameters of a=b=c=5.820, α=β=γ=90°, the double unit cell of CdS is a=b=5.820, c=11.64, which is quite close to the unit cell of CISeS. (Figure 4.7a) The lattice mismatch between CdS and CISeS is only 2.7%. To enable the epitaxial growth of one crystal ‘A’ to one crystal ‘B’, except for small lattice mismatch, the atomic arrangements also need to be considered. As shown in Figure 4.4a

for the CdSeS unit cell, Cd atoms occupy the same position of Cu and In ions in the CISeS unit cell. After the injection of Cd/S precursor, the Cu and In ions in the surface of CISeS core are replaced by Cd through the cation exchange process without any crystal structure deformation (Figure 4.7b). With the increasing volume of Cd/S precursor, the new layer of CdS can epitaxially grow on the surface of the core. According to the HRTEM images of the hetero-QDs at different growth stages (Figure 4.4a-4.4d) and shape analysis (Figure 4.3), the preferential growth direction is [111]. This also agrees with the general sequence of surface energy in ZB structure: $\gamma\{111\} < \gamma\{100\} < \gamma\ \{110\}$.[157] As the double CdS unit cell is similar to the CISeS unit cell, (Figure 4.4a) the CdS shell can epitaxially grow on the core layer by layer. As the lattice mismatch between CdS and CISeS is only 2.7%, there is one misfit dislocation every 37 planes. The diameter of the core is ~6.4 nm, which contains about twenty {111} planes. Obviously, the size of QDs is not large enough to form one misfit dislocation at the core-shell interface. The atomic model along [110] zone axis in Figure 4.7 (b) is consistent with our HRTEM results and the aforementioned analysis, showing a quasi-perfect atomic ordering at the interfaces between CISeS, CdSeS, and CdS without any crystal structure deformation. The SAED patterns (Figure 4.5) of hetero-QDs at different growth stages are also consistent with our HRTEM results. No additional diffraction ring is found during the process, which means that the atoms contained in the core and the shell remain perfectly aligned, as expected for epitaxial growth.

4.4 Defects in CISeS/CdSeS/CdS hetero-QDs

4.4.1 Stacking faults and twin boundaries

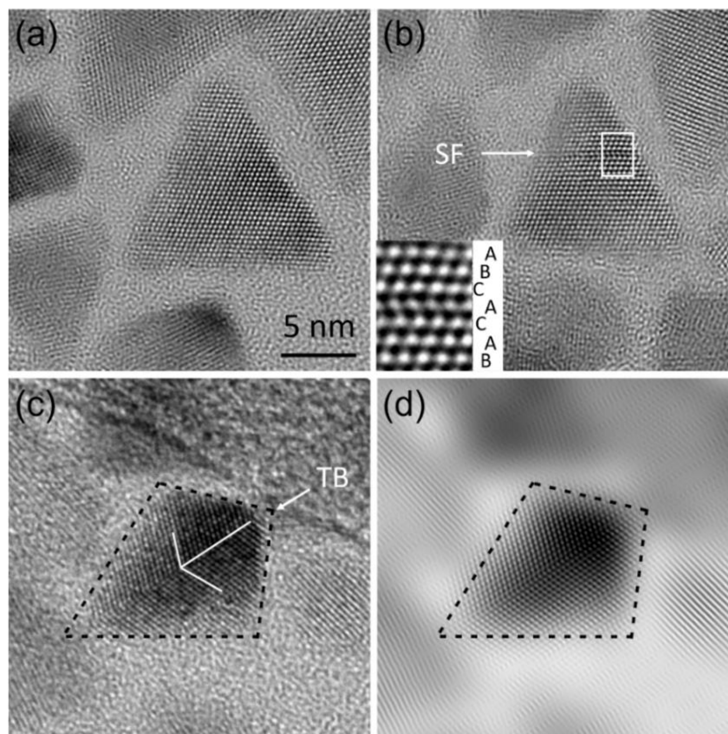

Figure 4.8 **HRTEM images of CISeS/CdSeS/CdS hetero-QDs. (a) perfect hetero-QDs, (b) hetero-QDs with stacking faults, (c) hetero-QDs with twin boundaries, and (d) FFT filtered image of (c).**

Extensive HRTEM micrographs (Figure 4.4 a-d and Figure 4.8 a) show that no misfit dislocation forms at the interface of the as-synthesized hetero-QDs. However, other types of structural defects, such as SF and twin boundaries, appear in these hetero-QDs. This kind of defect is endemic in NPs,[52-53, 151, 158] especially for multilayered materials of different chemical compositions. In the studies of Pt NPs,[151] edge and screw dislocations were observed at the atomic scale using electron tomography. In other previous studies conducted on Si NPs,[52] intrinsic and extrinsic SF was also analyzed by HRTEM. According to the analysis of Figure 4.7, the CISeS/CdSeS/CdS hetero-QDs can be seen

as quasi-ZB structures. Figure 4.8 (b) shows one QD with SF, which can be formed by the removal of the lattice plane B. From the enlarged figure shown in the lower-left corner of Figure 4.8 (b), we also notice the occurrence of a perfect crystal lattice plane sequence transfer from "…ABCABCABC…" to "…ABCACABC…". Due to the missing lattice plane B, this type of SF also can be identified as a local hexagonal-closed-packed (HCP) structure.[52] The hetero-QDs shown in Figure 4.7 (c) have a TB, which can be clearly seen in the FFT filtered image (Figure 4.8 d). The formation of such TB can be explained by the coalescence of two small NPs during the formation of the surrounding shell. Similar coalescence behaviors have been widely observed in Si NPs embedded in fused silica and prepared by ion implantation.[53]

4.4.2 Screw dislocations repaired by e-beam irradiations

Besides SF and TB, the screw dislocation is also observed in the hetero-QD. Figure 4.9a shows a typical screw dislocation and SF located in the middle and top of the hetero-QD, respectively. These structures can lead to the formation of surface-defects/traps that affect the photoelectric and luminescence properties of QDs.[152, 159] Many efforts have focused on preventing the formation of such defects in QDs.[160] The micrographs recorded for samples exposed to a 200 kV e-beam for durations reported on their top right are presented in Figure 4.9. After 15 min of e-beam irradiation, the screw dislocation observed in the middle of the hetero-QDs was almost completely repaired, whereas the SF located at the top remained unchanged, even after 20 min of e-beam exposure. According to atomistic simulations, more energy is required to repair planar defects (SF) than linear defects (screw dislocation).[161]

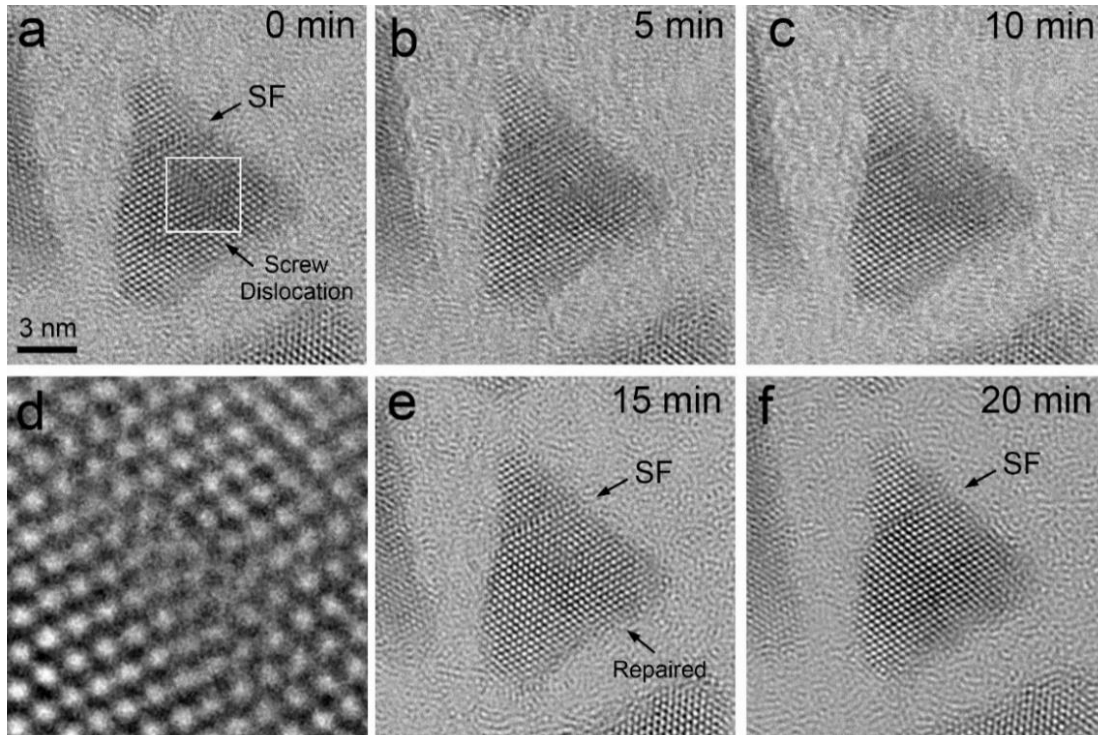

Figure 4.9 **Evolution of defects under e-beam exposure observed by *in situ* HRTEM. (a) HRTEM image of hetero-QDs at the beginning; (b), (c), (d), and (e) are hetero-QDs under e-beam exposure of 5 min, 10 min, 15 min, and 20 min, respectively; (d) corresponds to the rectangular region in (a). The radius of e-beam during observation is ~30 nm.**

4.5 The temperature under e-beam irradiation

As inelastic scattering involves 'successive interactions' between the incoming electrons and the sample electrons during TEM observations, the temperature of the materials increases locally.[162] Since atoms can thermally diffuse, this local heating becomes a driving force that can displace the screw dislocation towards the surface of the QD.[163] To estimate the temperature during our *in situ* observations, we can use the melting point of carbon film as a reference[164]. A similar method has been applied to detect the local temperature during the Joule heating of a carbon nanotube using W, Fe, and Al_2O_3 particles.[164-165] Carbon nanotubes were found to withstand temperatures increasing up

to the melting point of tungsten NP, around 3400 K.[164] In our experiments, we first reduced the e-beam diameter to reach the melting point of carbon film, then we increased the e-beam size until it reaches the value that was set for the *in situ* observations of Figure 4.9. The local temperature was then determined from the ratio between the two different beam current densities, for a total e-beam current of 8.0 nA, which was measured using a Faraday cup. As shown in Figure 4.10b, the QD started to evaporate immediately under an e-beam focus of ~7 nm radius (current density of ~ 500 A/cm^2). The whole QD is found to entirely evaporate after 20s e-beam exposure. The corner of QD also evaporated without direct e-beam exposure, which suggests that the local temperature was much higher than the melting point of CdS. After 30s e-beam exposure, the carbon film started to evaporate at a slower rate than QDs, giving rise to the formation of a quasi-circular hole after 60 s. As room temperature is 298 K and the melting point of carbon film is 3400 K,[164] for this highly focused e-beam conditions and high current density, this would correspond to a local temperature increase of ~3100 K. For *in situ* observations shown in Figure 4.9, the e-beam radius is 30 nm (current density of 30 A/cm^2), which is about one seventeenth of the previous observation. Hence, it is estimated that the local temperature increases by 180 K, from 298 K to 478 K. Such an increase of the local temperature is close to the one reported for nanocrystalline α-titanium,[166-167] which showed the decrease of dislocation density. During the low-temperature (523 K) heat treatment in α-titanium, the activated dislocations can be repaired through the annihilation of dislocations with opposite signs or their removal at the grain boundaries. The hardness and corrosion resistance of nanocrystalline α-titanium is enhanced after low-temperature annealing. Our results demonstrate that post-treatment techniques based on e-beam exposure can

remove some structural defects in hetero-QDs. As previously mentioned, (Figure 4.7a), the unit cell of tetragonal CuInSeS can be associated with two quasi-ZB unit cells. The structure of CISeS/CdSeS/CdS g-QDs is also found to be similar to other ZB core-shell QDs. Although the kinetics of the restoring process may depend on the material composition, we infer that the e-beam treatments we implemented on CISeS/CdSeS/CdS would also be able to repair defects in systems of comparable atom density and lattice structure, such as ZB CdSe/CdS[150] and CdSe/ZnS[168]. These electron treatments could be performed using a large variety of electron guns[169] or plasma-immersion ion implantation[170] systems. The e-beam post-treatment techniques also can be applied for *in situ* remediations of nanoscale devices.

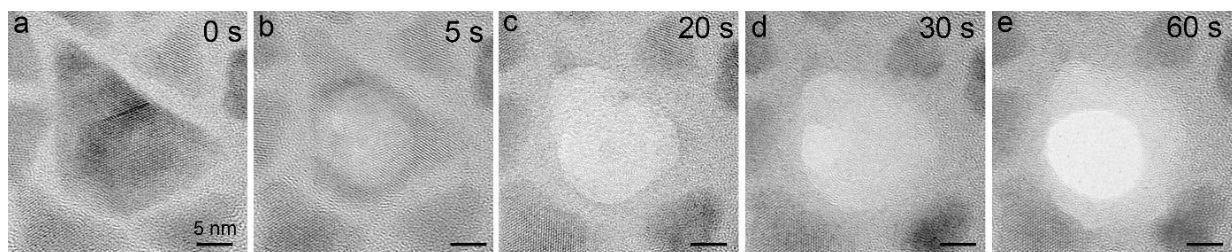

Figure 4.10 Evaporation of hetero-QDs and carbon film under e-beam exposure. (a) hetero-QDs before strong e-beam irradiation, (b)-(e) hetero-QDs after 5s(b), 20s(c), 30s(d) and 60s(e) e-beam irradiation. The radius of e-beam for irradiation is ~7 nm.

4.6 Summary

In summary, CISeS/CdSeS/CdS hetero-QDs were synthesized through a facile two-step method. HRTEM observation from different zone axes shows that the as-synthesized hetero-QDs have a regular tetrahedron shape with $\{111\}$ crystal facets. Extensive HRTEM analysis of QDs at different growth stages revealed that the cubic CdS growth on tetragonal CISeS/CdSeS layer by layer and the epitaxial relationship between core

and shell is determined to be $[110]_{\mathrm{core}}//[110]_{\mathrm{shell}}$, $\{112\}_{\mathrm{core}}//\{111\}_{\mathrm{shell}}$. In addition, we also proved that the screw dislocation in the hetero-QDs can be repaired using e-beam exposure post-growth treatments. The investigation of the growth mechanism and epitaxial relationship can be used to achieve hetero-QDs with high-quality interfaces, especially for hetero-QDs with different crystal structures in the core and shell. The low-temperature e-beam post-growth treatment whose efficiency for repairing SF has been demonstrated in this work defines new strategies and new routes for synthesizing defect-free hetero-QDs.

5 ENHANCED RADIATION RESISTANCE OF PHOTOLUMINESCENCE EMISSION INDUCED BY NANOCLUSTERING

5.1 Motivation

The vulnerability of Erbium and Ytterbium doped optical devices under radiation-prone environments is an ongoing research topic for space technologies. Such devices are essential to many optical sources, gyroscopes, all fibered communication links, and laser sources used in satellite or space station.[171-173] However, cosmic radiations found in the space environment are known to damage (Er, Yb)-doped fibers[174], leading to irreversible optical losses. Such a degradation of the Er-doped fiber amplifiers (EDFAs) properties is mainly resulting from the radiation-induced non-radiative trapping defects and color centers. It is shown that H_2 loading of hermetically coated EDFAs can improve their lifetime in a radiation-prone environment.[175] However, the formation of hydroxyl groups (OH) and hydrides (SiH) generates strong absorption peaks in the near-infrared (NIR) spectral range, responsible for significant optical losses. Other approaches based on the development of fibered amplifiers with shorter lengths and Ce-doping were also implemented, yet these systems do not meet the requirements for satellites because they are based on the use of intense optical pumping sources which is too energy-intensive for space applications.[176]

In this chapter, the influence of Er and Si nanoclustering on NIR Er emission is investigated in fused silica samples exposed to proton beams, which is used to reproduce the space radiation conditions at LEO. Bulk silica glasses are used as model systems that mimic optical fibers. The growth of Er/Si nanoclusters, synthesized in co-implanted fused silica through thermal annealing between 1000°C and 1200°C, was analyzed by in-

depth TEM and EDS analysis. PL measurements of Er^{3+} optical emission indicate that its $_4I^{13/2} \rightarrow {}_4I^{15/2}$ transition around 1.54 μm can still be used for optical communication after proton irradiation doses equivalent to over 50 years of exposure at LEO. The enhanced radiation resistance of PL emission can be explained by the increase of photocarriers transfer occurring between Si NCs and NIR Er emitting levels, which partially compensates for the optical losses induced by structural damage. This work demonstrates an alternative approach for the development of advanced Er light sources with superior radiation resistance and longer operating times in space environments. Some of the work described in this chapter has been previously published in Material & Design, 89, 715-720, 2017.

5.2 Distribution of Si and Er in SiO_2 layer

Table 5.1 summarizes the data obtained from TRIM-SRIM calculations for Si^+ and Er^+ ions implanted with acceleration voltages between 50 and 200 kV, into a SiO_2 substrate of 2.30 g/cm^3 mass density. The projected range (R_p) and straggle (ΔR_p) of impinging are given in the third and the fourth columns, respectively. These values are found to increase with the implantation energy. For silicon ions accelerated at 200 kV, the projected range and straggle are almost four times than that of 50 keV Si^+. Under the same accelerating voltage, Er ions have smaller projected ranges and straggles compared to Si, due to the their larger atomic mass. It is similar to the discussions about different types of charged particles (in section 1.1), which show the light ions trend to have better penetrability.

Table 5.1 Projected range and straggle of Si and Er ions into SiO_2 substrate

Ion	Energy Level keV	projected range R_p(nm)	Straggle ΔR_p (nm)
Si	50	69.3	24.5
	100	138.3	42.4
	150	208.9	57.8
	200	281.3	71.6
Er	50	28.2	6.0
	100	44.4	8.8
	150	59.2	11.1
	200	73.3	13.3

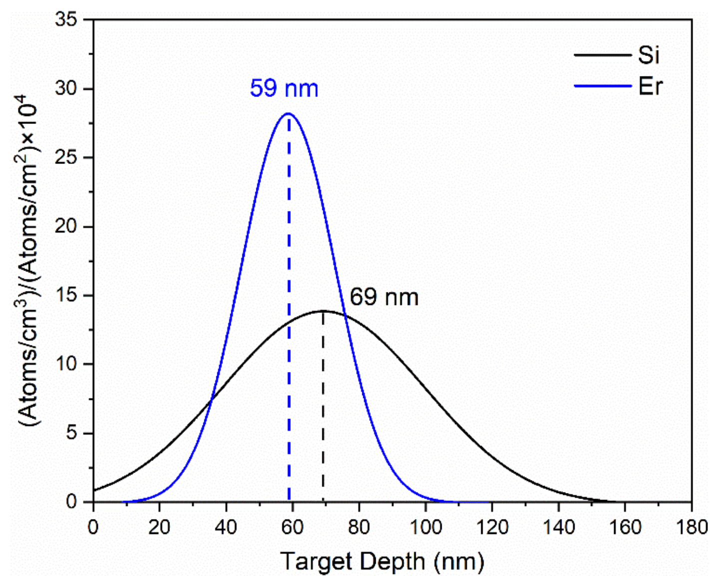

Figure 5.1 The implantation depth-profiles of 50 keV Si and 150 keV Er ions in SiO_2 substrate calculated by SRIM.

In our experiments, 50 keV Si ions were implanted into a SiO_2 layer, followed by the implantation of 150 keV Er ions. According to table 5.1, the projected ranges of Si and Er are 69 nm and 59 nm, which are quite close values. The detailed implantation depth-profiles calculated by SRIM are shown in Figure 5.1, showing an effective overlap of the depth-profiles calculated for the implanted Si and Er. As a consequence, it is expected that for thermal annealing conducted after implantation, some NPs can mix implanted Si and Er during their formation, within a sample region located between 20 and 120 nm from the surface. Such a feature is critically important in our following experiments because it will promote the photocarriers transfer between Si and Er NPs.

5.3 Morphological and microstructural investigations

5.3.1 Morphology of the NPs after annealing

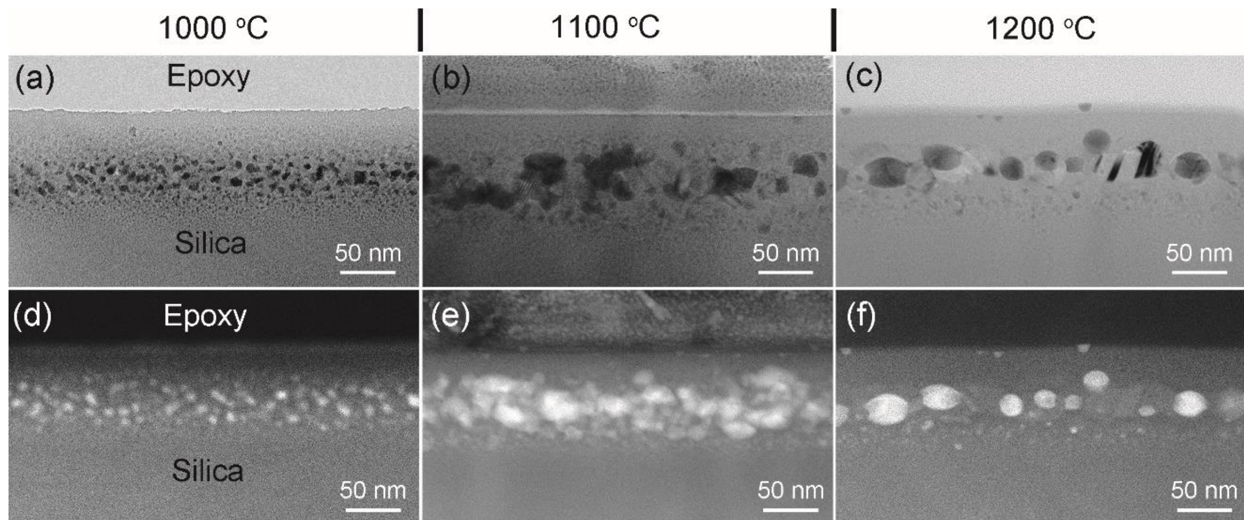

Figure 5.2 **BF TEM images of samples annealed at 1000°C (a), 1100°C (b) and 1200°C (c); with their corresponding HAADF TEM images (d), (e) and (f).**

Typical BF TEM images are presented in Figures 5.2(a)-(c), and HAADF images in Figures 5.2(d)-(f), for samples annealed at 1000°C, 1100°C, and 1200°C, respectively. For comparison purposes, all cross-sectional images were recorded at the same magnification. In each sample, Si and Er-based nanoclusters were observed in the upper region of the implanted SiO_2 film up to a depth of 120 ± 10 nm,[177] which is consistent with the depth-profiles calculated by SRIM (Figure 5.1).

HAADF analysis (also known as Z-contrast imaging) was carried out, to measure the distribution of Si and Er after annealing and show their effective overlap. The thickness of the cross-sectional samples (t) was measured by electron energy loss spectroscopy using the Log-Ratio method,[178] according to:

$$t/\lambda = \ln\left(I_t/I_0\right) \qquad \text{Eq. (5.1)}$$

where λ is the total mean free path for inelastic electron scattering, and I_t/I_o is the relative variation of the integrated spectral intensity with respect to the zero-loss peak. The thickness is ~ 40 nm in each sample so that the TEM image contrast of all nanoclusters is proportional to the concentration of Er. Only incoherently scattered electrons at high angles were collected so that the acquired images can be interpreted as a result of atomic number differences inside the sample.[129] Hence, Er NPs will be brighter than Si NPs in the HAADF image, due to their larger atomic number. In Figures. 5.2(d)-(f), these bright NPs can be associated with clusters containing an elevated concentration of Er. The brightness of Si NPs is quite close to that of the surrounding SiO_2, since the contrast both mainly arise from silicon. HAADF images show the as-synthesized Er and Si NPs are well mixed, which will benefit the carriers' transfer between them.

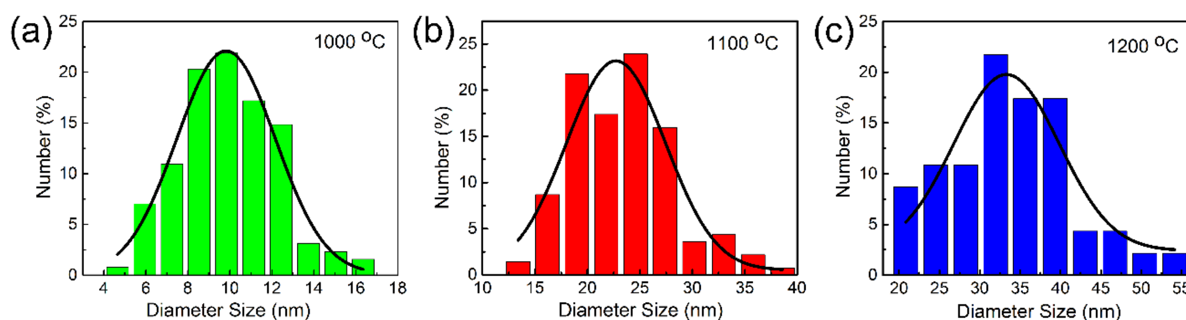

Figure 5.3 Nanoparticle size-distribution of samples annealed at 1000°C (a), 1100°C (b), and 1200°C (c).

In addition, HAADF images indicate that Er atoms form larger aggregates about 33 nm in diameter at higher annealing temperatures. At 1000 °C, the depth distribution of small and isolated clusters suggests that only a small fraction of Er contributes to the formation of NPs. The diffusion coefficients of Er and Si both increase linearly with the annealing temperature, which is 5×10^{-16} cm^2/s[179] and 10^{-17} cm^2/s[180] at 1100 °C, respectively. Therefore, the Er participates in the growth of NPs more efficiently and the size of NPs increases in the sample annealed at 1100 °C due to the higher diffusion rate. In the sample annealed at 1200 °C, the observed NPs were found to contain a higher concentration of Er and no other small Er NPs can be observed in the surrounding SiO_2. The size of NPs further increases not only through the Ostwald ripening mechanism but also thanks to the coalescence of small NPs, [53, 60] described in section 1.3.3. The average dimensions of these NPs were determined from an in-depth analysis of TEM images, accounting for more than 100 observed nanoclusters. As shown in Figure 5.3, the diameter of the formed nanoclusters increases continuously with annealing temperature, from 9.9 nm at 1000°C, to 25.0 at 1100°C, and up to 33.0 nm at 1200°C.

5.3.2 Microstructure and composition of the NPs after annealing

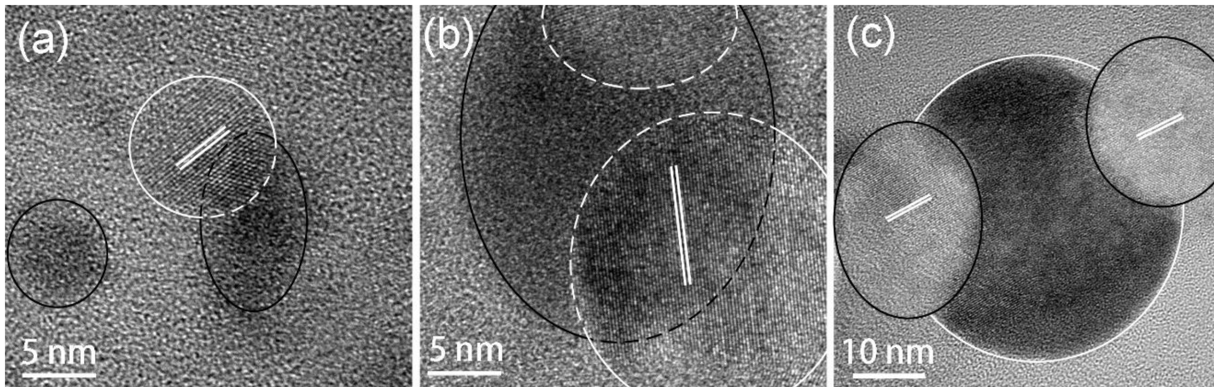

Figure 5.4 **HRTEM images of samples annealed at 1000°C (a), 1100°C (b) and 1200°C (c), obtained at magnifications of ×600 000, ×600 000 and ×400 000, respectively.**

The microstructure of the formed NPs was investigated by HRTEM. Two kinds of NPs were observed in the samples annealed at 1000 °C (Figure 5.4a), 1100 °C (Figure 5.4b), and 1200 °C (Figure 5.4c), namely: amorphous NPs and atom-ordered nanocrystallites, identified by black and white circles, respectively. The inter-planar spacing (marked by a pair of parallel white lines) was measured to be 0.313 nm, which corresponds to the {111} d-spacing of bulk Si.

Consequently, the white encircled NPs are identified as pure Si NCs. As for the dark amorphous NPs, they were recognized as nanoclusters containing Erbium, which has a higher atomic number than Si. Since the standard molar enthalpy of Er_2O_3 formation (~ -1900 kJ/mol) is considerably lower than that of SiO_2 (~ -900 kJ/mol) and that of Erbium silicides (~ -60 kJ/mol) [181], the formation of Er_2O_3 is more favorable in the co-implanted Si/Er SiO_2 system. According to the Er-Si phase diagram,[182] Er silicide precipitates can form at ~ 1210 ^{o}C. Hence, the formation of Er-O chemical bonds is strongly promoted in samples annealed at 1000 ^{o}C and 1100 ^{o}C, and the dark Erbium amorphous nanoclusters

observed in Figure 5.4 are most likely oxidized. Such oxidation can occur to the detriment of the Si-bond restoration inside the SiO_2 layer, where a number of broken chemical bonds have been generated during the successive implantation of Si and Er ions.[177]

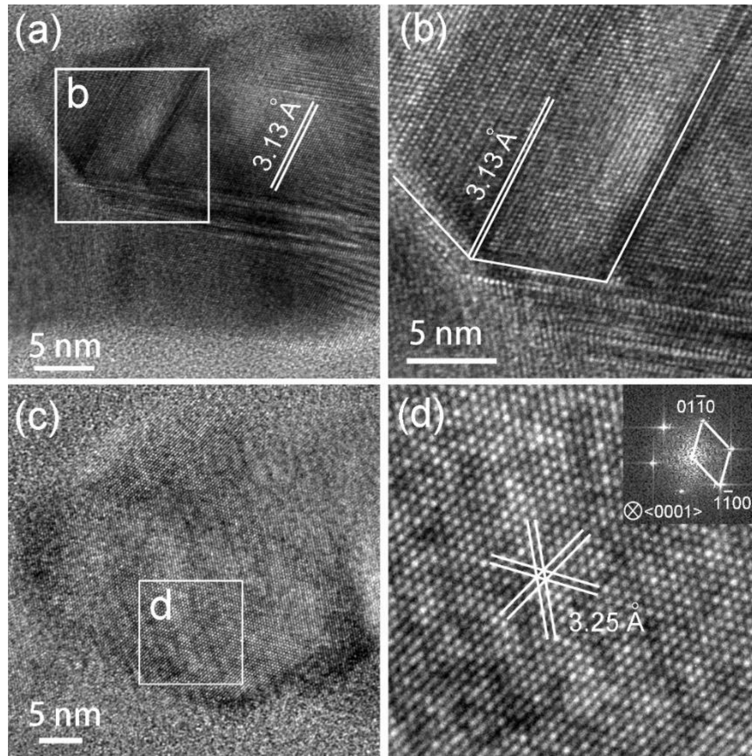

Figure 5.5 **(a) and (c) HRTEM images of samples annealed at 1200 °C; (b) and (d) zoomed images at a magnification of x 500 000, corresponding to rectangular regions of images (a) and (c), respectively.**

In Figures. 5.5 (a)-(b), HRTEM images reveal the presence of SFs and TB inside large Si-ncs synthesized at 1200°C. This structural defect may result from the coalescence of small Si-ncs into larger ones [53, 183]. In addition, a new chemical phase (only observed at 1200 °C) was found for the NP shown in Figures. 5.5(c)-(d). The inter-planar distance of its atomic structure is 0.325 nm, which corresponds to the $\{1\bar{1}00\}$ inter-planar distance of hexagonal $ErSi_2$.[184] Statistical analysis shows that there are approximately five times

more Er_2O_3 NPs than $ErSi_2$ NPs. This demonstrates, in addition to the nucleation of pure Si NCs, the possible formation of erbium silicide NCs above 1100 ^oC.

5.3.3 Chemical composition analysis by EDS line scans

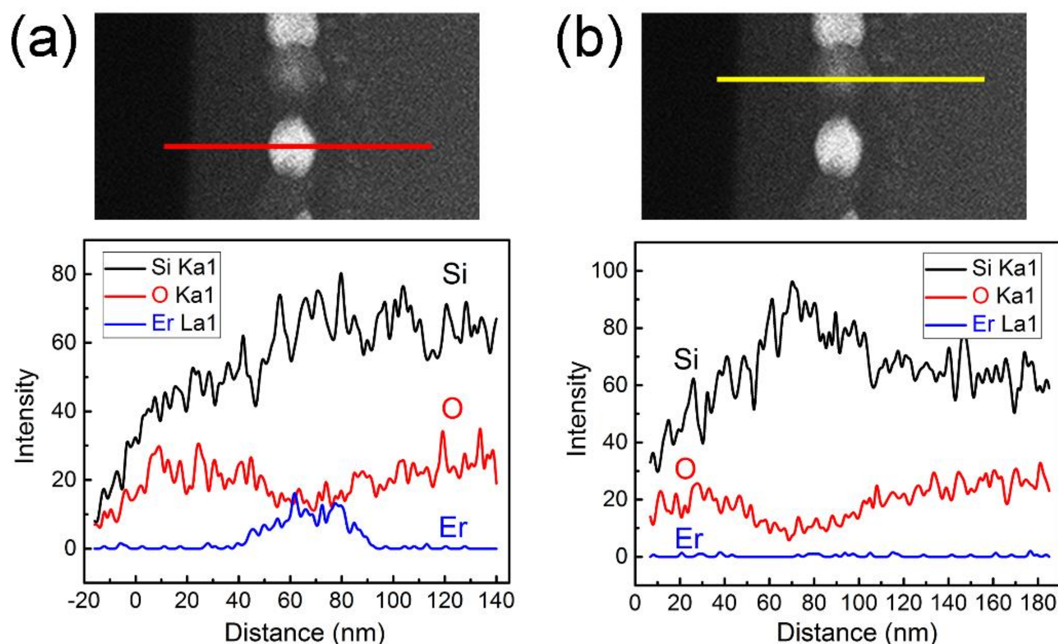

Figure 5.6 **EDS line-scan of bright (a) and dark (b) NPs synthesized at 1200°C, showing the neighboring formation of Er-rich Si-nc (a) and pure Si-nc (b).**

EDS line scans were carried out through two different NPs synthesized at 1200 ^oC. All the NPs are embedded in the SiO_2 matrix, there will be strong Si and O background single in the EDS line scan. According to the TEM analyses in section 3.3.2, the chemical composition will be various for the NPs with different brightness. Er signal should be detected in the bright NPs and the concentration of O should be low in the region with NPs. An example of an EDS line scan (Figure 5.6a) shows that while the concentration of Si remains unchanged inside this bright NP, the concentrations of Er and O increase and decrease, respectively. Such features are consistent with the EDS signature of an

Er-rich Si-nc, where the detected oxygen atoms mainly originate from the fused silica surroundings. On the other hand, the EDS measurements showed in Figure 5.6(b) are compatible with a line scan of one Si-nc embedded within SiO_2, free of Er, where the intensity peak signals of Si and O increase and decrease, correspondingly. Such EDS elemental line-scan profiles agree with our expectation based on the TEM analyses, which show the NPs with different contrast have various chemical compositions.

5.4 SRIM simulations for proton irradiation

As mentioned in section 1.1.2, the natural background radiation in space is mainly composed (~90%) of electrons, protons, and ions originating from SCR, GCR, and the Van Allen belts. Typical radiation doses associated with the proton flux at GEO or LEO within space modules are between 80 and 120 mGy (0.8–1.2 mrad) per year.[13] To simulate space conditions in our implantation chamber, the irradiation dose, D (in mGy) is calculated by the following equation:

$$D = 1.602 \times 10^{-10} \Phi \frac{dE}{dx}, \quad \text{Eq. (5.2)}$$ [185]

where, Φ (in H^+/cm^2) is proton fluence and $\frac{dE}{dx}$ is the mass stopping power. For 10 keV proton implanted into a fuse silica target with a density of 2.30 g/cm^3, the mass stopping power is ~ 0.28. The electronic stopping power and nuclear stopping power of protons with different energy are shown in Table 5.2. It also indicates that the electronic stopping power increased firstly and then decreased with the energy, which has a maximum value at around 100 keV. The impinging protons penetrate the implanted materials and lose their energy through elastic collisions with the target atom nuclei and interactions with the electron gas. Therefore, the crystal order can be disrupted by energetic ions, leading to

the formation of both cation and anion Frenkel pairs which can accumulate inside the crystal lattice as radiation-induced point defects.[108] After longer exposures, radiation-induced amorphization may occur.[186]

Table 5.2 Electronic stopping power, nuclear stopping power, projected range, and straggle of proton implanted in SiO_2.

Energy Level keV	dE/dx Elec. MeV/(mg/cm^2)	dE/dx Nucl. MeV/(mg/cm^2)	projected range R_p(nm)	Straggle ΔR_p (nm)
5	0.203	7.21×10^{-3}	82.8	41.6
10	0.279	4.85×10^{-3}	151.5	55.9
50	0.532	1.60×10^{-3}	519.9	86.5
100	0.548	0.94×10^{-3}	903.0	101.2
150	0.502	0.68×10^{-3}	1 310	113.4
200	0.451	0.54×10^{-3}	1 760	126.9
500	0.283	0.25×10^{-3}	5 510	267.8
1 000	0.190	0.14×10^{-3}	15 100	695.7
5 000	0.064	3.44×10^{-5}	199 410	8 600
10 000	0.037	1.857×10^{-5}	662 020	30 090

Figure 5.7 shows the depth profile of H^+ implanted at 10 keV calculated by SRIM simulations. Compared with the depth profile in Figure 5.1, the projected ranges of Si and Er in our experiments are both much smaller than the one calculated for 10 keV H^+ (around 150 nm). BF and HADDF images in Figure 5.2 also prove that Si and Er-based nanoclusters are distributed in the upper region of the implanted SiO_2 film up to a depth around 120 nm. Therefore, during the proton irradiation process, most of the proton will pass through the NPs layer whose center is located at about 70 nm to the surface. Typically, the energy of high-speed ions from space radiation can reach several hundreds

of MeV, which can penetrate through the shell of the satellite easily. In our experiments, the samples are exposed to the proton beam without any protection. The relationships between stopping power and ion energy have been shown in Table 5.2. Therefore, we can generate similar damage inside the target materials using low-energy protons by adjusting the implantation doses accordingly.

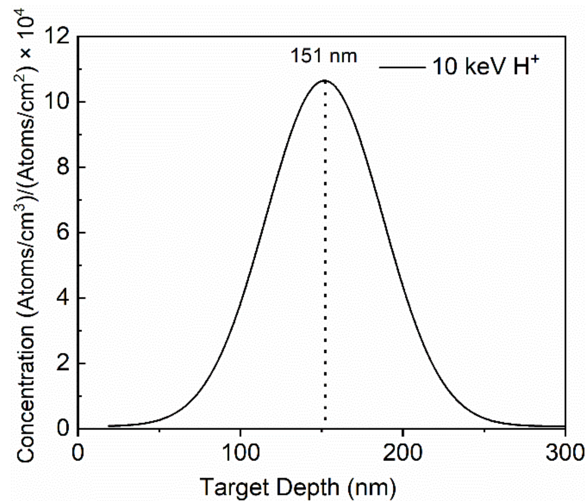

Figure 5.7 **Implantation depth profile of 10 keV H^+ is calculated by SRIM-TRIM simulations. The target material is SiO_2 with a density of 2.30 g/cm^3.**

In order to study the damaging rate generated by impinging protons, we built a simple mixed layer (Si, Er, and O) of 200 nm thickness. The rate of damage generated by impinging protons depends on their energy, tilt angle, as well as density, and the nature of the target. The vacancy distribution generated by H^+ irradiation were calculated in the layer containing a mixture of implanted Si and Er and shown in Figure 5.8. The solid lines in green, blue, and red refer to the vacancies of Si, Er, and O, respectively. Figure 5.8 (a) shows the results obtained for a target material containing the same contents of Si, O, and Er are the same. It shows that 10 keV H^+ irradiation can generate more Si vacancies than Er and O in the mixed layer. The number of Er and O vacancies is very close. In our

sample, the ion dose of Si and Er is 2.0×10^{17} ions/cm^2 and 5.0×10^{15} ions/cm^2, respectively. If multiply the ion density shown in the implantation depth-profiles (Figure 5.1), we will get the atomic density of 2.6×10^{22} Si/cm^3 and 1.3×10^{21} Si/cm^3. In SiO_2 substrate (density of 2.30 g/cm^3), the atomic density of Si and O is about 2.3×10^{22} Si/cm^3 and 4.6×10^{22} O/cm^3, respectively. Therefore, in the sample we have studied, the atomic ratio between Er, Si, and O is around 1:20:20. The corresponding vacancy distribution in such mixed layer under H^+ irradiation is shown in Figure 5.8(b). Here, the number of Er vacancies is very low due to its low concentration and small nuclear stopping power. These SRIM calculations indicate that the impacts of proton irradiations on different types of NPs may strongly vary. More damage will be created inside Si NPs than that of Er NPs. Therefore, the effect of H^+ implantation on their properties (for example, their PL emission) should have different impacts and dynamics upon the implantation dose.

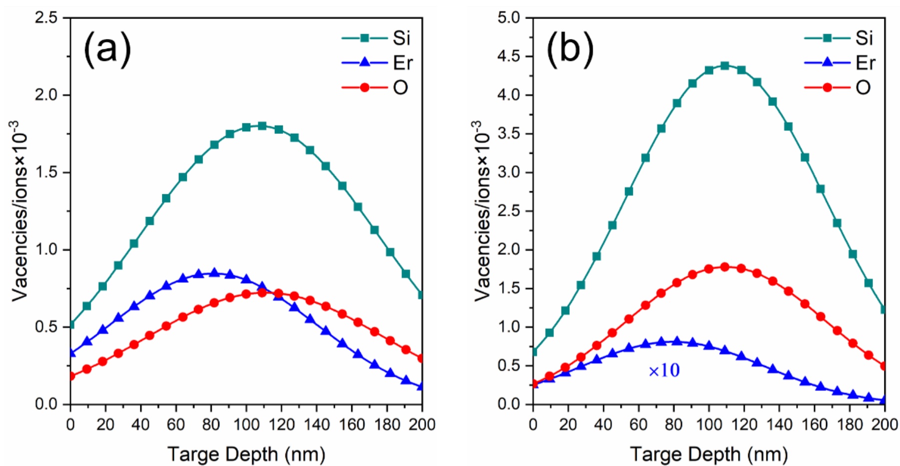

Figure 5.8 **Vacancy distribution inside Si, Er and O mixed layer exposed to 10 keV H^+ irradiations, which is calculated by SRIM simulations inside a target where the concentration of Si, O, and Er is the same (a), and the atomic ratio between Er, Si and O is 1:20:20 (b).**

5.5 Photoluminescence measurements

5.5.1 PL intensity after annealing

The PL spectra of Er and Si/Er implanted samples annealed at 1000, 1100, and 1200 ^{o}C are shown in Figure 5.9. No signal was detected in materials implanted exclusively with Er and annealed at 1100 ^{o}C and 1200 ^{o}C (not shown). The NIR (Figure 5.8a) and VIS (Figure 5.9b) emissions are associated with the Er^{3+}-4f: $^{4}I_{13/2}\rightarrow ^{4}I_{15/2}$ optical transition and the Si-nc PL, respectively.[177]

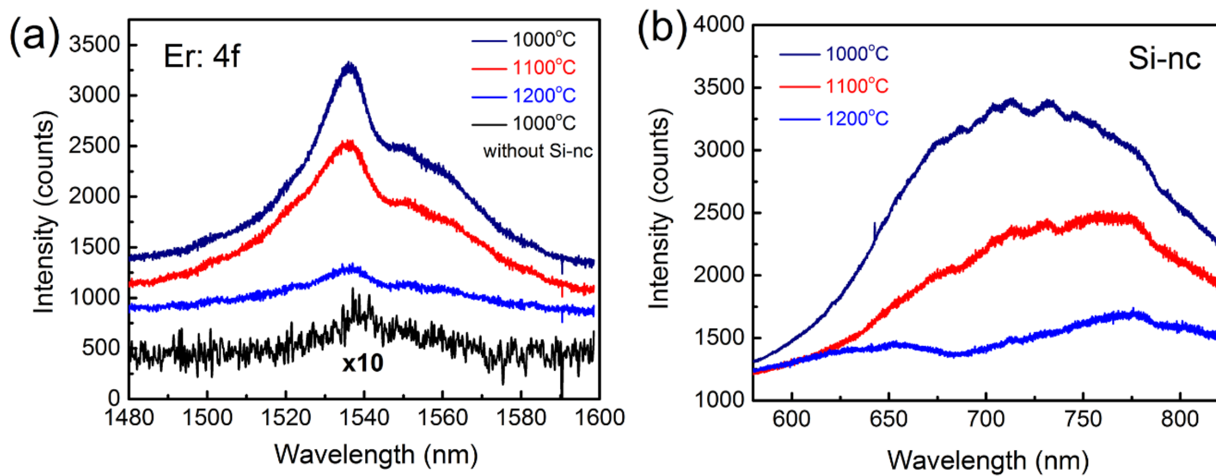

Figure 5.9 PL spectra of the NIR Er emission (a) and the VIS Si emission (b).

In agreement with other studies on Si/Er hybrid systems [187-189], the presence of Si-ncs was found to improve the Er PL-emission by around 1.54 µm. By comparing the NIR (Figure 5.9a) and VIS (Figure 5.9b) signals, a maximum Er PL emission may be observed when the Si-nc PL-emission is the highest. This feature results from the occurrence of an effective transfer mechanism between the photocarriers generated by laser excitation in Si-ncs towards the NIR emitting levels of Er[190]. The schematic diagram related to the transfer mechanisms of the photocarriers between Si and Er NPs is shown in Figure 5.10.

Under 405 nm laser, electrons can be excited from the valence band to the conduction band. When the excited electrons return to the ground state, this process will be accompanied by Si and Er^{3+}-4f: $^4I_{13/2} \rightarrow {}^4I_{15/2}$ photon emission. For Er^{3+} NIR PL emission, besides electrons excited to the conduction band, the photocarriers transfer from Si to Er also contribute to the final PL emission.

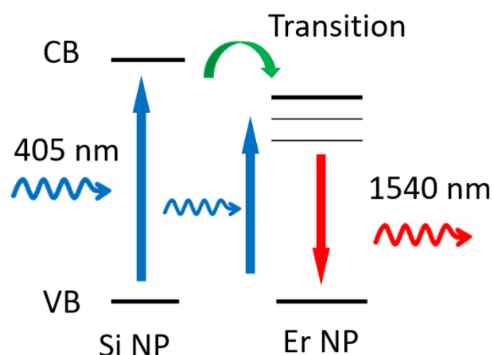

Figure 5.10 Schematic diagram for photodynamics between Si and Er NP.

Figure 5.9 also demonstrates that the intensity of all recorded PL signals decreases as the annealing temperature increases. The drastic reduction of the PL peaks reported in the sample annealed at 1200 °C (Figure 5.9a) has two origins: the formation of non-luminescent $ErSi_2$ (whose synthesis was evidenced in Figures. 5.5c-d) and the formation of large silicon nanoaggregates (in Figures. 5.5a-b). The latter observation is also consistent with the redshift of the PL peaks observed in Figure 5.9b, which indicates the nucleation of large Si-ncs at higher synthesis temperatures. These clusters are made of several nanocrystallites with different atom orientations. The presence of multiple structural defects within the clusters induces strong optical absorption and/or non-radiative transitions.

5.5.2 Degradation of PL intensity after proton irradiation

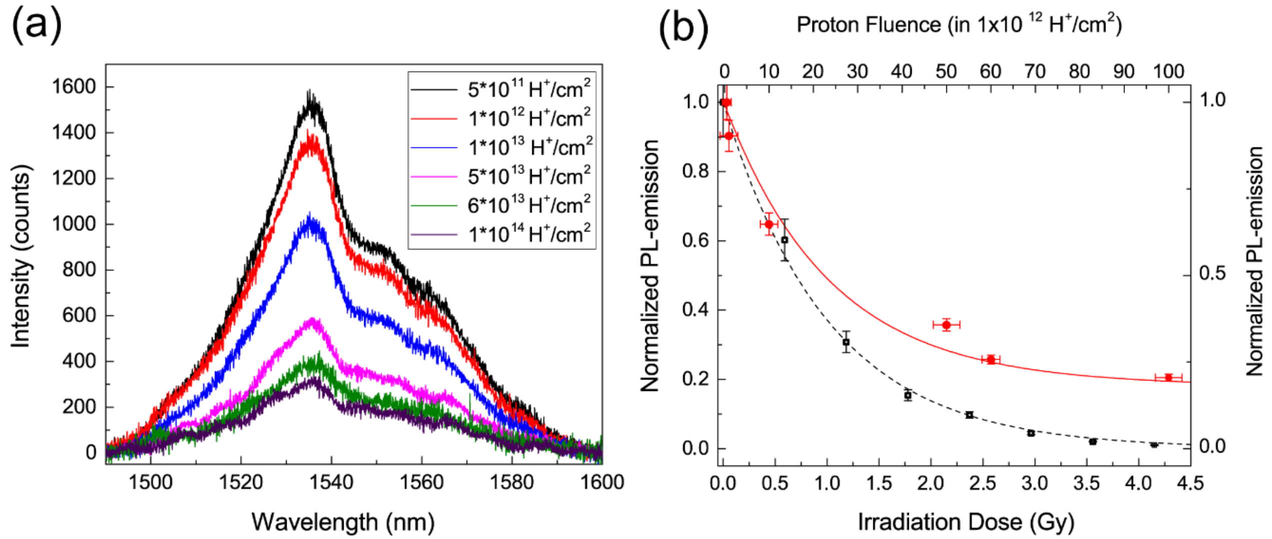

Figure 5.11 **Evolution of the NIR PL spectral emission of Er/Si hybrid systems synthesized at 1100°C under proton irradiation (a), with the dose-dependence of their corresponding integrated signal (red solid circles) and the decay of PL power expected in single systems (black open squares) (b).**

Irradiation experiments were conducted on Si/Er co-implanted samples annealed at 1100 °C. The corresponding NIR PL spectra upon proton fluence are shown in Figure 5.11(a). A proton bombardment at a fluence of 1×10^{12} H^+/cm^2 was also conducted on the sample annealed at 1000 °C, which contains only Er-nps. After irradiation, the weak PL-signal reported for this sample at the bottom of Figure 5.9a becomes undetectable (not shown). For samples prepared at 1100 °C, a continuous decrease of the 1.54 µm peak is reported as a function of the irradiation dose. According to Eq. (5.2) and the annual radiation dose measured inside space modules (see section 5.4 and ref. 13), proton fluences of 5×10^{11}, 1×10^{12}, 5×10^{12}, 1×10^{13}, 5×10^{13}, 6×10^{13}, 1×10^{14} H^+/cm^2 correspond to irradiation conditions at GEO/LEO during ~100 days, 200 days, 3 years, 5 years, 27 years, 32 years

and 55 years, respectively[13, 191]. In Figure 5.11(b), the normalized spectral intensity of each measured PL peak, integrated between 1480 and 1600 nm after subtracting the optical background contribution (red solid dots), is reported as a function of proton irradiation. Since the average penetration depth of 10 keV protons into SiO_2 is around 150 nm [9], most of the impinging protons have entirely crossed the layer where Si-nc and Er-np have grown (the thickness measured for the implanted sublayer is around 100 nm in Figure 5.2).

Hence, the reported decrease in PL emission can be directly related to the damage generated by impinging protons, responsible for the formation of color centers that generate optical absorptions [192-193]. Typically, for Er light emission, the effect of ion bombardment or radiation exposure on PL signals should result in a single exponential decay function decreasing down to zero [194]. As evidenced in Figure 5.11b, the variation in the measured PL intensities (red solid dots) does not follow this relationship. Instead, a fast reduction of the PL emission for low irradiation doses ($D < 100$ mGy) up to half the value of the non-irradiated erbium emission is observed, followed by a weak quasi-linear and continuous decrease.

The expected changes in PL intensity can be estimated on the basis of the data collected for the VIS PL signals of Si-ncs exposed to an 18 kV proton beam [194]. This extrapolation was performed with a mass stopping power dE/dx = 0.37 MeV/(mg/cm^2), calculated for protons accelerated at 18 kV (instead of 0.28 MeV/(mg/cm^2) for 10 keV protons in this work) [194], using TRIM simulations [9]. The resulting curve (marked by black squares) indicates that ~ 90 % of the PL signal should be lost after 2.5 Gy, while more than ~ 30%

of the nominal Er emission is still detected (red circles). This shows that the PL-emission of erbium survives to radiation effects for longer times in Er-np/Si-nc systems.

5.5.3 Absorbance spectra before and after proton irradiation

Figure 5.12 shows that the changes in optical absorption due to the presence of Si-ncs are more important than those induced by proton bombardment effects. An increase by one order of magnitude is reported for the absorbance measured around 405 nm in Si-nc-based samples, with respect to the absorbance measured in pure fused silica. This suggests that the presence of Si-ncs can significantly improve the efficiency of the laser optical pumping. In fused silica samples free of Si-nc, while the increase in optical absorption at the laser excitation wavelength is marginal after irradiation (less than 10 %, inset of Figure 5.12), such an increase is greater than 50 % in the NIR spectra range (2nd inset on Figure 5.12). Such a feature means that even if the laser pumping efficiency increases after proton irradiation due to the possible creation of non-bridging oxygen hole centers (NBOHC) or other oxygen defects by impinging protons [195], this improvement in photocarrier generation is lower than the increase of optical losses in the NIR spectral range. Hence, in the absence of Si-ncs, the Er PL-signal around 1.54 μm should decrease upon proton irradiation, as observed for Er-nps synthesized at 1000 ^{o}C in pure fused silica (Figure 5.9a). In samples where Si-nc have been produced, the greater impact of proton damaging effects on optical absorbance variations reported in Figure 5.12 (green and blue lines) may result from a local increase of the stopping power in the Si-nc sublayer of greater mass density. For these materials, although the optical losses due to proton bombardment increase around 1.54 μm, the optical absorbance is still lower in the NIR range than in the UV-VIS range.

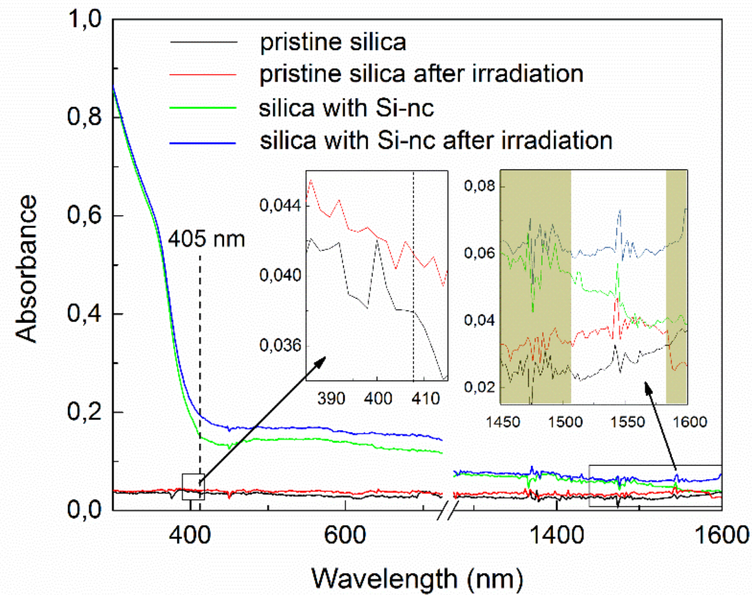

Figure 5.12 **Absorbance spectra measured before and after proton irradiation in pristine fused silica and fused silica where Si-ncs have been produced by 50 keV Si^+ implanted at a fluence of 2.10^{17} Si^+/cm^2. The insets show the variations of absorbance around the laser wavelength excitation (405 nm) and around 1.54 µm (between 1510 and 1580 nm).**

5.6 Phenomenological analysis about the enhanced PL emission

5.6.1 Degradation of PL under proton irradiation

Assuming that the number of emitting centers decreases according to a geometric sequence under constant particle flux bombardment, the PL-signal decay should follow a simple exponential decay function upon irradiation. Such a trend is also observed for the degradation of optical properties in many systems exposed to damaging radiations[196-198]. In the studies of GaN LED,[198] the normalized light output decreases as the fluence increases due to the irradiation introduces defects that may act as nonradiative recombination centers. The model described and discussed below brings a new mathematical understanding to the data trend observed in Figure 5.11b, to show that the

PL intensity measured in Er-np/Si-nc systems does not follow the trend expected for the progressive destruction of emitting centers upon irradiation [194].

The intensity of the Er^{3+} NIR PL emission in SiO_2, I, can be expressed as:

$$I = \tau_{PL} N_{ph}^{Er} (1 - \alpha), \qquad \text{Eq. (5.3)}$$

where τ_{PL} refers to the erbium PL emission rate around 1.54 μm, N_{ph}^{Er}, to the number of Er^{3+}:*4f* photocarriers, and α to the fraction of PL-power absorbed by the damaged SiO_2 upper layer, which is crossed by every collected NIR photon. After exposure to a proton irradiation dose, *D*, this optical absorption should be proportional to the density of color centers, assuming that the effect of OH on the upper SiO_2 matrix transparency can be neglected for low proton fluences. The concentration of optical absorption centers is correlated with the concentration of recoiled target atoms, resulting from proton-matter interaction, as follows [199]:

$$\alpha = a \, \frac{n_{rec.}}{n} D, \qquad \text{Eq. (5.4)}$$

where a is a dimensionless fitting parameter, related to the formation rate of color centers per recoiled atom and unit irradiation dose, n_{rec} is the density of the target atoms displaced by impinging protons, and n is the target atom density.

Using the SRIM-TRIM simulation[9], at depths between 20 and 80 nm, where most of Si and Er nanoclusters are formed (Figure 5.2b), each incident proton moves on average 1.65 x 10^5 atoms along its path within the SiO_2 target. Since the volume of Erbium nanoclusters represents less than a few percent of the target volume, the damage generated inside Er-nps is negligible with respect to the damage generated by impinging protons into the host matrix. Thus, it can be postulated that the number of photocarriers

generated inside emitting centers (relating to N_{Ph}) and τ_{PL} remains constant during and after proton bombardment so that the Er PL signal given in Eq. (5.3) should follow a single exponential decay function: $I(D) \propto \exp(-D/\Delta_1)$.

The plot (marked by dashed black lines) in Figure 5.11(b), showing the relative PL variations calculated for a ~ 1/3, supports the above-mentioned mathematical trend as an accurate reproduction of the decrease in PL intensity upon proton beam exposure for irradiated Si-ncs [194]. The value of 1/3 is consistent with the fact that 3 target atoms must be displaced to move each SiO_2 molecule, which is a prerequisite to induce a color center. From this coefficient, the calculated decay constant, Δ_1 related to the evolution of the PL signal transmitted through the damaged SiO_2 layer is ~ 1.10 ± 0.05 Gy. Hence, in the absence of any charge or photocarrier transfer mechanism between emitting centers and their surroundings, this value should roughly correspond to the one of pure Er-nps embedded in SiO_2, whose weak PL signals (Figure 5.9a) become undetectable after proton irradiation experiments.

5.6.2 Photocarriers transfer between Si and Er NPs

In Er-np/Si-nc systems, where the amount of Er^{3+}:*4f* photocarriers can be improved by the occurrence of a transfer mechanism between Si-nc and Er-np [190], the number of Er^{3+}:*4f* photocarriers after irradiation, $N_{ph}(D)$, can be expressed as a sum of two contributions:

$$N_{ph}(D) = N_{ph}^{Er} + N_{ph}^{trans}(D) \qquad \text{Eq. (5.5)}$$

where N_{ph}^{Er} is constant over irradiation and related to photocarriers created by optical absorption inside Er-nps, and $N_{ph}^{trans}(D)$ is the number of photocarriers generated in Si-

ncs that are transferred to the NIR emitting levels of Er. Lastly, substituting N_{ph}^{Er} by $N_{ph}(D)$ in Eq. (5.3), the relative variation of the PL signal upon proton beam exposure can be expressed as:

$$\frac{I(D)}{I_0} \propto [1+\beta(D)]e^{-D/\Delta_1}, \quad \text{Eq. (5.6)}$$

where I_0 is the PL intensity before irradiation and β refer to the effective average transfer rate of photocarriers between Si-ncs and Er-nps. By taking: $\beta \propto \exp{(D/\Delta_1')}$, with $\Delta_1{}'$ ~ 1.0 Gy, the resulting curve reported in Figure 5.11(b) (marked in red and superimposed to red solid circles) offers a satisfactory description of the PL-signal evolution observed in irradiated Si-nc/Er-np systems. For these samples, the data obey a two exponential decay fit that can describe the evolution of the PL measurements upon irradiation only under condition $\Delta_1' < \Delta_1$. This suggests that the slower decrease of the Er signal in Er/Si hybrid systems could be explained by a greater amount of transferred photocarriers from Si-ncs toward Er following each proton irradiation. Such a condition is consistent with the promotion of charge transfer mechanisms in damaged SiO_2 [53, 194], where recoiled atoms create new electron states responsible for strong conductivity variations. Hence, due to the presence of Si-ncs, the proton-induced optical losses are compensated by a more efficient optical pumping of the NIR Er emitting centers that makes them more resistant to radiation damage effects.

5.7 Summary

In conclusion, Er/Si nanoclusters synthesized in co-implanted fused silica after thermal annealing between 1000 °C and 1200 °C, have been studied by TEM and EDS analysis. HRTEM images showed that the diameter of the formed nanoclusters increases with

temperature. At 1000 °C and 1100 °C, Si and Er were found to nucleate separately, leading to stronger photoemission signals in both VIS and NIR spectral ranges. At 1200 °C we observed nanoscale aggregates that are less optically active, due to the formation of $ErSi_2$ nanoclusters in localized sample regions. PL measurements of the samples exposed to proton irradiation doses equivalent to those received for more than 50 years at LEO demonstrate that the intensity of the NIR Er emission around 1.54 μm decreases by only ~ 75 % with respect to its nominal emission. This observation is consistent with the fact that in hybrid Er-np/Si-nc systems, the decrease of the Er^{3+}: *4f* PL signal under proton beam do not obey a single exponential decay function upon irradiation dose, as observed for the Si-nc PL emission.

Using a phenomenological model supported by SRIM-TRIM calculations, we showed that the longer longevity of the NIR Er emission in Si-nc/Er-np samples could result from a continuous increase of the photocarrier transfer between Si-nc and Er-np. This mechanism compensates for the optical losses generated in the fused silica matrix and is related to structural damaging effects induced by impinging protons. Overall, the results presented herein suggest new approaches for designing advanced Er-based components with superior performance. The integration of Si-nc inside the silica glass used for the manufacturing of innovative Er-doped NIR light sources is suitable for outer space implementation, notably because both the more intense emission and the improved longevity to cosmic radiation of these systems can double or even triple their operating time.

6 CONCLUSIONS AND PERSPECTIVES

6.1 Conclusions

In this thesis, proton irradiation experiments were conducted on different types of NPs to simulate radiation conditions found in space and investigate their effect on the NPs' functionality. After irradiation, the damage observed in the microstructure of individual NPs has been studied by extensive TEM analyses. Ion stopping powers, straggle, projected range, damaging rates, recoil distribution, and depth profiles of the implanted ions were calculated by SRIM-TRIM simulations. Effects of radiation-induced damage on the physical properties, such as PL emission, PL lifetime, absorption, and charge carrier exchanges were further characterized. In addition, e-beam irradiations on hetero-QDs were performed during several TEM observations. The evolution of structural defects, such as SF and screw dislocation were determined *in situ*.

In chapter 3, structural investigations at the atomic scale are carried out by HRTEM, followed by PL measurements and I-V characterizations, in order to study their evolution upon the irradiation doses. The radiation-induced effects inside g-CS QDs were calculated using SRIM-TRIM simulations, showing that 1.5 and 10 keV proton irradiations create almost the same rate of vacancies inside the CdSe core, while 1.5 keV proton irradiation creates 30% higher vacancies in the CdS shell than that of 10 keV protons. Nanocavities with diameters of about 1.0 nm are reported for g-CS QDs exposed to high proton fluences (10^{17} H^+/cm^2). These TEM micrographs are the first evidence proving that nanocavities in g-CS QDs can be created by proton irradiation. The density of nanocavities is found to be consistent with the calculated rate of vacancies generated during such experiments. Both the PL intensity and lifetime of g-CS QDs decrease linearly

with the concentration of the ion-induced vacancies. The I-V curves of g-CS QDs deposited onto Si wafers, prior to their exposure to 1.5 and 10 keV proton beams, show that the semiconductor bandgap and the charge carrier exchange inside and outside g-CS QDs differ from the I-V response of the substrate. In this work, it is shown that proton irradiation can be implemented to enhance photocurrent generation in g-CS QDs. Such phenomenon is attributed to the generation of additional non-radiative decay channels, as well as efficient photoelectron delocalization. These results will benefit the application of g-CS QDs in optical running and energy conversion.

In chapter 4, three-dimensional (3D) shape and inner structure of CISeS/CdSeS/CdS QDs were studied by in-depth HRTEM characterization. The as-synthesized hetero-QDs have a regular tetrahedron shape with $\{111\}$ crystal facets which were proved by HRTEM observation from different zone axes. An epitaxial growth mechanism for the hetero-QDs is proposed, based on monitoring particle morphology and size at different stages of their growth process. Cubic CdS growth on tetragonal CISeS/CdSeS layer by layer and the epitaxial relationship between CISeS/CdSeS core and CdS shell is determined to be $[110]_{\mathrm{core}}//[110]_{\mathrm{shell}}$, $(112)_{\mathrm{core}}//(111)_{\mathrm{shell}}$. In addition, *in situ* TEM observations demonstrated that structural defects as screw dislocation in hetero-QDs can be repaired by e-beam irradiation. However, there was no significant change in SF in the hetero-QDs, even after 20 min of e-beam exposure. It is because the energy required to repair planar defects of SF is much higher than linear defects of a screw dislocation. Our investigation of the growth mechanism can be used to guide the design for hetero-QDs with high-quality interfaces, especially for hetero-QDs with different crystal structures in core and

shell. The low-temperature e-beam post-growth treatments provide a new strategy to synthesize defect-free hetero-QDs.

In chapter 5, bulk silica glass substrates were used as a model system to mimics optical fibers. Er/Si nanoclusters were synthesized in co-implanted fused silica after thermal annealing between 1000 ^{o}C and 1200 ^{o}C. The diameter of the formed NPs increases with temperature. For samples annealed at 1000 ^{o}C and 1100 ^{o}C, the implanted Si and Er are found to nucleate separately. The influence of Er and Si nanoclustering on NIR Er emission is investigated in fused silica samples exposed to low-energy proton beams which are used to reproduce the space radiation conditions at LEO. A strong NIR and VIS emissions associated with the Er^{3+}-*4f*: $^{4}I_{13/2} \rightarrow ^{4}I_{15/2}$ optical transition and the Si PL can be measured. For the sample annealed at 1200 ^{o}C, the NIR and VIS emissions are very weak, due to the formation of $ErSi_2$. PL measurements of samples exposed to proton irradiation demonstrated that the optical emission of hybrid systems containing Er NPs and Si NCs is more intense and survives longer to proton radiation than the one of unmixed nanoclusterized systems. Such enhanced radiation-resistance of their PL emission results from the increase of photocarrier transfer between Si NCs and Er NPs. This suggests that the integration of Si NCs into NIR Er-based systems can improve their longevity in space, especially for devices used in the satellites that orbit around the Earth within the Van Allen radiation belts. Overall, the results provide new approaches and very promising routes for designing advanced photonic, energy conversion, and other optoelectronic components with superior performance.

6.2 Perspectives

The effects of ion irradiation on freestanding NPs or the NPs embedded in matrix are drastically different from that of bulk or thin-film materials, which is highly dependent on the NPs morphology and surface conditions. Additional work is needed to elucidate the underlying physics leading to numerous changes in the microstructure and properties of NPs. This would be hazardous to employ NPs in radiation environments, such as the devices used in satellites or nuclear power plants, without a deep understanding of the radiation-induced degradation. Especially, when the area of radiation-induced damage approaches the diameter of NPs.

Besides the aforementioned impacts, the microstructure, as well as some physical properties of NPs, can also be manipulated by ion beam exposure using appropriate energies and fluencies. As the results shown in chapter 3 and chapter 4, the photocurrent can be improved after low dose proton irradiation and some defects can be repaired by e-beam exposure. Therefore, it is promising to conduct research on the effects of ion irradiation on other physical properties such as mechanics, magnetism, and heat. In addition, if some properties can be varied regularly with the increasing of fluence, it has the potential to be designed as a radiation sensor which can monitor the radiation fluence.

Further study perspectives are pointing out as following:

(1) Perform ionizing irradiation experiments with heavier ions (such as He^+, N^+, Cu^+, Au^+) at higher acceleration voltages. Although the SRIM calculations can estimate the damage generated by different impinging ions, more experimental data are needed to elucidate the underlying physics.

(2) Develop a new method based on numerical calculations and simulations for describing the damage induced by radiations on the nanomaterials structure and physical properties. In this thesis, SRIM-TRIM simulations have been used to quantify the projected range of the ions that have penetrated into the target and the damaging rates they have generated, including the recoil distribution of target atoms and the depth-profiles of implanted ions inside NPs. One possible improvement of the methodology we have developed in this work would be to account for the shape and the crystal orientation of the target materials, which is not considered by the SRIM-TRIM code, a feature that could be quite important for ordered and/or assembled nanomaterials.

(3) Study the microstructural evolution of NPs under ion irradiation by *in situ* TEM. *In situ* TEM allows researchers to study samples in real-time, under real-world conditions. In this thesis, only CISeS/CdSeS/CdS hetero-QDs were studied by *in situ* TEM, which proves that some defects can be repaired by e-beam post-growth treatments. *In situ* TEM study on NPs irradiated with other energetic ions will benefit the understanding of the evolution of radiation-induced damage on NPs.

(4) Study the effects of ion irradiation on other physical properties. In this thesis, we mainly focused on optical and electrical properties. Other properties, such as mechanical, thermal, or magnetic properties, should be impacted by the radiation-matter interactions presented in our studies. Their deep investigation would be relevant for achieving devices operating in numerous radiative environments.

(5) Design a radiation sensor based on the radiation-induced degradation of the PL emission. According to our proton irradiation experiments described in chapters 3 and 5, the PL emission of NPs decreases with the irradiation dose. Therefore, a radiation sensor

can be designed though monitoring both the intensity and the wavelength of the PL signals.

7 BIBLIOGRAPHY

1. Flores-McLaughlin, J.; Runnells, J.; Gaza, R., Overview of non-ionizing radiation safety operations on the International Space Station. ***J. Space Saf. Eng.**, 4* (2), 61-63, (2017).
2. Attix, F. H.; Tochilin, E., *Sources, fields, measurements, and applications: radiation dosimetry*. Academic Press: New York, 2016; Vol. 3.
3. Luckey, T. D., *Hormesis with ionizing radiation*. CRC press: Cleveland, 2019.
4. Davis, S.; Ross, C.; Mobit, P.; der Zwan Van, L.; Chase, W.; Shortt, K., The response of lif thermoluminescence dosemeters to photon beams in the energy range from 30 kV x rays to 60Co gamma rays. ***Radiat. Prot. Dosim.**, 106* (1), 33-43, (2003).
5. Aharonian, F. A., *Very high energy cosmic gamma radiation: a crucial window on the extreme Universe*. World Scientific: Heidelberg, 2004.
6. Grdanovska, S. Characterization of radiation damage to a novel phontonic crystal sensor. Doctoral dissertation, University of Maryland, 2015.
7. Crespo, M., A review of electrodeposition methods for the preparation of alpha-radiation sources. ***Appl. Radiat. Isotopes**, 70* (1), 210-215, (2012).
8. Zimmermans, D., Relative thermoluminescence effects of alpha-and beta-radiation. ***Radiation Effects**, 14* (1-2), 81-92, (1972).
9. Ziegler, J.; Biersack, J.; Ziegler, M., *SRIM The stopping and range of ions in matter*. Lulu Press: Morrisville, 2008.
10. El-Hakim, S.; Morsy, M., Simultaneous γ (Co^{60})-quanta irradiation and isothermal annealing-induced insulator–metal transition in a-$As_4Se_4Te_2$ chalcogenide composition. ***Radiat. Eff. Defect. S.**, 169* (4), 313-324, (2014).
11. Bütikofer, R.; Flückiger, E.; Desorgher, L.; Moser, M., The extreme solar cosmic ray particle event on 20 January 2005 and its influence on the radiation dose rate at aircraft altitude. ***Sci. Total. Environ.**, 391* (2-3), 177-183, (2008).
12. Blasi, P., The origin of galactic cosmic rays. ***Astron. Astrophys. Rev.**, 21* (1), 70, (2013).
13. Holmes-Siedle, A.; Adams, L., *Handbook of radiation effects*. Oxford University Press: New York, 1993.

14. Radiation belts with satellites. Available from: https://www.nasa.gov/mission_pages/sunearth/news/gallery/20130228-radiationbelts.html.

15. Picano, E., Sustainability of medical imaging. ***Brit. Med. J.**, 328* (7439), 578-580, (2004).

16. Schonfeld, S. J.; Lee, C.; de Gonzalez, A. B., Medical exposure to radiation and thyroid cancer. ***Clin. Oncol-uk.**, 23* (4), 244-250, (2011).

17. Chithrani, D. B.; Jelveh, S.; Jalali, F.; van Prooijen, M.; Allen, C.; Bristow, R. G.; Hill, R. P.; Jaffray, D. A., Gold nanoparticles as radiation sensitizers in cancer therapy. ***Radiat. Res.**, 173* (6), 719-728, (2010).

18. Ismail, M. A. In *Nuclear gauge application in road industry*, IOP Conference Series: Materials Science and Engineering, IOP Publishing: 2017; p 012087.

19. Berejka, A. J., Radiation response of industrial materials: Dose-rate and morphology implications. ***Nucl. Instrum. Methods Phys. Res., Sect. B**, 261* (1-2), 86-89, (2007).

20. Sun, X.; Luo, H.; Dai, S., Ionic liquids-based extraction: a promising strategy for the advanced nuclear fuel cycle. ***Chem. Rev.**, 112* (4), 2100-2128, (2011).

21. Knoll, G. F., *Radiation detection and measurement*. John Wiley & Sons: Hoboken, 2010.

22. Gobet, F.; Eden, S.; Coupier, B.; Tabet, J.; Farizon, B.; Farizon, M.; Gaillard, M.; Carré, M.; Ouaskit, S.; Märk, T., Ionization of water by (20-150)-keV protons: Separation of direct-ionization and electron-capture processes. ***Phys. Rev. A**, 70* (6), 062716, (2004).

23. Berrington, K.; Nakazaki, S., Direct and indirect ionization processes near the Li hollow-atom threshold. ***J. Phys. B: At., Mol. Opt. Phys.**, 31* (2), 313, (1998).

24. Jin, K. Electronic Energy Loss of Heavy Ions and Its Effects in Ceramics. Doctoral dissertation, University of Tennessee, 2015.

25. De Laney, T. F.; Kooy, H. M., *Proton and charged particle radiotherapy*. Lippincott Williams & Wilkins: Massachusetts, 2008.

26. Khan, F. M.; Gibbons, J.; Mihailidis, D.; Alkhatib, H., *Khan's lectures: handbook of the physics of radiation therapy*. Lippincott Williams & Wilkins: Massachusetts, 2012.

27. Turner, J.; Kelsey, C., Atoms, radiation, and radiation protection. New York: McGraw-Hill: 1992.

28. Bakhtiari, M.; Kramer, G.; Takechi, M.; Tamai, H.; Miura, Y.; Kusama, Y.; Kamada, Y., Role of bremsstrahlung radiation in limiting the energy of runaway electrons in tokamaks. ***Phys. Rev. Lett.**, 94* (21), 215003, (2005).

29. Woods, R. J.; Pikaev, A. K., *Applied radiation chemistry: radiation processing*. John Wiley & Sons: Hoboken, 1993.

30. Cember, H.; Johnson, T. E.; Alaei, P., Introduction to health physics. ***Med. Phys.**, 35* (12), 5959, (2008).

31. Williams, J. S.; Poate, J. M., *Ion implantation and beam processing*. Academic Press: New Jersey, 2014.

32. Husnain, G.; Shu-De, Y.; Ahmad, I.; Rafique, H., Structural and magnetic impact of Cr^+ implantation into GaN thin film. ***Solid State Sci.**, 14* (6), 735-738, (2012).

33. He, Z.; Zhao, R.; Chen, X.; Chen, H.; Zhu, Y.; Su, H.; Huang, S.; Xue, J.; Dai, J.; Cheng, S., Defect engineering in single-layer MoS2 using heavy ion irradiation. ***ACS Appl. Mater. Interfaces**, 10* (49), 42524-42533, (2018).

34. Klein, J.; Lorke, M.; Florian, M.; Sigger, F.; Sigl, L.; Rey, S.; Wierzbowski, J.; Cerne, J.; Müller, K.; Mitterreiter, E., Site-selectively generated photon emitters in monolayer MoS_2 via local helium ion irradiation. ***Nat. Commun.**, 10* (1), 1-8, (2019).

35. Ni, Z.; Ishaq, A.; Yan, L.; Gong, J.; Zhu, D., Enhanced electron field emission of carbon nanotubes by Si ion beam irradiation. ***J. Phys. D: Appl. Phys.**, 42* (7), 075408, (2009).

36. Ishaq, A.; Yan, L.; Zhu, D., The electrical conductivity of carbon nanotube sheets by ion beam irradiation. ***Nucl. Instrum. Methods Phys. Res., Sect. B**, 267* (10), 1779-1782, (2009).

37. Ishaq, A.; Ni, Z.; Yan, L.; Gong, J.; Zhu, D., Constructing carbon nanotube junctions by Ar ion beam irradiation. ***Radiat. Phys. Chem.**, 79* (6), 687-691, (2010).

38. Tsuji, H.; Sommani, P.; Kitamura, T.; Hattori, M.; Sato, H.; Gotoh, Y.; Ishikawa, J., Nerve-cell attachment properties of polystyrene and silicone rubber modified by carbon negative-ion implantation. ***Surf. Coat. Technol.**, 201* (19-20), 8123-8126, (2007).

39. Li, S.; Fan, Y.; Chen, H.; Nie, J.; Liang, Y.; Tao, X.; Zhang, J.; Chen, X.; Fu, E.; Wang, Z. L., Manipulating the triboelectric surface charge density of polymers by low-energy helium ion irradiation/implantation. ***Energy Environ. Sci.**, 13* (3), 896-907, (2020).

40. Meisner, L.; Lotkov, A.; Matveeva, V.; Artemieva, L.; Meisner, S.; Matveev, A., Effect of silicon, titanium, and zirconium ion implantation on NiTi biocompatibility. ***Adv. Mater. Sci. Eng.**, 2012*, (2012).

41. Mohamad, N.; Buang, F.; Mat Lazim, A.; Ahmad, N.; Martin, C.; Mohd Amin, M. C. I., Characterization and biocompatibility evaluation of bacterial cellulose-based wound dressing hydrogel: effect of electron beam irradiation doses and concentration of acrylic acid. ***J. Biomed. Mater. Res.**, 105* (8), 2553-2564, (2017).

42. Council, N. R., *Plasma Processing and Processing Science*. The National Academies Press: Washington, DC, 1995; p 45.

43. Conrad, J. R.; Radtke, J. L.; Dodd, R. A.; Worzala, F. J.; Tran, N. C., Plasma source ion-implantation technique for surface modification of materials. ***J. Appl. Phys.**, 62* (11), 4591-4596, (1987).

44. Manova, D.; Gerlach, J. W.; Mändl, S., Thin film deposition using energetic ions. ***Materials**, 3* (8), 4109-4141, (2010).

45. Lin, Z.; Li, S.-J.; Sun, F.; Ba, D.-C.; Li, X.-C., Surface characteristics of a dental implant modified by low energy oxygen ion implantation. ***Surf. Coat. Technol.**, 365*, 208-213, (2019).

46. Svecova, B.; Nekvindova, P.; Mackova, A.; Oswald, J.; Vacik, J.; Grötzschel, R.; Spirkova, J., Er+ medium energy ion implantation into lithium niobate. ***Nucl. Instrum. Methods Phys. Res., Sect. B**, 267* (8-9), 1332-1335, (2009).

47. Hallén, A.; Linnarsson, M. K.; Vines, L. In *Recent advances in the doping of 4H-SiC by channeled ion implantation*, Mater. Sci. Forum, Trans Tech Publ: 2019; pp 375-381.

48. Deicher, M., Radioactive isotopes in solid state physics. ***europhysics news**, 33* (3), 81-85, (2002).

49. Schaffer, M.; Schaffer, B.; Ramasse, Q., Sample preparation for atomic-resolution STEM at low voltages by FIB. ***Ultramicroscopy**, 114*, 62-71, (2012).

50. Dee, C. F.; Ahmad, I.; Long, Y.; Xingtai, Z.; Salleh, M.; Majlis, B., Contact welding study of carbon nanotube with ZnO nanowire. ***Phys. E**, 43* (10), 1857-1862, (2011).

51. Yan, L.; Zhou, G.; Ishaq, A.; Zhou, X., Improving the electrical conductivity of multi-walled carbon nanotube networks by H ion beam irradiation. ***Carbon**, 49* (6), 2141-2144, (2011).

52. Wang, Y. Q.; Smirani, R.; Ross, G. G., Stacking faults in Si nanocrystals. ***Appl. Phys. Lett.**, 86* (22), 221920, (2005).

53. Wang, Y.; Smirani, R.; Ross, G.; Schiettekatte, F., Ordered coalescence of Si nanocrystals in SiO_2. ***Phys. Rev. B**, 71* (16), (2005).

54. Barba, D.; Wang, C.; Nélis, A.; Terwagne, G.; Rosei, F., Blocking germanium diffusion inside silicon dioxide using a co-implanted silicon barrier. ***J. Appl. Phys.**, 123* (16), 161540, (2018).

55. Tsuji, H.; Arai, N.; Gotoh, N.; Minotani, T.; Ishibashi, T.; Okumine, T.; Adachi, K.; Kotaki, H.; Gotoh, Y.; Ishikawa, J., Germanium nanoparticle formation in thin oxide films on Si by negative-ion implantation. ***Surf. Coat. Technol.**, 201* (19-20), 8516-8520, (2007).

56. Popok, V.; Stepanov, A.; Odzhaev, V., Synthesis of silver nanoparticles by the ion implantation method and investigation of their optical properties. ***J. Appl. Spectrosc.**, 72* (2), 229-234, (2005).

57. Popović, M.; Novaković, M.; Noga, P.; Vaňa, D.; Rakočević, Z., Synthesis of AuAg@Ag core/shell bimetallic nanoparticles in titanium nitride thin films by sequential ion implantation. ***Appl. Surf. Sci.**, 481*, 1418-1424, (2019).

58. Fu, Y.; Liang, F.; Tian, H.; Hu, J., Nonenzymatic glucose sensor based on ITO electrode modified with gold nanoparticles by ion implantation. ***Electrochim. Acta**, 120*, 314-318, (2014).

59. Nie, W.; Zhang, Y.; Yu, H.; Li, R.; He, R.; Dong, N.; Wang, J.; Hübner, R.; Böttger, R.; Zhou, S., Plasmonic nanoparticles embedded in single crystals synthesized by gold ion implantation for enhanced optical nonlinearity and efficient Q-switched lasing. ***Nanoscale**, 10* (9), 4228-4236, (2018).

60. Li, C.; Feng, H.; Liu, B.; Liang, W.; Liu, G.; Ross, G. G.; Wang, Y.; Barba, D., Effect of nanocavities on Ge nanoclustering and out-diffusion in SiO_2. ***Nanotechnology**, 28* (3), 035707, (2016).

61. Barba, D.; Martin, F.; Demarche, J.; Terwagne, G.; Ross, G., Nanocavities and germanium nanocrystals produced by Ge ion implantation in fused silica. ***Nanotechnology**, 23* (14), 145701, (2012).

62. Bera, D.; Qian, L.; Tseng, T.-K.; Holloway, P. H., Quantum dots and their multimodal applications: a review. ***Materials**, 3* (4), 2260-2345, (2010).

63. Henglein, A., Small-particle research: physicochemical properties of extremely small colloidal metal and semiconductor particles. ***Chem. Rev.**, 89* (8), 1861-1873, (1989).

64. Trindade, T.; O'Brien, P.; Pickett, N. L., Nanocrystalline semiconductors: synthesis, properties, and perspectives. ***Chem. Mater.**, 13* (11), 3843-3858, (2001).

65. Kuchibhatla, S. V.; Karakoti, A.; Bera, D.; Seal, S., One dimensional nanostructured materials. ***Prog. Mater. Sci.**, 52* (5), 699-913, (2007).

66. Bera, D.; Qian, L.; Holloway, P. H., *Drug delivery nanoparticles formulation and characterization*. CRC Press: Boca Raton, 2016.

67. Alivisatos, A. P., Perspectives on the physical chemistry of semiconductor nanocrystals. ***J. Phys. Chem.**, 100* (31), 13226-13239, (1996).

68. Alivisatos, A. P., Semiconductor clusters, nanocrystals, and quantum dots. ***Science**, 271* (5251), 933-937, (1996).

69. Cress, C. D.; Hubbard, S. M.; Landi, B. J.; Raffaelle, R. P.; Wilt, D. M., Quantum dot solar cell tolerance to alpha-particle irradiation. ***Appl. Phys. Lett.**, 91* (18), 183108, (2007).

70. Chuang, C.-H. M.; Brown, P. R.; Bulović, V.; Bawendi, M. G., Improved performance and stability in quantum dot solar cells through band alignment engineering. ***Nat. Mater.**, 13* (8), 796, (2014).

71. Yu, X.-Y.; Liao, J.-Y.; Qiu, K.-Q.; Kuang, D.-B.; Su, C.-Y., Dynamic study of highly efficient CdS/CdSe quantum dot-sensitized solar cells fabricated by electrodeposition. ***ACS Nano**, 5* (12), 9494-9500, (2011).

72. Selopal, G. S.; Zhao, H.; Tong, X.; Benetti, D.; Navarro-Pardo, F.; Zhou, Y.; Barba, D.; Vidal, F.; Wang, Z. M.; Rosei, F., Highly stable colloidal “giant” quantum dots sensitized solar cells. ***Adv. Funct. Mater.**, 27* (30), 1701468, (2017).

73. Zhao, H.; Rosei, F., Colloidal quantum dots for solar technologies. ***Chem**, 3* (2), 229-258, (2017).

74. Etgar, L.; Yanover, D.; Čapek, R. K.; Vaxenburg, R.; Xue, Z.; Liu, B.; Nazeeruddin, M. K.; Lifshitz, E.; Grätzel, M., Core/shell PbSe/PbS QDs TiO_2 heterojunction solar cell. ***Adv. Funct. Mater.**, 23* (21), 2736-2741, (2013).

75. Campbell, I. H.; Crone, B. K., Quantum-dot/organic semiconductor composites for radiation detection. ***Adv. Mater.**, 18* (1), 77-79, (2006).

76. Letant, S.; Wang, T.-F., Semiconductor quantum dot scintillation under γ-ray irradiation. ***Nano Lett.**, 6* (12), 2877-2880, (2006).

77. Gao, X.; Kang, Q.; Yeow, J.; Barnett, R., Design and evaluation of quantum dot sensors for making superficial X-ray energy radiation measurements. ***Nanotechnology**, 21* (28), 285502, (2010).

78. Zhou, Y.; Zhao, H.; Ma, D.; Rosei, F., Harnessing the properties of colloidal quantum dots in luminescent solar concentrators. ***Chem. Soc. Rev.**, 47* (15), 5866-5890, (2018).

79. Navarro-Pardo, F.; Zhao, H.; Wang, Z. M.; Rosei, F., Structure/property relations in "giant" semiconductor nanocrystals: opportunities in photonics and electronics. ***Accounts. Chem. Res.**, 51* (3), 609-618, (2017).

80. Erickson, C. S.; Bradshaw, L. R.; McDowall, S.; Gilbertson, J. D.; Gamelin, D. R.; Patrick, D. L., Zero-reabsorption doped-nanocrystal luminescent solar concentrators. ***ACS Nano**, 8* (4), 3461-3467, (2014).

81. Zhao, H.; Benetti, D.; Jin, L.; Zhou, Y.; Rosei, F.; Vomiero, A., Absorption enhancement in "giant" core/alloyed-shell quantum dots for luminescent solar concentrator. ***Small**, 12* (38), 5354-5365, (2016).

82. Caruge, J.; Halpert, J. E.; Wood, V.; Bulović, V.; Bawendi, M., Colloidal quantum-dot light-emitting diodes with metal-oxide charge transport layers. ***Nat. Photonics**, 2* (4), 247, (2008).

83. Pal, B. N.; Ghosh, Y.; Brovelli, S.; Laocharoensuk, R.; Klimov, V. I.; Hollingsworth, J. A.; Htoon, H., 'Giant' CdSe/CdS core/shell nanocrystal quantum dots as efficient electroluminescent materials: strong influence of shell thickness on light-emitting diode performance. ***Nano Lett.**, 12* (1), 331-336, (2011).

84. Deng, W.; Xu, X.; Zhang, X.; Zhang, Y.; Jin, X.; Wang, L.; Lee, S. T.; Jie, J., Organometal halide perovskite quantum dot light-emitting diodes. ***Adv. Funct. Mater.**, 26* (26), 4797-4802, (2016).

85. Zhu, H.; Song, N.; Lian, T., Wave function engineering for ultrafast charge separation and slow charge recombination in type II core/shell quantum dots. ***J. Am. Chem. Soc.**, 133* (22), 8762-8771, (2011).

86. Smith, A. M.; Nie, S., Semiconductor nanocrystals: structure, properties, and band gap engineering. ***Accounts. Chem. Res.**, 43* (2), 190-200, (2009).

87. Lo, S. S.; Mirkovic, T.; Chuang, C. H.; Burda, C.; Scholes, G. D., Emergent properties resulting from type-II band alignment in semiconductor nanoheterostructures. ***Adv. Mater.**, 23* (2), 180-197, (2011).

88. Hewa-Kasakarage, N. N.; El-Khoury, P. Z.; Tarnovsky, A. N.; Kirsanova, M.; Nemitz, I.; Nemchinov, A.; Zamkov, M., Ultrafast carrier dynamics in type II ZnSe/CdS/ZnSe nanobarbells. ***ACS Nano**, 4* (4), 1837-1844, (2010).

89. Dorfs, D.; Franzl, T.; Osovsky, R.; Brumer, M.; Lifshitz, E.; Klar, T. A.; Eychmüller, A., Type-I and Type-II nanoscale heterostructures based on CdTe nanocrystals: A comparative study. ***Small**, 4* (8), 1148-1152, (2008).

90. Jones, M.; Kumar, S.; Lo, S. S.; Scholes, G. D., Exciton trapping and recombination in type II CdSe/CdTe nanorod heterostructures. ***J. Phys. Chem. C**, 112* (14), 5423-5431, (2008).

91. Chulapakorn, T. Luminescence of Silicon Nanoparticles Synthesized by Ion Implantation. Acta Universitatis Upsaliensis, 2018.

92. Cullis, A.; Canham, L., Visible light emission due to quantum size effects in highly porous crystalline silicon. ***Nature**, 353* (6342), 335, (1991).

93. Fujioka, K.; Hiruoka, M.; Sato, K.; Manabe, N.; Miyasaka, R.; Hanada, S.; Hoshino, A.; Tilley, R. D.; Manome, Y.; Hirakuri, K., Luminescent passive-oxidized silicon quantum dots as biological staining labels and their cytotoxicity effects at high concentration. ***Nanotechnology**, 19* (41), 415102, (2008).

94. Chen, S.; Shen, L.; van Aken, P. A.; Maier, J.; Yu, Y., Dual-functionalized double carbon shells coated silicon nanoparticles for high performance lithium-ion batteries. ***Adv. Mater.**, 29* (21), 1605650, (2017).

95. Gu, M.; Li, Y.; Li, X.; Hu, S.; Zhang, X.; Xu, W.; Thevuthasan, S.; Baer, D. R.; Zhang, J.-G.; Liu, J., In situ TEM study of lithiation behavior of silicon nanoparticles attached to and embedded in a carbon matrix. ***ACS Nano**, 6* (9), 8439-8447, (2012).

96. Zhou, X.; Cao, A.-M.; Wan, L.-J.; Guo, Y.-G., Spin-coated silicon nanoparticle/graphene electrode as a binder-free anode for high-performance lithium-ion batteries. ***Nano Res.**, 5* (12), 845-853, (2012).

97. Ma, S.-d.; Chen, Y.-l.; Feng, J.; Liu, J.-j.; Zuo, X.-w.; Chen, X.-g., One-step synthesis of water-dispersible and biocompatible silicon nanoparticles for selective heparin sensing and cell imaging. ***Anal. Chem.**, 88* (21), 10474-10481, (2016).

98. Dasog, M.; Kehrle, J.; Rieger, B.; Veinot, J. G., Silicon nanocrystals and silicon-polymer hybrids: synthesis, surface engineering, and applications. ***Angew. Chem. Int. Ed.**, 55* (7), 2322-2339, (2016).

99. Kang, Z.; Liu, Y.; Lee, S.-T., Small-sized silicon nanoparticles: new nanolights and nanocatalysts. ***Nanoscale**, 3* (3), 777-791, (2011).

100. Chen, X.; Lu, Q.; Liu, D.; Wu, C.; Liu, M.; Li, H.; Zhang, Y.; Yao, S., Highly sensitive and selective determination of copper (II) based on a dual catalytic effect and by using silicon nanoparticles as a fluorescent probe. ***Microchim. Acta**, 185* (3), 188, (2018).

101. Santos, H. A.; Mäkilä, E.; Airaksinen, A. J.; Bimbo, L. M.; Hirvonen, J., Porous silicon nanoparticles for nanomedicine: preparation and biomedical applications. ***Nanomedicine**, 9* (4), 535-554, (2014).

102. Ahire, J. H.; Chambrier, I.; Mueller, A.; Bao, Y.; Chao, Y., Synthesis of D-mannose capped silicon nanoparticles and their interactions with MCF-7 human breast cancerous cells. ***ACS Appl. Mater. Interfaces**, 5* (15), 7384-7391, (2013).

103. Xiao, L.; Gu, L.; Howell, S. B.; Sailor, M. J., Porous silicon nanoparticle photosensitizers for singlet oxygen and their phototoxicity against cancer cells. ***ACS Nano**, 5* (5), 3651-3659, (2011).

104. McVey, B. F.; Tilley, R. D., Solution synthesis, optical properties, and bioimaging applications of silicon nanocrystals. ***Accounts. Chem. Res.**, 47* (10), 3045-3051, (2014).

105. Schuppler, S.; Friedman, S. L.; Marcus, M.; Adler, D.; Xie, Y.-H.; Ross, F.; Chabal, Y.; Harris, T.; Brus, L.; Brown, W., Size, shape, and composition of luminescent species in oxidized Si nanocrystals and H-passivated porous Si. ***Phys. Rev. B**, 52* (7), 4910, (1995).

106. Saar, A., Photoluminescence from silicon nanostructures: the mutual role of quantum confinement and surface chemistry. ***J. Nanophotonics**, 3* (1), 032501, (2009).

107. Rizza, G.; Coulon, P.; Khomenkov, V.; Dufour, C.; Monnet, I.; Toulemonde, M.; Perruchas, S.; Gacoin, T.; Mailly, D.; Lafosse, X., Rational description of the ion-beam shaping mechanism. ***Phys. Rev. B**, 86* (3), 035450, (2012).

108. Bufford, D.; Pratt, S. H.; Boyle, T. J.; Hattar, K., In situ TEM ion irradiation and implantation effects on Au nanoparticle morphologies. ***Chem. Commun.**, 50* (57), 7593-7596, (2014).

109. Mishra, Y.; Singh, F.; Avasthi, D.; Pivin, J.; Malinovska, D.; Pippel, E., Synthesis of elongated Au nanoparticles in silica matrix by ion irradiation. ***Appl. Phys. Lett.**, 91* (6), 063103, (2007).

110. Araujo, L.; Giulian, R.; Sprouster, D.; Schnohr, C.; Llewellyn, D.; Johannessen, B.; Byrne, A.; Ridgway, M. C., Structural properties of embedded Ge nanoparticles modified by swift heavy-ion irradiation. ***Phys. Rev. B**, 85* (23), 235417, (2012).

111. Järvi, T.; Pohl, D.; Albe, K.; Rellinghaus, B.; Schultz, L.; Fassbender, J.; Kuronen, A.; Nordlund, K., From multiply twinned to fcc nanoparticles via irradiation-induced transient amorphization. ***Europhys. Lett.**, 85* (2), 26001, (2009).

112. Järvi, T. T.; Kuronen, A.; Nordlund, K.; Albe, K., Structural modification of a multiply twinned nanoparticle by ion irradiation: A molecular dynamics study. ***J. Appl. Phys.**, 102* (12), 124304, (2007).

113. Dmitrieva, O.; Rellinghaus, B.; Kästner, J.; Liedke, M. O.; Fassbender, J., Ion beam induced destabilization of icosahedral structures in gas phase prepared FePt nanoparticles. ***J. Appl. Phys.**, 97* (10), 10N112, (2005).

114. Pacifici, D.; Moreira, E.; Franzo, G.; Martorino, V.; Priolo, F.; Iacona, F., Defect production and annealing in ion-irradiated Si nanocrystals. ***Phys. Rev. B**, 65* (14), 144109, (2002).

115. Leon, R.; Marcinkecius, S.; Siegert, J.; Cechavicius, B.; Magness, B.; Taylor, W.; Lobo, C., Effects of proton irradiation on luminescence emission and carrier dynamics of self-assembled III-V quantum dots. ***IEEE Trans. Nucl. Sci.**, 49* (6), 2844-2851, (2002).

116. Leon, R.; Swift, G.; Magness, B.; Taylor, W.; Tang, Y.; Wang, K.; Dowd, P.; Zhang, Y., Changes in luminescence emission induced by proton irradiation: InGaAs/GaAs quantum wells and quantum dots. ***Appl. Phys. Lett.**, 76* (15), 2074-2076, (2000).

117. Lu, W.; Ji, Y.; Chen, G.; Tang, N.; Chen, X.; Shen, S.; Zhao, Q.; Willander, M., Enhancement of room-temperature photoluminescence in InAs quantum dots. ***Appl. Phys. Lett.**, 83* (21), 4300-4302, (2003).

118. Ji, Y.; Chen, G.; Tang, N.; Wang, Q.; Wang, X.; Shao, J.; Chen, X.; Lu, W., Proton-implantation-induced photoluminescence enhancement in self-assembled InAs/GaAs quantum dots. ***Appl. Phys. Lett.**, 82* (17), 2802-2804, (2003).

119. Zanazzi, E.; Favaro, M.; Ficorella, A.; Pancheri, L.; Dalla Betta, G.; Quaranta, A., Photoluminescence enhancement of colloidal CdSe/ZnS quantum dots embedded in polyvinyl alcohol after 2 MeV proton irradiation: Crucial role of the embedding medium. ***Opt. Mater.****, 88*, 271-276, (2019).

120. Bratchenko, M.; Bryk, V.; Dyuldya, S.; Kalchenko, A.; Lazarev, N.; Voyevodin, V., Comments on DPA calculation methods for ion beam driven simulation irradiations. ***Probl. At. Sci. Technol.***, (2013).

121. ASTM Standard, E., Standard Practice for Neutron Radiation Damage Simulation by Charged-Particle Irradiation. ASTM International: 2009.

122. Norgett, M.; Robinson, M.; Torrens, I., A proposed method of calculating displacement dose rates. ***Nucl. Eng. Des.****, 33* (1), 50-54, (1975).

123. Kinchin, G.; Pease, R., The displacement of atoms in solids by radiation. ***Rep. Prog. Phys.****, 18* (1), 1, (1955).

124. Volkert, C. A.; Minor, A. M., Focused ion beam microscopy and micromachining. ***Mrs. Bull.****, 32* (5), 389-399, (2007).

125. Feldman, M., *Nanolithography: the art of fabricating nanoelectronic and nanophotonic devices and systems*. Woodhead publishing: 2014.

126. Giannuzzi, L. A.; Stevie, F. A., A review of focused ion beam milling techniques for TEM specimen preparation. ***Micron****, 30* (3), 197-204, (1999).

127. Introduction: focused ion beam systems. Available from: http://www.fibics.com/fib/tutorials/introduction-focused-ion-beam-systems/4/.

128. Seidl, R. Specimen Preparation for Transmission Electron Microscopy by Focused Ion Beam: Refinement of Post-Treatment using Focused Low Energy Argon Ion Milling. Graz University of Technology, 2016.

129. Williams, D. B., *Transmission Electron Microscopy*. Springer Science & Business Media: New York, 2009.

130. Smith, D. J., Ultimate resolution in the electron microscope? ***Materials Today****, 11*, 30-38, (2008).

131. Li, C.; Zhang, Q.; Mayoral, A., Ten Years of Aberration Corrected Electron Microscopy for Ordered Nanoporous Materials. ***ChemCatChem***, (2020).

132. Russ, J. C., *Fundamentals of Energy Dispersive X-Ray Analysis: Butterworths Monographs in Materials*. Butterworth-Heinemann: 2013.

133. Adhikari, R.; Jin, L.; Navarro-Pardo, F.; Benetti, D.; AlOtaibi, B.; Vanka, S.; Zhao, H.; Mi, Z.; Vomiero, A.; Rosei, F., High efficiency, Pt-free photoelectrochemical cells for solar hydrogen generation based on "giant" quantum dots. ***Nano Energy**, 27*, 265-274, (2016).

134. Zhao, H.; Fan, Z.; Liang, H.; Selopal, G.; Gonfa, B.; Jin, L.; Soudi, A.; Cui, D.; Enrichi, F.; Natile, M., Controlling photoinduced electron transfer from PbS@CdS core@shell quantum dots to metal oxide nanostructured thin films. ***Nanoscale**, 6* (12), 7004-7011, (2014).

135. Wahl, M., Time-correlated single photon counting. ***Technical Note***, 1-14, (2014).

136. Tompkins, H.; Irene, E. A., *Handbook of ellipsometry*. William Andrew: New York, 2005.

137. Tong, X.; Kong, X.-T.; Wang, C.; Zhou, Y.; Navarro-Pardo, F.; Barba, D.; Ma, D.; Sun, S.; Govorov, A. O.; Zhao, H.; Wang, Z. M.; Rosei, F., Optoelectronic properties in near-infrared colloidal heterostructured pyramidal "giant" Core/Shell quantum dots. ***Adv. Sci.**, 5* (8), 1800656, (2018).

138. Algra, R. E.; Verheijen, M. A.; Borgström, M. T.; Feiner, L.-F.; Immink, G.; van Enckevort, W. J.; Vlieg, E.; Bakkers, E. P., Twinning superlattices in indium phosphide nanowires. ***Nature**, 456* (7220), 369, (2008).

139. Van Dijken, A.; Meulenkamp, E. A.; Vanmaekelbergh, D.; Meijerink, A., The kinetics of the radiative and nonradiative processes in nanocrystalline ZnO particles upon photoexcitation. ***J. Phys. Chem. B**, 104* (8), 1715-1723, (2000).

140. Borgschulte, A.; Sambalova, O.; Delmelle, R.; Jenatsch, S.; Hany, R.; Nüesch, F., Hydrogen reduction of molybdenum oxide at room temperature. ***Sci. Rep.**, 7*, 40761, (2017).

141. Meyer, J.; Hamwi, S.; Kröger, M.; Kowalsky, W.; Riedl, T.; Kahn, A., Transition metal oxides for organic electronics: energetics, device physics and applications. ***Adv. Mater.**, 24* (40), 5408-5427, (2012).

142. Wu, Y.; Wang, H.; Tu, W.; Wu, S.; Chew, J. W., Construction of hole-transported MoO_{3-x} coupled with CdS nanospheres for boosting photocatalytic performance via oxygen-defects-mediated Z-scheme charge transfer. ***Appl. Organomet. Chem.***, e4780, (2019).

143. Shen, S.; Chen, J.; Wang, M.; Sheng, X.; Chen, X.; Feng, X.; Mao, S. S., Titanium dioxide nanostructures for photoelectrochemical applications. ***Prog. Mater. Sci.***, *98*, 299-385, (2018).

144. Nesheva, D., Properties of amorphous CdS-crystalline Si junctions. ***Solid-State Electron.***, *30* (2), 173-176, (1987).

145. Blackman, B.; Battaglia, D. M.; Mishima, T. D.; Johnson, M. B.; Peng, X., Control of the morphology of complex semiconductor nanocrystals with a type II heterojunction, dots vs peanuts, by thermal cycling. ***Chem. Mater.***, *19* (15), 3815-3821, (2007).

146. Young, D. L.; Nemeth, W.; LaSalvia, V.; Page, M. R.; Theingi, S.; Aguiar, J.; Lee, B. G.; Stradins, P., Low-cost plasma immersion ion implantation doping for interdigitated back passivated contact (IBPC) solar cells. ***Sol. Energ. Mater. Sol. C.***, *158*, 68-76, (2016).

147. García-Santamaría, F.; Chen, Y.; Vela, J.; Schaller, R. D.; Hollingsworth, J. A.; Klimov, V. I., Suppressed auger recombination in “giant” nanocrystals boosts optical gain performance. ***Nano Lett.***, *9* (10), 3482-3488, (2009).

148. Brovelli, S.; Schaller, R. D.; Crooker, S.; García-Santamaría, F.; Chen, Y.; Viswanatha, R.; Hollingsworth, J. A.; Htoon, H.; Klimov, V. I., Nano-engineered electron-hole exchange interaction controls exciton dynamics in core–shell semiconductor nanocrystals. ***Nat. Commun.***, *2*, 280, (2011).

149. Tong, X.; Kong, X.-T.; Zhou, Y.; Navarro-Pardo, F.; Selopal, G. S.; Sun, S.; Govorov, A. O.; Zhao, H.; Wang, Z. M.; Rosei, F., Near-infrared, heavy metal-free colloidal "giant" core/shell quantum dots. ***Adv. Energy Mater.***, *8* (2), 1701432, (2018).

150. Chen, O.; Zhao, J.; Chauhan, V. P.; Cui, J.; Wong, C.; Harris, D. K.; Wei, H.; Han, H.-S.; Fukumura, D.; Jain, R. K., Compact high-quality CdSe-CdS core-shell nanocrystals with narrow emission linewidths and suppressed blinking. ***Nat. Mater.***, *12* (5), 445, (2013).

151. Chen, C.-C.; Zhu, C.; White, E. R.; Chiu, C.-Y.; Scott, M.; Regan, B.; Marks, L. D.; Huang, Y.; Miao, J., Three-dimensional imaging of dislocations in a nanoparticle at atomic resolution. ***Nature***, *496* (7443), 74-77, (2013).

152. Guo, W.; Li, J. J.; Wang, Y. A.; Peng, X., Luminescent CdSe/CdS core/shell nanocrystals in dendron boxes: superior chemical, photochemical and thermal stability. ***J. Am. Chem. Soc.***, *125* (13), 3901-3909, (2003).

153. Yuan, X.; Zheng, J.; Zeng, R.; Jing, P.; Ji, W.; Zhao, J.; Yang, W.; Li, H., Thermal stability of Mn^{2+} ion luminescence in Mn-doped core-shell quantum dots. ***Nanoscale**, 6* (1), 300-307, (2014).

154. Yu, M.; Bovet, N.; Satterley, C. J.; Bengio, S.; Lovelock, K. R.; Milligan, P.; Jones, R. G.; Woodruff, D.; Dhanak, V., True nature of an archetypal self-assembly system: Mobile Au-thiolate species on Au (111). ***Phys. Rev. Lett.**, 97* (16), 166102, (2006).

155. Panzer, R.; Guhrenz, C.; Haubold, D.; Hübner, R.; Gaponik, N.; Eychmüller, A.; Weigand, J. J., Versatile tri (pyrazolyl) phosphanes as phosphorus precursors for the synthesis of highly emitting InP/ZnS quantum dots. ***Angew. Chem. Int. Ed.**, 56* (46), 14737-14742, (2017).

156. Chu, M.-W.; Szafraniak, I.; Scholz, R.; Harnagea, C.; Hesse, D.; Alexe, M.; Gösele, U., Impact of misfit dislocations on the polarization instability of epitaxial nanostructured ferroelectric perovskites. ***Nat. Mater.**, 3* (2), 87-90, (2004).

157. Wang, Z. L., Transmission electron microscopy of shape-controlled nanocrystals and their assemblies. ***J. Phys. Chem. B**, 104* (6), 1153-1175, (2000).

158. Maksimuk, S.; Teng, X.; Yang, H., Roles of twin defects in the formation of platinum multipod nanocrystals. ***J. Phys. Chem. C**, 111* (39), 14312-14319, (2007).

159. Wang, C.; Xu, J.; Wang, Y.; Xu, S.; Qi, Z.; Lu, C.; Cui, Y., Manipulation of irradiative defects at MnSe and ZnSe dopant-host interface. ***Adv. Funct. Mater.**, 26* (24), 4274-4282, (2016).

160. Plumhof, J.; Křápek, V.; Wang, L.; Schliwa, A.; Bimberg, D.; Rastelli, A.; Schmidt, O., Experimental investigation and modeling of the fine structure splitting of neutral excitons in strain-free GaAs/Al_xGa_{1-x} As quantum dots. ***Phys. Rev. B**, 81* (12), 121309, (2010).

161. Hunter, A.; Beyerlein, I.; Germann, T. C.; Koslowski, M., Influence of the stacking fault energy surface on partial dislocations in fcc metals with a three-dimensional phase field dislocations dynamics model. ***Phys. Rev. B**, 84* (14), 144108, (2011).

162. Egerton, R.; Li, P.; Malac, M., Radiation damage in the TEM and SEM. ***Micron**, 35* (6), 399-409, (2004).

163. Gilbert, M.; Queyreau, S.; Marian, J., Stress and temperature dependence of screw dislocation mobility in α-Fe by molecular dynamics. ***Phys. Rev. B**, 84* (17), 174103, (2011).

164. Wei, X.; Wang, M.-S.; Bando, Y.; Golberg, D., Thermal stability of carbon nanotubes probed by anchored tungsten nanoparticles. ***Sci. Technol. Adv. Mater.****, 12* (4), 044605, (2011).

165. Chen, S.; Huang, J.; Wang, Z.; Kempa, K.; Chen, G.; Ren, Z., High-bias-induced structure and the corresponding electronic property changes in carbon nanotubes. ***Appl. Phys. Lett.****, 87* (26), 263107, (2005).

166. Naka, S.; Lasalmonie, A.; Costa, P.; Kubin, L., The low-temperature plastic deformation of α-titanium and the core structure of a-type screw dislocations. ***Philos. Mag. A****, 57* (5), 717-740, (1988).

167. Sotniczuk, A.; Kuczyńska-Zemła, D.; Królikowski, A.; Garbacz, H., Enhancement of the corrosion resistance and mechanical properties of nanocrystalline titanium by low-temperature annealing. ***Corros. Sci.****, 147*, 342-349, (2019).

168. Hao, J.-J.; Zhou, J.; Zhang, C.-Y., A tri-n-octylphosphine-assisted successive ionic layer adsorption and reaction method to synthesize multilayered core–shell CdSe–ZnS quantum dots with extremely high quantum yield. ***Chem. Commun.****, 49* (56), 6346-6348, (2013).

169. De Heer, W. A.; Chatelain, A.; Ugarte, D., A carbon nanotube field-emission electron source. ***Science****, 270* (5239), 1179-1180, (1995).

170. Lieberman, M. A., Model of plasma immersion ion implantation. ***J. Appl. Phys.****, 66* (7), 2926-2929, (1989).

171. Bradley, J. D.; Hosseini, E. S., Monolithic erbium-and ytterbium-doped microring lasers on silicon chips. ***Opt. Express****, 22* (10), 12226-12237, (2014).

172. Chen, H.; Jin, C.; Huang, B.; Fontaine, N.; Ryf, R.; Shang, K.; Grégoire, N.; Morency, S.; Essiambre, R.-J.; Li, G., Integrated cladding-pumped multicore few-mode erbium-doped fibre amplifier for space-division-multiplexed communications. ***Nat. Photonics***, (2016).

173. Saglamyurek, E.; Jin, J.; Verma, V. B.; Shaw, M. D.; Marsili, F.; Nam, S. W.; Oblak, D.; Tittel, W., Quantum storage of entangled telecom-wavelength photons in an erbium-doped optical fibre. ***Nat. Photonics****, 9* (2), 83-87, (2015).

174. Mebrouk, Y.; Mady, F.; Benabdesselam, M.; Duchez, J.-B.; Blanc, W., Experimental evidence of Er^{3+} ion reduction in the radiation-induced degradation of erbium-doped silica fibers. ***Opt. Lett.****, 39* (21), 6154-6157, (2014).

175. Zotov, K.; Likhachev, M.; Tomashuk, A.; Bubnov, M.; Yashkov, M.; Guryanov, A.; Klyamkin, S., Radiation-resistant erbium-doped fiber for spacecraft applications. ***IEEE Trans. Nucl. Sci.**, 55* (4), 2213, (2008).

176. Gusarov, A.; Van Uffelen, M.; Hotoleanu, M.; Thienpont, H.; Berghmans, F., Radiation sensitivity of EDFAs based on highly Er-doped fibers. ***J. Lightwave Technol.**, 27* (11), 1540-1545, (2009).

177. Celikin, M.; Barba, D.; Ruediger, A.; Chicoine, M.; Schiettekatte, F.; Rosei, F., Co-mediated nucleation of erbium/silicon nanoclusters in fused silica. ***J. Mater. Res.**, 30*, 3003, (2015).

178. Egerton, R. F., *Electron energy-loss spectroscopy in the electron microscope*. Springer: New York, 2011.

179. Lu, Y.-W.; Julsgaard, B.; Petersen, M. C.; Jensen, R. S.; Pedersen, T. G.; Pedersen, K.; Larsen, A. N., Erbium diffusion in silicon dioxide. ***Appl. Phys. Lett.**, 97* (14), 141903, (2010).

180. Tsoukalas, D.; Tsamis, C.; Normand, P., Diffusivity measurements of silicon in silicon dioxide layers using isotopically pure material. ***J. Appl. Phys.**, 89* (12), 7809-7813, (2001).

181. Ren, Y.-G. F. Erbium doped silicon as an optoelectronic semiconductor material. Doctoral dissertation, Massachusetts Institute of Technology, 1994.

182. Luzan, S.; Buyanov, Y. I.; Martsenyuk, P., Phase equilibria in the erbium-silicon system. ***Powder Metall. Met. Ceram**, 36* (1-2), 24-29, (1997).

183. Zhang, M.; Cai, R.; Zhang, Y.; Wang, C.; Wang, Y.; Ross, G. G.; Barba, D., Evolution of microstructural defects with strain effects in germanium nanocrystals synthesized at different annealing temperatures. ***Mater. Charact.**, 93*, 1-9, (2014).

184. Travlos, A.; Salamouras, N.; Flouda, E., Epitaxial erbium silicide films on (100) silicon: growth, structure and electrical properties. ***Appl. Surf. Sci.**, 120* (3), 355-364, (1997).

185. Sullivan, A. H., *A Guide to Radiation and Radioactivity Levels Near High Energy Particle Accelerators*. Nuclear Technology Publishing: Kent, 1992.

186. Sickafus, K. E.; Grimes, R. W.; Valdez, J. A.; Cleave, A.; Tang, M.; Ishimaru, M.; Corish, S. M.; Stanek, C. R.; Uberuaga, B. P., Radiation-induced amorphization resistance and radiation tolerance in structurally related oxides. ***Nat. Mater.**, 6* (3), 217-223, (2007).

187. Pacifici, D.; Franzo, G.; Priolo, F.; Iacona, F.; Dal Negro, L., Modeling and perspectives of the Si nanocrystals-Er interaction for optical amplification. ***Phys. Rev. B**, 67* (24), 245301, (2003).

188. Kanjilal, A.; Rebohle, L.; Voelskow, M.; Skorupa, W.; Helm, M., Influence of annealing on the Er luminescence in Si-rich SiO_2 layers coimplanted with Er ions. ***J. Appl. Phys.**, 104* (10), 103522, (2008).

189. Senter, R. A.; Chen, Y.; Coffer, J. L.; Tessler, L. R., Synthesis of silicon nanocrystals with erbium-rich surface layers. ***Nano Lett.**, 1* (7), 383-386, (2001).

190. Navarro-Urrios, D.; Jambois, O.; Lupi, F. F.; Pellegrino, P.; Garrido, B.; Pitanti, A.; Prtljaga, N.; Daldosso, N.; Pavesi, L., Si nanoclusters coupled to Er^{3+} ions in a SiO_2 matrix for optical amplifiers. ***Opt. Mater.**, 33* (7), 1086-1090, (2011).

191. Boucher, R. H.; Woodward, W. F.; Lomheim, T. S.; Shima, R. M.; Asman, D. J.; Killian, K. M.; LeGrand, J.; Goellner, G. J., Proton-induced degradation in interferometric fiber optic gyroscopes. ***Opt. Eng.**, 35* (4), 955-976, (1996).

192. Girard, S.; Tortech, B.; Regnier, E.; Van Uffelen, M.; Gusarov, A.; Ouerdane, Y.; Baggio, J.; Paillet, P.; Ferlet-Cavrois, V.; Boukenter, A., Proton-and gamma-induced effects on erbium-doped optical fibers. ***IEEE Trans. Nucl. Sci.**, 54* (6), 2426-2434, (2007).

193. Fu, X.; Song, L.; Li, J., Radiation induced color centers in silica glasses of different OH content. ***Nucl. Instrum. Methods Phys. Res. B**, 330*, 7-10, (2014).

194. Demarche, J.; Barba, D.; Ross, G.; Terwagne, G., Ionodeterioration of the silicon nanocrystal photoluminescence. ***J. Appl. Phys.**, 110* (11), 114904, (2011).

195. Tortech, B.; Girard, S.; Regnier, E.; Ouerdane, Y.; Boukenter, A.; Meunier, J.-P.; Van Uffelen, M.; Gusarov, A.; Berghmans, F.; Thienpont, H., Core versus cladding effects of proton irradiation on erbium-doped optical fiber: micro-luminescence study. ***IEEE Trans. Nucl. Sci.**, 55* (4), 2223-2228, (2008).

196. Yu, Y.; He, T.; Guo, L.; Yang, Y.; Guo, L.; Tang, Y.; Cao, Y., Efficient visible-light photocatalytic degradation system assisted by conventional Pd catalysis. ***Sci. Rep.**, 5*, 9561, (2015).

197. Pearton, S.; Ren, F.; Patrick, E.; Law, M.; Polyakov, A. Y., Review-ionizing radiation damage effects on GaN devices. ***ECS J. Solid State Sc.**, 5* (2), Q35-Q60, (2016).

198. Ionascut-Nedelcescu, A.; Carlone, C.; Houdayer, A.; Von Bardeleben, H.; Cantin, J.-L.; Raymond, S., Radiation hardness of gallium nitride. ***IEEE Trans. Nucl. Sci.**, 49* (6), 2733-2738, (2002).

199. Koutský, J.; Kocik, J., *Radiation damage of structural materials*. Elsevier: New York, 1994.

8 ANNEXE I

8.1 The Stopping and Range of Ions in Matter Software

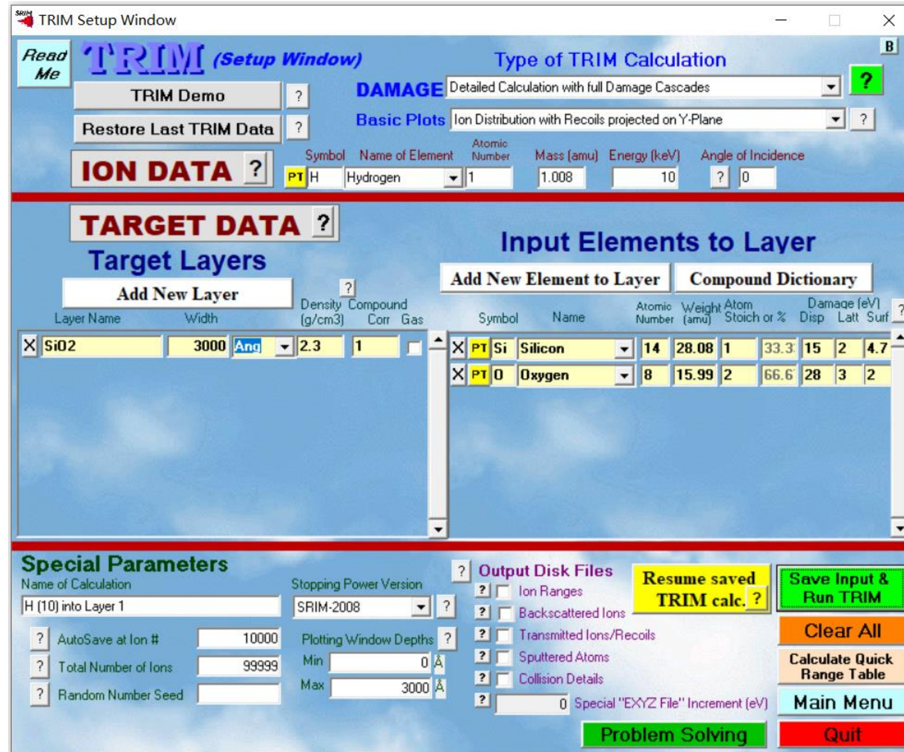

Figure S1 SRIM setup window of proton implantation.

SRIM has an easy-to-use user interface and built-in parameters for different ions and materials. Figure S1 shows a typical user inputs for the calculation of 10 keV H^+ implanting into SiO_2 subtract. Parameters, such as name of element, atomic number, mass, energy and angle of incidence can be set in the ION DATA region. Target layer information including name, width, density and the element inside can be entered from TARGET DATA region. “Ion Distribution and Quick Calculation of Damage” and “Detailed Calculation with Full Damage Cascades” can be selected through scrolling down the DAMAGE. After setting all the parameters, pressing “Save Input and Run TRIM” can start calculations.

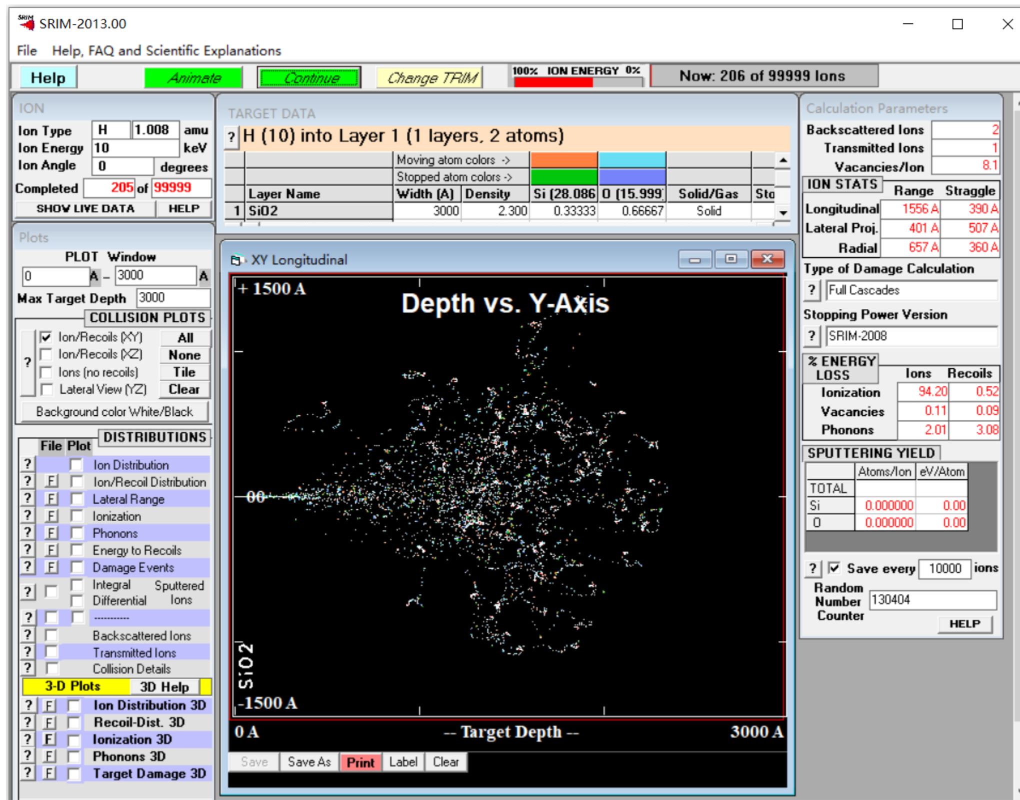

Figure S2 SRIM calculation window of 10 keV H^{+} implanting into SiO_2 subtract.

Figure S2 show the SRIM calculation window of 10 keV H^{+} implanting into SiO_2 subtract with thickness of 3000 Å. Every time the proton hits a silicon or oxygen atom and transfer a significant portion of its energy. A table named DISTRIBUTIONS on the bottom left corner has various buttons, such as “Ion Distribution”, “Ion/Recoil Distribution”, “Damage Events”, etc. For example, if click “Ion Distribution” button, a plot will appear with title of ION RANGES. The unit of longitudinal coordinate-axis Y is “(atoms/cm^3)/(atoms/cm^2)”. If multiply by the implantation dose (ions/cm^2), ion concentration with unit of atoms/cm^3 can be acquired. Similarly, the plots of “COLLISION EVENTS”, “ENERGY OF RECOILS” and “ATOM DISTRIBUTIONS” will appear by clicking the corresponding buttons.

8.2 DigitalMicrograph^{TM} Scripting

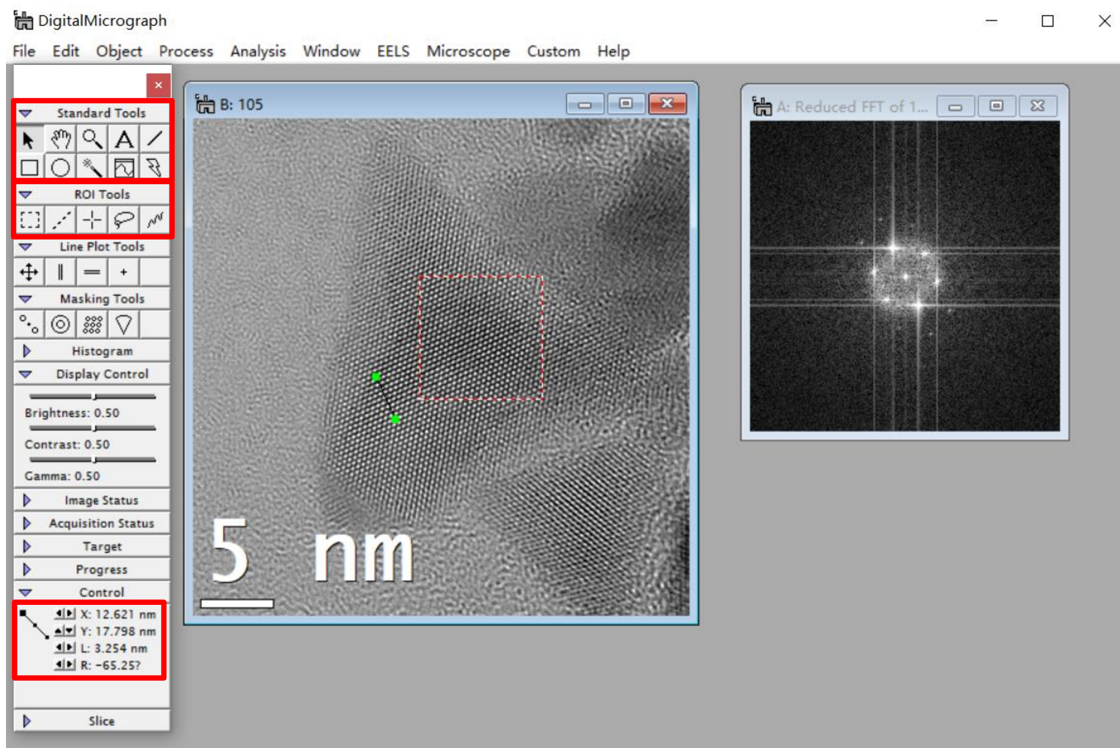

Figure S3 DigitalMicrograph window for d-spacing measurements, interfacial angle measurements and fast Fourier transform.

DigitalMicrograph designed by Gatan company is a powerful image processing software used by the majority of TEM users in the world. Using standard tools can easily measure d-spacing and interfacial angle of two adjacent crystal faces, which are crucial for the determination of crystal face. The measured length and rotation angle are presented in the Control bar. The tools in ROI bar can be applied to select interesting region for fast Fourier transform. The Batch Convert in the File menu can be used to convert dm3 image to JPEG or TIFF format, which can be read by most of image processing software, such as Photoshop or Power Point.

9 ANNEXE II

SOMMAIRE RÉCAPITULATIF

L'effet des rayonnements ionisants sur la microstructure et les propriétés physiques des nanoparticules

L’introduction

L'irradiation des solides par des particules haute énergie, telles que des électrons ou des ions, entraîne normalement la formation de défauts atomiques dans la cible et altère les propriétés du matériau. Récemment, la nécessité de comprendre la dégradation des matériaux induite par l'irradiation pour les applications spatiales nous a incités à étudier les effets de l'irradiation sur les solides. Les matériaux utilisés dans l'espace doivent résister à des environnements qui combinent rayonnements ionisants, températures extrêmes, micrométéorites, etc. Plusieurs missions impliquent des menaces supplémentaires. Par exemple, les orbites terrestres basses et les orbites géostationnaires (OTB/GEO) entraînent des dégradations importantes induites par l’ozone, tandis que les missions dans l'espace lointain impliquent des niveaux élevés de rayonnements ionisants. Les principales conditions requises pour les matériaux spatiaux sont les suivantes : légèreté (pour réduire les coûts de lancement), conservation de l'énergie, longue durée de vie opérationnelle et meilleure résistance aux rayonnements ionisants, tels que les électrons, les protons et autres ions lourds. Les nanomatériaux sont extrêmement intéressants, car ils laissent entrevoir une réduction du volume, du poids et de la consommation d'énergie, avec des performances accrues et une meilleure

résistance au rayonnement cosmique. Toutefois, leurs propriétés physiques dans l'environnement spatial restent à étudier.

Les rayons cosmiques que l'on retrouve dans l'espace sont composés d'environ 91% de protons, 8% d'hélium et 1% d'ions lourds ayant une énergie comprise entre quelques 100 MeV et 100 GeV. Les doses de rayonnement typiques associées au flux de protons sur les orbites OTB ou GEO au sein des modules spatiaux se situent entre 80 et 120 mGy (0,8 à 1,2 mrad) par an, ce qui entraîne une dégradation irréversible des dispositifs à semi-conducteurs. Pour planifier une mission spatiale, il est important d'évaluer la modification des performances de tout équipement embarqué (comme un laser, un détecteur, une cellule solaire, un amplificateur à fibre, etc.) sous irradiation. Par conséquent, avant d'utiliser des matériaux dans un environnement exposé aux rayonnements, il est nécessaire de tester leur stabilité. À cette fin, différentes expériences d'irradiation ionique doivent être réalisées sur ces matériaux afin d'étudier comment leur structure et leurs performances sont modifiées.

L'interaction de l'irradiation de particules chargées (alpha, bêta et protons) avec la matière est différente de celle des radiations neutres (rayons X, gamma et neutrons). Les particules chargées, qui ionisent les atomes par interaction avec les électrons de leurs atomes, sont dites directement ionisantes, tandis que les rayons gamma ou les neutrons, qui produisent une particule chargée pouvant ensuite ioniser d'autres atomes d'un matériau, sont classés comme indirectement ionisants. Plusieurs types de rayonnements ionisants et leur interaction avec la matière sont illustrés à la figure R1.

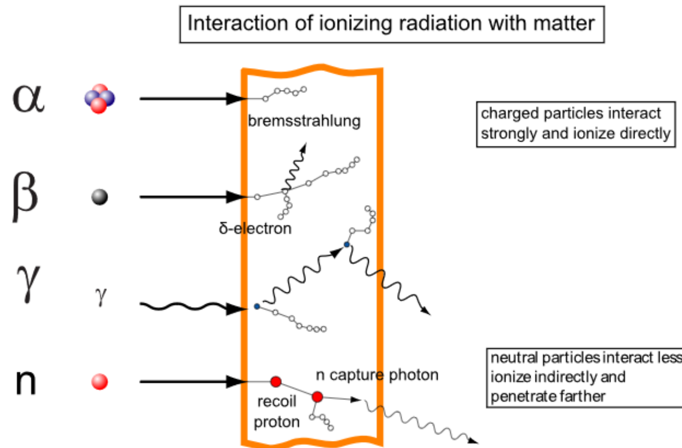

Figure R1 **Types de rayonnements ionisants et leur interaction avec la matière ; les trajectoires des particules telles que celles des alphas, des bêtas (électrons) et des neutrons sont représentées par des lignes droites tandis que les lignes ondulées représentent les rayons gamma. Les cercles vides montrent les endroits où l'ionisation se produit.**

Les ions hautement énergétiques qui pénètrent dans les matériaux perdent leur énergie par (i) des collisions élastiques avec les noyaux des atomes cibles et (ii) des interactions avec le gaz d'électrons. L'énergie perdue par les ions lors des collisions élastiques est également appelée "pouvoir d'arrêt nucléaire". Le processus de collision peut être considéré comme une diffusion élastique de deux corps, tel qu’illustré à la figure R2.

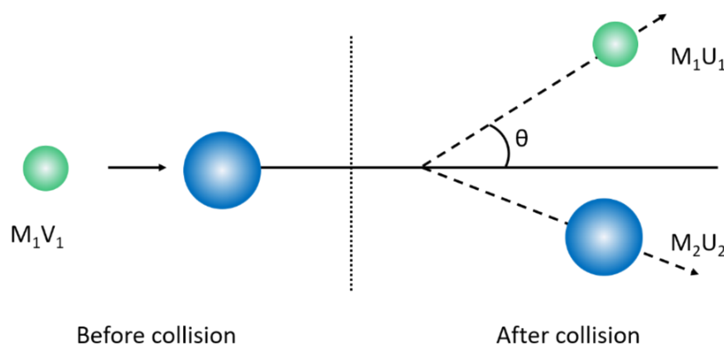

Figure R2 **Collision élastique entre deux atomes.**

Objectifs

Nos deux principaux objectifs sont de parvenir à une compréhension fondamentale des altérations radio-induites des nanoparticules (NP) et d'étudier leurs effets sur les propriétés des matériaux. Les modifications dans la microstructure sont liées aux variations de l'émission et de l'absorption optique des NP et de la résistivité des électrons après irradiation. Plus précisément, nos travaux visent à :

(1) Synthétiser et caractériser des NP Er/Si stables et résistantes aux radiations à l'intérieur de substrats de verre de silice en fonction de différents paramètres de fabrication, tels que la dose d'implantation, l'énergie d'implantation et la température de recuit.

(2) Mener des expériences d'irradiation à l'aide d'un faisceau d'électrons (*e-beam*) et d'un faisceau de protons sur différents types de NP.

(3) Étudier l'effet des rayonnements ionisants sur la microstructure et les propriétés physiques des NP, notamment (mais pas exclusivement) :

(a) la caractérisation approfondie des dommages structurels induits par les rayonnements par analyse au microscope électronique à transmission à haute résolution (HRMET) et avec les simulations SRIM (*Stopping and Range of Ions in Matter*), afin de relier les changements microstructurels aux changements de plusieurs propriétés des matériaux.

(b) l'étude de la photoluminescence (PL) et de sa décroissance après irradiation ionique.

(c) l'utilisation de l'irradiation ionique pour montrer l'existence de transferts de photoporteurs dans les systèmes Er/Si et dans les points quantiques (*quantum dots* ou QD) de CdSe/CdS « géants » de type cœur-coquille (*giant core-shell* ou g-CS).

(d) l'utilisation de l'irradiation par faisceau d'électrons pour étudier l'effet du rayonnement d'ions légers sur les QD de $CuInSe_xS_{2-x}$/CdSeS/CdS

(4) Élaborer de nouvelles stratégies pour améliorer les propriétés et la stabilité des nanomatériaux.

Effet de l'irradiation de protons sur les points quantiques de type cœur-coquille

Les QD des groupes II-VI possèdent des propriétés électriques et optiques accordables qui les rendent très attrayants pour les applications de haute technologie et la production d'énergie. Dans ce chapitre, les effets de l'irradiation de protons sur les propriétés structurelles et physiques des QD de CdS/CdSe « géants » de type cœur-coquille (g-CS) sont étudiés. Ces expériences mettent en lumière la délocalisation des photoélectrons dans les QD g-CS, où les courants totaux et les fortes variations de l'émission optique résultent de l'extension spatiale des fonctions d'onde des photoélectrons sur les bandes de conduction du CdSe et du CdS. Des simulations de Monte-Carlo des interactions ion-matière montrent que les taux d'endommagement peuvent être fixés à partir de l'énergie des protons incidents pour favoriser la formation de défauts structurels dans le cœur ou dans la coquille. La formation de nanocavités est démontrée pour des doses d'irradiation supérieures à ~10^{17} H^+/cm^2 et une diminution continue de l'intensité de la luminescence est observée avec l'augmentation de la fluence de protons. Cette caractéristique s'accompagne d'une diminution concomitante du temps de vie, marquant l'augmentation

des phénomènes non radiatifs et l'apparition de transferts de photoporteurs plus importants entre le CdS et le CdSe. La caractérisation courant-tension montrent que l'implantation de protons peut être utilisée pour améliorer la génération de photocourants dans les QD g-CS. Cette augmentation est attribuée à la délocalisation des photoélectrons dans la coquille de CdS, dont l'amélioration favorise la séparation des paires électron-trou.

Les images en champ clair (*bright field* ou BF) et au HRMET montrent des QD g-CS avec une distribution de taille étroite et un réseau cristallin clair. Le schéma de diffraction électronique en aire sélectionnée (*selected area electron diffraction* ou SAED) en encadré dans la figure R3a montre que les QD g-CS ont une structure cristalline wurtzite (WZ). Avant l'exposition au faisceau de protons, les différents QD présentent un contraste MET uniforme, à l'exception de quelques QD qui contiennent des défauts d'empilement (*stacking faults* ou SF). Après une irradiation de protons de 1×10^{17} H^+/cm^2, le contraste MET des différents QD (figures R3c et R3e) n'est pas aussi uniforme que celui observé avant l'irradiation (figures R3a et R3b). Les images BF et HRMET révèlent toutes deux l'apparition de petites taches blanches, indiquées par des flèches sur les figures R3c et R3e. Cette observation est corroborée par les modulations de l’intensité du contraste au HRMET le long des directions tracées sur chaque image, indiquant des changements significatifs après l'irradiation.

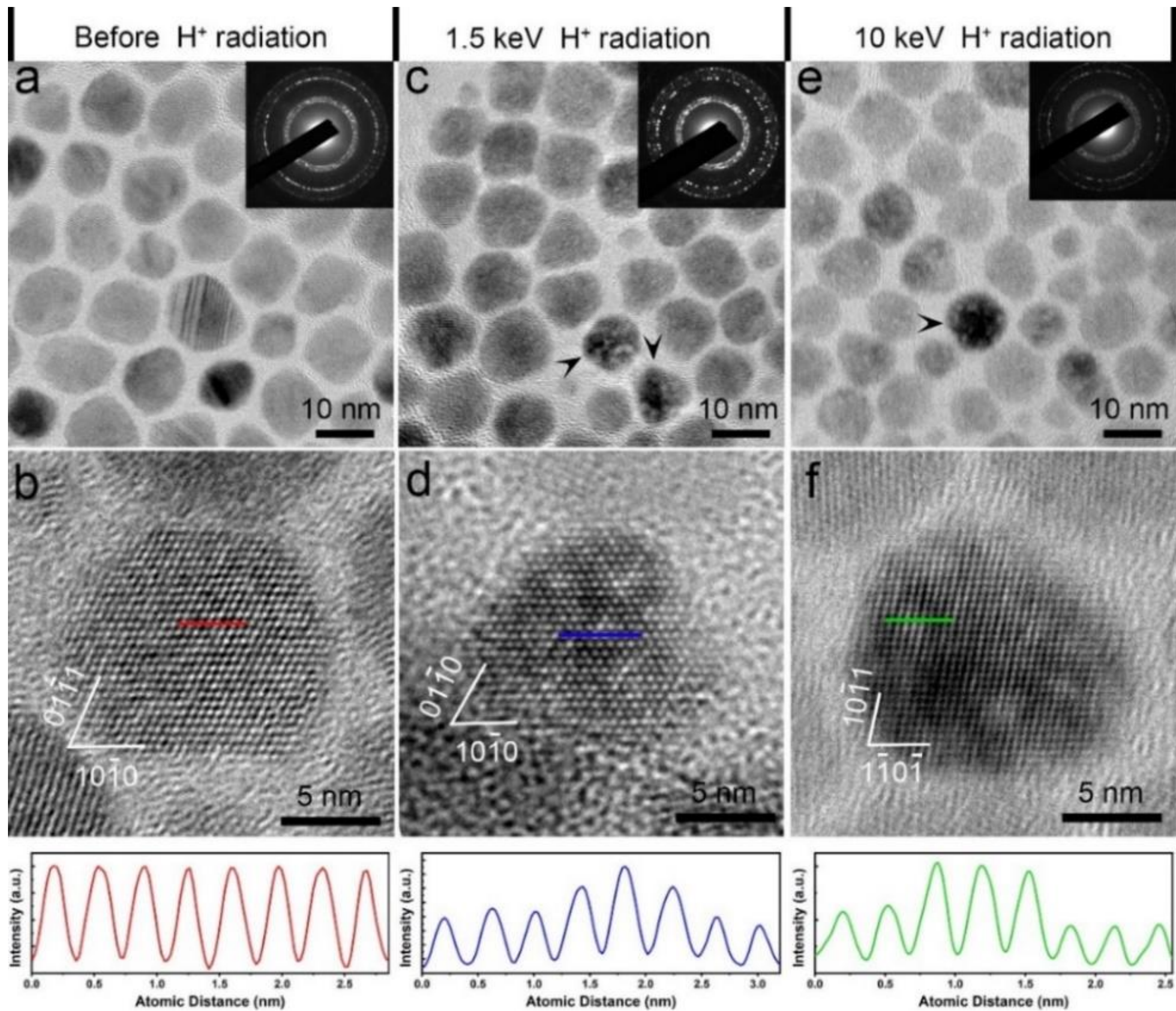

Figure R3 **Images BF, images HRMET et profils d'intensité des QD g-CS : (a) et (b) avant irradiation ; (c) et (d) après irradiation de protons de 1,5 keV à 1×10^{17} H^+/cm^2 ; (e) et (f) après irradiation de protons de 10 keV à 1×10^{17} H^+/cm^2.**

Les figures R4a et R4b montrent les spectres d'absorption et de PL des QD g-CS avant et après irradiation avec des énergies de protons de 1,5 et 10 keV pour des doses d'ions variant entre 5×10^{13} H^+/cm^2 et 5×10^{15} H^+/cm^2. Avant irradiation, tous les échantillons présentent une forte émission de PL avec un pic de PL autour de 627 nm. Dans les figures R4a et R4b, alors que l'intensité de PL des QD après irradiation de protons diminue avec la dose d'irradiation, on ne mesure ni décalage ni changement spectral. Nos observations

mettent également en évidence le fait que la taille et la bande interdite des QD g-CS restent inchangées après l'irradiation. Cela est qualitativement cohérent avec la légère diminution de l'absorbance optique signalée après l'exposition au faisceau de protons. Dans les figures R4c et R4d, l'intensité spectrale normalisée de chaque pic de PL mesuré est rapportée en fonction de la fluence des protons et de la concentration correspondante des sites vacants induits par irradiation dans la coquille du CdS, déterminée à l'aide de calculs SRIM. L'intensité du signal de PL a été obtenue après soustraction de la contribution du bruit de fond optique et l'intégration numérique du pic de PL entre 550 et 750 nm. Comme le montre la figure R4c, l'irradiation de protons de 1,5 keV engendre une réduction légèrement plus rapide de l'intensité de la PL que dans le cas de 10 keV.

La figure R5 est la courbe I-V de l'échantillon avant et après irradiation, les tensions appliquées étant comprises entre 0,0 V et +1,5 V. Pour toutes les expériences menées dans des conditions d'obscurité, le courant direct mesuré passant à travers les systèmes MoO_3/QD/Si ou MoO_3/Si est supérieur au courant inverse. Une diminution des valeurs rapportées est également observée avec l'augmentation de l'exposition au faisceau de protons. Ces deux phénomènes semblent se produire plus rapidement et/ou être plus prononcées pour les implantations effectuées à 1,5 keV que pour celles effectuées à 10,0 keV. Pour les courbes I-V obtenues sous illumination, les mesures diffèrent fortement en présence et en absence de QD g-CS. Deux tendances remarquables et très distinctes ressortent. Premièrement, on ne détecte pratiquement pas de photocourant en polarisation inverse dans les échantillons de MoO_3/QD/Si (côté gauche des figures R5a et R5b), alors qu'un fort courant est observé dans les systèmes MoO_3/Si (côté gauche des figures R5c et R5d). Deuxièmement, alors que tous les photocourants mesurés

diminuent avec la dose de protons dans les MoO_3/Si implantés, on constate que ces photocourants augmentent continuellement avec les fluences de H^+ dans les MoO_3/QD/Si.

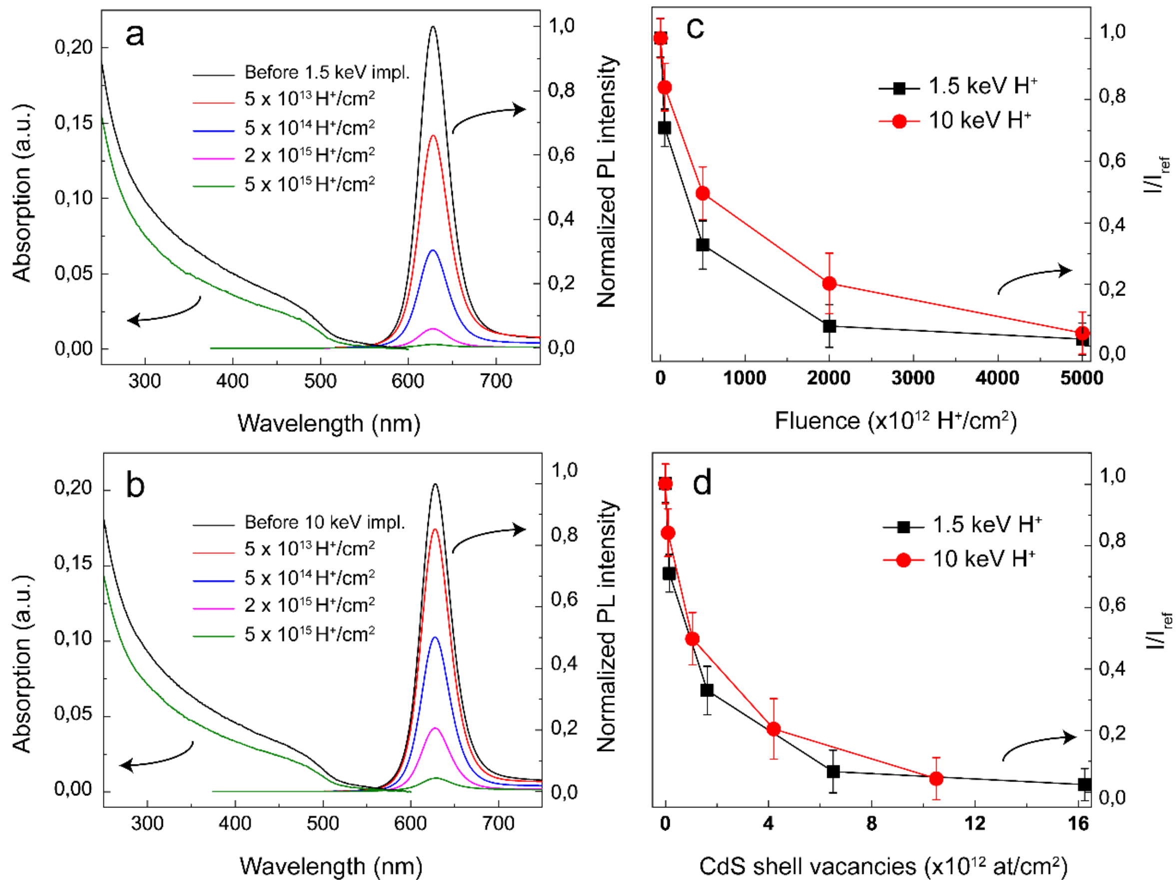

Figure R4 **Évolution de l'absorption et de l'émission spectrale de PL dans les QD g-CS exposés à une irradiation de protons de 1,5 keV (a) et de 10 keV (b), avec la dépendance du signal de PL, intégrée entre 550 et 700 nm, à la dose (c), et tracée en fonction de la variation de la concentration de sites vacants de la coquille de CdS calculée par SRIM (d).**

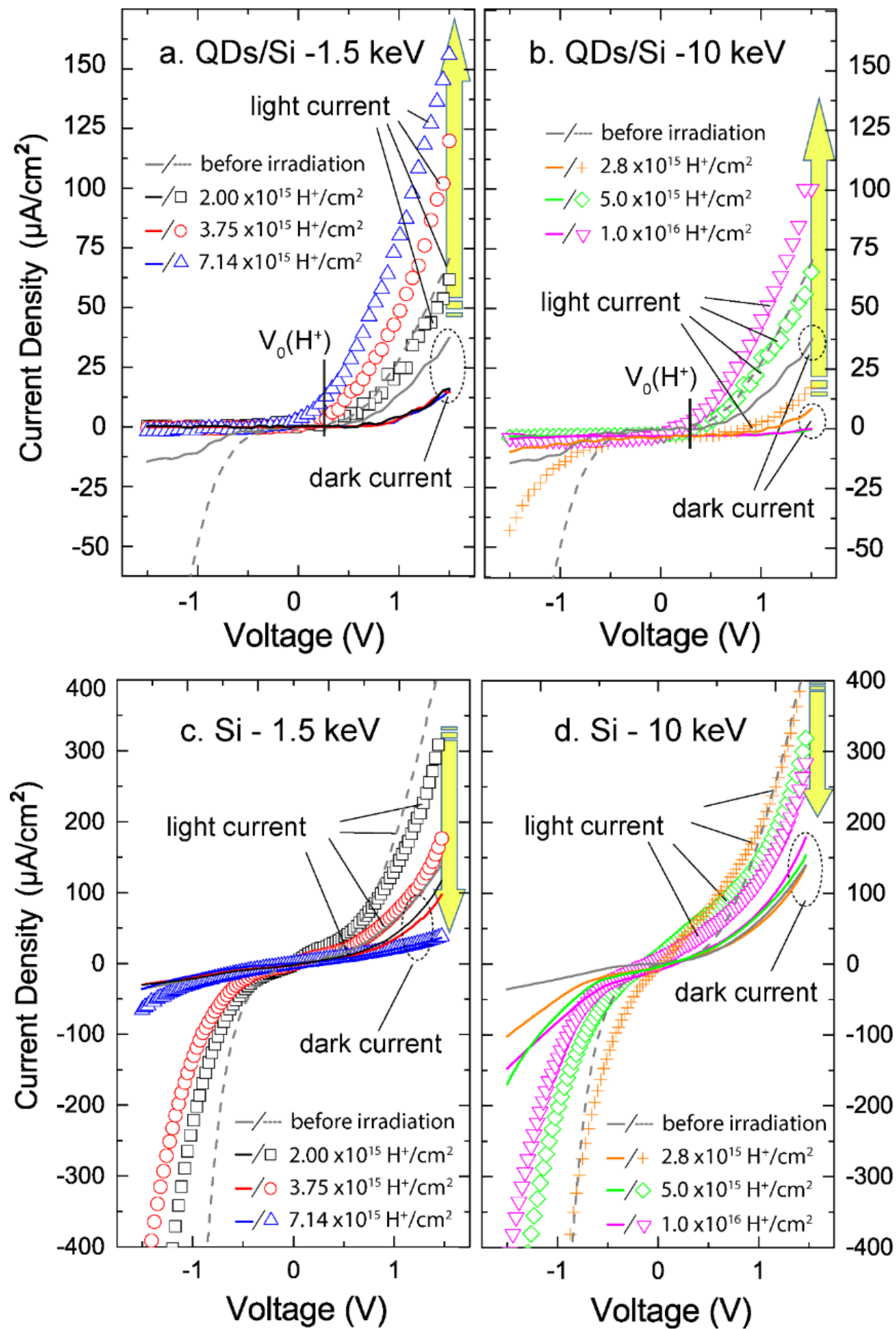

Figure R5 **Caractéristiques I-V des MoO_3/QD/Si et MoO_3/Si dans l'obscurité et sous illumination, pour les QD implantés à 1,5 keV (a) et à 10,0 keV (b) ainsi que pour les substrats de Si implantés à 1,5 keV (c) et à 10,0 keV (d).**

Dans la figure R6a, nous présentons une description complète de l'alignement de la bande interdite qui se produit dans les systèmes MoO_3/QD/Si, sur la base d'études précédentes menées sur des QD g-CS ainsi que des mesures de spectroscopie de photoélectrons UV (UPS) effectuées sur des substrats de silicium avant et après exposition à différents faisceaux H^+. Sur la gauche de la figure R6a, l'hétérojonction de type II entre le MoO_3 et la coquille de CdS des QD est comparable aux interfaces des bandes interdites des couches de TiO_2/CdS et de MoO_3/CdS massif présentées dans la littérature, pour des énergies de bande interdite de 3,1 eV dans le MoO_3 et de 2,7 eV dans le CdS. Une bande interdite indirecte de 1,1 eV est choisie pour illustrer la jonction de type I entre la partie inférieure de la coquille de CdS et la face supérieure de la couche de Si implantée. Sachant que la génération de sites vacants dans le Si implanté augmente la concentration d'états donneurs à l'intérieur du matériau, l'augmentation du niveau de la bande de valence et la légère diminution du travail de sortie de l'échantillon montrées à la figure R6 indiquent que la structure de bande du substrat de Si exposé au bombardement de protons est décalée vers le haut de 0,2 à 0,3 eV par rapport à celle du Si non implanté. La jonction entre la couche de Si implantée (identifié « Si_{H+} » sur la figure) et la région de Si non implantée, située à une profondeur supérieure à plusieurs centaines de nm, est comparée à une barrière d'énergie de type II, tel qu'illustré dans la partie droite de la figure R6a, qui est agrandie dans la figure R6b. Selon les calculs SRIM, l'épaisseur de la couche de Si_{H+} est d'environ 80 nm et 260 nm respectivement pour des faisceaux d'ions de 1,5 keV et de 10,0 keV. Pour l'ensemble du système, l'alignement de la bande interdite est fixé par rapport au niveau de Fermi indiqué par la ligne horizontale pointillée sur les figures R6.

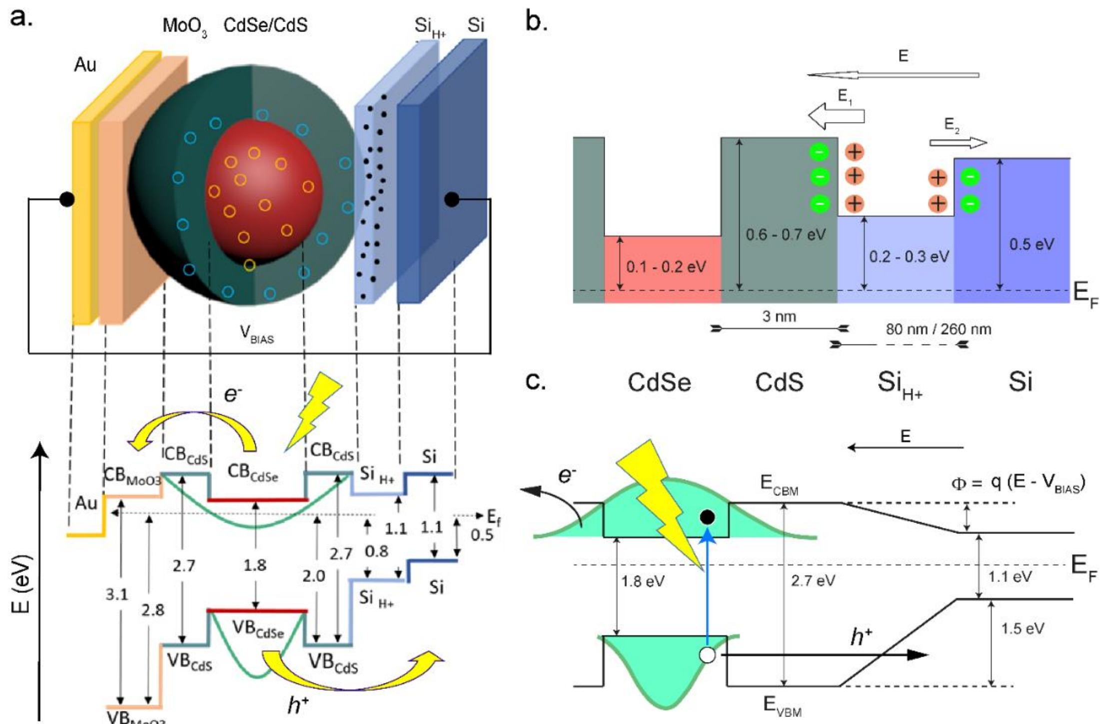

Figure R6 **(a) Alignement schématique des bandes le long du niveau de Fermi dans les systèmes MoO_3/QD/Si contenant des QD g-CS, (b) redistribution des donneurs/accepteurs aux interfaces CdS/Si-H et Si-H/Si engendrant les champs électriques locaux E_1 et E_2. (c) Décalage vers le bas du potentiel équivalent, Φ, obtenu à partir de $E = E_1 - E_2$ et de la tension de polarisation, V_{BIAS}, par le processus photovoltaïque amélioré grâce à la délocalisation des électrons de conduction dans le système g-CS.**

La présence de l'interface CdS/Si_{H+}/Si peut expliquer l'évolution des courbes I-V en polarisation inverse et directe. La valeur inférieure du minimum de la bande de conduction dans la sous-couche de Si_{H+} et la valeur supérieure du maximum de sa bande de valence créent des barrières d’énergie pour les électrons traversant la couche de Si implantée vers la coquille de CdS ou le substrat de Si. Ces barrières génèrent deux champs électriques locaux de directions opposées (appelés E_1 et E_2 sur la figure R6) résultant de l'équilibre des distributions donneur/accepteur le long des jonctions Si_{H+}/Si et Si_{H+}/CdS.

L'interface Si_{H+}/CdS a une barrière d'énergie d'environ 0,5-0,6 eV, soit près du double de celle de l'interface Si-H/Si (~ 0,3 eV). En première approximation, la contribution totale de la redistribution des porteurs de charge à l'intérieur de la couche « tampon » de Si_{H+} peut être approximé sous la forme d'un champ électrique positif, E, orienté perpendiculairement au substrat de Si (figure R6b). Dans la partie droite de la figure R6c, une représentation schématique des hétérojonctions CdS/Si_{H+}/Si est présentée.

Croissance épitaxiale et réparation des défauts des points quantiques

Les points quantiques hétérostructurés (hétéro-QD) présentent des propriétés optiques ainsi qu'une stabilité chimique et une photostabilité exceptionnelles, ce qui rend leur utilisation dans divers dispositifs optoélectroniques très prometteuses. Dans ce chapitre, les hétéro-QD $CuInSe_xS_{2-x}$/CdSeS/CdS ont été synthétisés à l'aide d'une méthode simple en deux étapes. La taille des particules, leurs formes tridimensionnelles (3D) et la relation épitaxiale entre le cœur de $CuInSe_xS_{2-x}$/CdSeS et la coquille de CdS ont été étudiées au HRMET. Nos études prouvent que les hétéro-QD tels que synthétisés ont une forme 3D régulière en tétraèdre avec quatre facettes cristallines $\{111\}$. La relation épitaxiale entre le cœur de $CuInSe_xS_{2-x}$/CdSeS et la coquille de CdS est déterminée comme étant : $[110]_{\text{coeur}}//[110]_{\text{coquille}}$, $\{112\}_{\text{coeur}}//\{111\}_{\text{coquille}}$. Les observations *in situ* au HRMET montrent que les dislocations vis dans les hétéro-QD peuvent être réparées efficacement par irradiation par faisceau d'électrons. Ces résultats pourront aider à concevoir des hétéro-QD avec des interfaces de haute qualité et à identifier des stratégies pour synthétiser des hétéro-QD sans défaut.

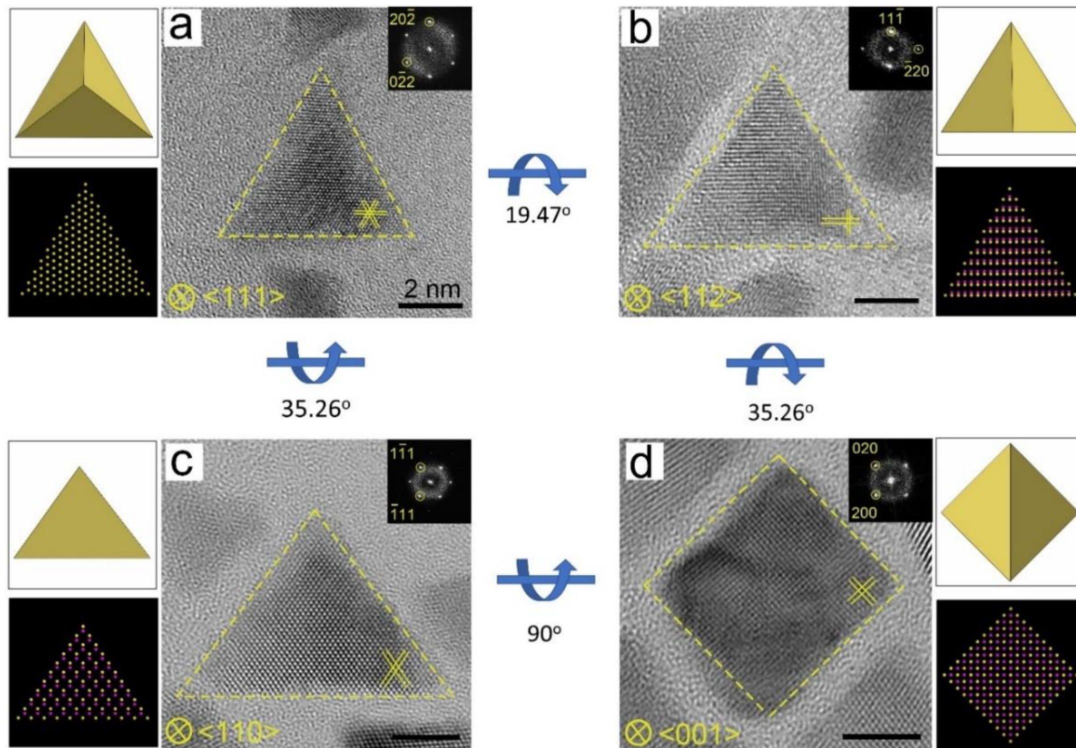

Figure R7 **Images HRMET d'hétéro-QD CISeS/CdSeS/CdS. Chacun des quatre sous-figures (a-d) est composée d'une image HRMET représentative d'un QD isolé dans une projection donnée, des diagrammes FFT (encadré) correspondant à l'image HRMET, d'un croquis et du modèle atomique. Les modes de rotation détaillés entre les axes de différentes zones sont indiqués par les flèches bleues. (a)-(d) montrent les QD visualisés selon les axes des zones <111>, <112>, <110> et <001>, respectivement.**

La figure R7 montre un hétéro-QD ayant une forme de triangle équilatéral et des franges d'interférence atomiques avec une distance interréticulaire d mesurant 2,06 Å, qui est associée aux plans $\{220\}$ du CdS à structure zinc blende (ZB). Cela suggère que cette particule est vue le long de l'axe de la zone [111]. Lorsqu'il est observée le long des axes de la zone [112] et [110], le QD apparaît comme un triangle isocèle dont les sommets forment des angles de 63° et 71° qui concordent avec les valeurs théoriques de 62,96° et 70,5°. La distance interréticulaire d du plan cristallin présenté sur la figure R7 est

respectivement de ~3,36 Å et ~2,06 Å avec un angle de ~90°, pour les familles de plans (111) et (220) du CdS à structure cristalline ZB. La figure R7 montre la particule vue le long de l'axe de la zone [110] et affichant les plans {111}. Les franges d'interférences de cette projection présentent un angle de 71°, ce qui est en accord avec la valeur théorique calculée de 70,5°. Une faible proportion (~10%) de QD est observée avec des projections carrées. Lorsqu'on les observe le long de l'axe de la zone [001], ces particules ont des franges rectangulaires pour les familles de plans {200} avec un distance interréticulaire d mesurant 2,9 Å. En outre, le contour 2D des QD montré dans l'image HRMET et le diagramme de transformée de Fourier rapide (*fast Fourier transform* ou FFT) correspondant concordent parfaitement avec le modèle atomique dans le coin de chaque figure. Ces résultats démontrent et valident expérimentalement sans équivoque la forme 3D des CISeS/CdSeS/CdS, ainsi que leurs facettes cristallines et leurs orientations atomiques.

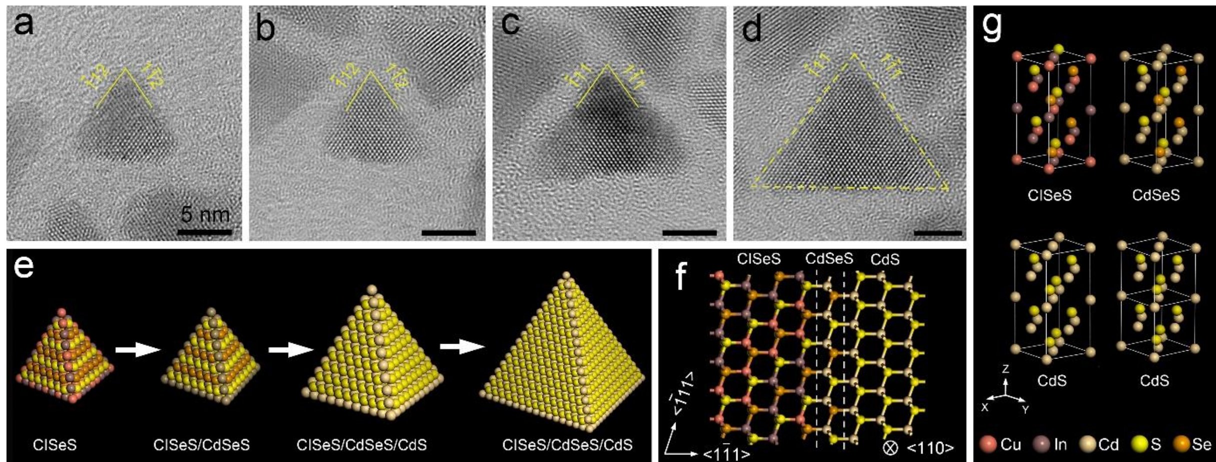

Figure R8 **(a) Image HRMET du cœur de CISeS ; (b-d) images HRMET des hétéro-QD formés à différents stades de la croissance ; (e) modèle atomique des QD à différents stades de la croissance ; (f) l'interface du CISeS, du CdSeS et du CdS, vue selon l'axe de la zone <110> ; (g) montre la maille élémentaire du CISeS, du CdSeS et deux mailles élémentaires du CdS.**

Pour étudier le mécanisme de croissance des hétéro-QD, des produits intermédiaires formés à différents stades de la croissance ont été extraits et observés au HRMET. La figure R8 montre des franges d'interférence atomiques avec une distance interréticulaire d de 3,25 Å, pour les plans $\{112\}$ du cœur de CISeS (PDF nº 00-036-1311). Après l'injection de 2,5 ml de précurseurs Cd/S, une fine couche de CdSeS croît à la surface du cœur de CISeS par le processus d'échange de cations. On constate que la taille des QD diminue légèrement en raison de l'échange de cations aux premiers stades de la croissance. Les franges d'interférence atomiques de la figure R8b sont toujours constituées de structures de CISeS, avec une distance interréticulaire d de 3,3 Å légèrement supérieure à celle mesurée sur la figure R8a (3,25 Å). Une telle expansion résulte de la croissance des CdSeS, dont le réseau présente une distance interréticulaire d plus importante que celui des CISeS. Lorsque le volume du précurseur Cd/S injecté augmente, le dépôt de CdS sur la surface du cœur de CISeS/CdSeS augmente la taille du cristallite synthétisé, comme sur la figure R8c. La taille moyenne des hétéro-QD passe de 6,4 ± 0,5 nm à 7,4 ± 0,5 nm. Lorsque le volume de précurseur Cd/S injecté atteint 20 ml, la distance interréticulaire d est de 3,36 Å, ce qui est égal à la distance interréticulaire d dans le CdS (PDF nº 00-001-0647).

La figure R9a montre un défaut SF et une dislocation vis typiques situés respectivement en haut et au milieu de l'hétéro-QD. Ce type de défaut est endémique dans la structure ZB, en particulier pour les matériaux multicouches de compositions chimiques différentes. Ces structures peuvent conduire à la formation de défauts/pièges de surface qui affectent les propriétés photoélectriques et de luminescence des QD. De nombreux efforts ont été investis pour prévenir la formation de tels défauts dans les QD. Les images

microscopiques enregistrées pour des échantillons exposés à un faisceau électronique de 200 kV pendant les durées indiquées en haut à droite sont présentées à la figure R9. La dislocation vis située au milieu des hétéro-QD a été réparée après environ 15 minutes d'irradiation, tandis que le défaut SF situé en haut demeure inchangé, même après 20 minutes d'exposition au faisceau d'électrons.

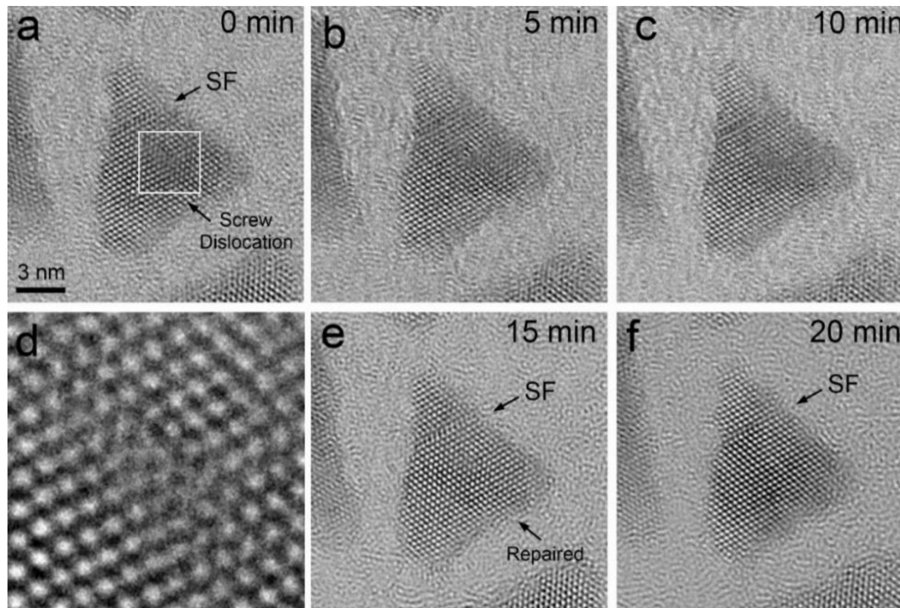

Figure R9 Évolution des défauts lors de l'exposition au faisceau d'électrons, observée au HRMET *in situ* ; (d) correspond à la région encadrée en (a).

Amélioration de la résistance au rayonnement de l'émission de photoluminescence grâce au *nanoclustering*

L'influence du *nanoclustering* de Er et de Si sur l'émission de Er dans le proche infrarouge (*near-infrared* ou NIR) est étudiée dans des échantillons de verre de silice exposés à des faisceaux de protons, utilisés pour reproduire les conditions de rayonnement spatial en OTB. Des verres de silice massifs sont utilisés comme systèmes modèles qui imitent les fibres optiques. Dans ce chapitre, la croissance de *nanoclusters* de Er/Si, synthétisés

dans du verre de silice co-implanté après recuit thermique entre 1000°C et 1200°C, a été analysée au MET et par EDS. Des mesures de photoluminescence de l'émission optique de Er^{3+} indiquent que sa transition $_4I^{13/2} \rightarrow {}_4I^{15/2}$ autour de 1,54 µm peut encore être utilisée pour la communication optique après des doses d'irradiation de protons équivalant à plus de 50 ans d'exposition en OTB. En utilisant un modèle phénoménologique soutenu par des simulations de Monte-Carlo, nos résultats montrent une augmentation du transfert de photoporteurs entre les NC de Si et les niveaux d'émission de Er dans le NIR, ce qui compense partiellement les pertes optiques induites par les dommages structurels. Ces expériences présentent une approche alternative pour développer des sources de lumière Er avancées avec une résistance aux radiations supérieure et des durées de fonctionnement plus longues dans l'environnement spatial.

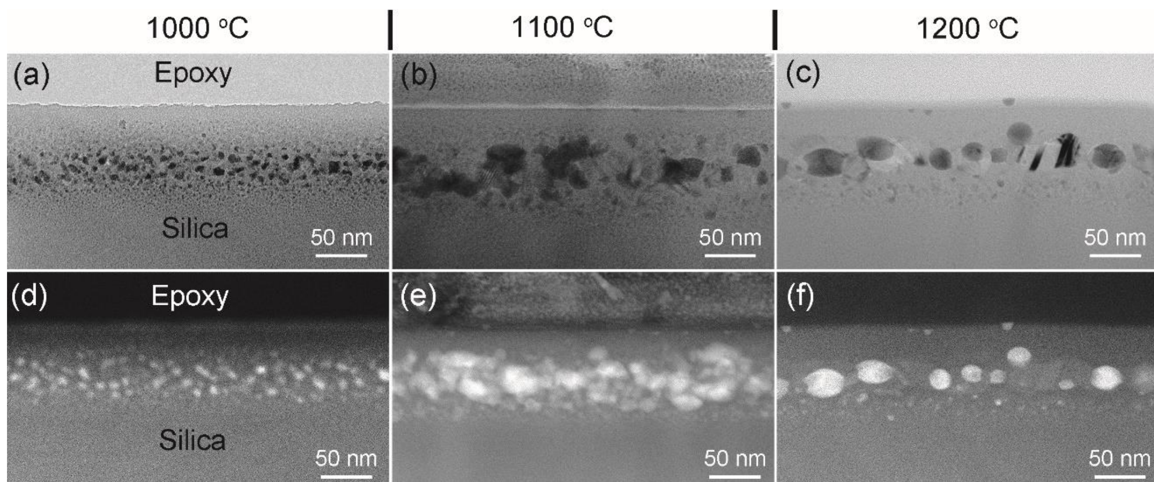

Figure R10 **Images MET BF d'échantillons recuits à 1000°C (a), 1100°C (b) et 1200°C (c) ; avec leurs images MET HAADF correspondantes en (d), (e) et (f).**

Les images BF MET sont présentées aux figures R10a-c et les images HAADF, aux figures R10d-f, pour des échantillons recuits à 1000°C, 1100°C et 1200°C respectivement. À des fins de comparaison, toutes les images en coupe transversale ont

été enregistrées avec le même grossissement. Dans chaque échantillon, des *nanoclusters* à base de Si et de Er ont été observés dans la région supérieure du film de SiO_2 implanté jusqu'à une profondeur de 120 ± 10 nm. Les dimensions moyennes de ces NP ont été déterminées à partir d'une analyse approfondie des images MET, en prenant en compte plus plus de 100 *nanoclusters* observés. Comme le montre la figure R10, le diamètre des *nanoclusters* formés augmente continuellement avec la température de recuit, de 9,9 nm à 1000°C à 25,0 à 1100°C, et jusqu'à 33,0 nm à 1200°C. Une telle évolution de la taille des nanoparticules résulte du phénomène de maturation d'Ostwald et d'effets de coalescence, comme décrit dans de précédents travaux.

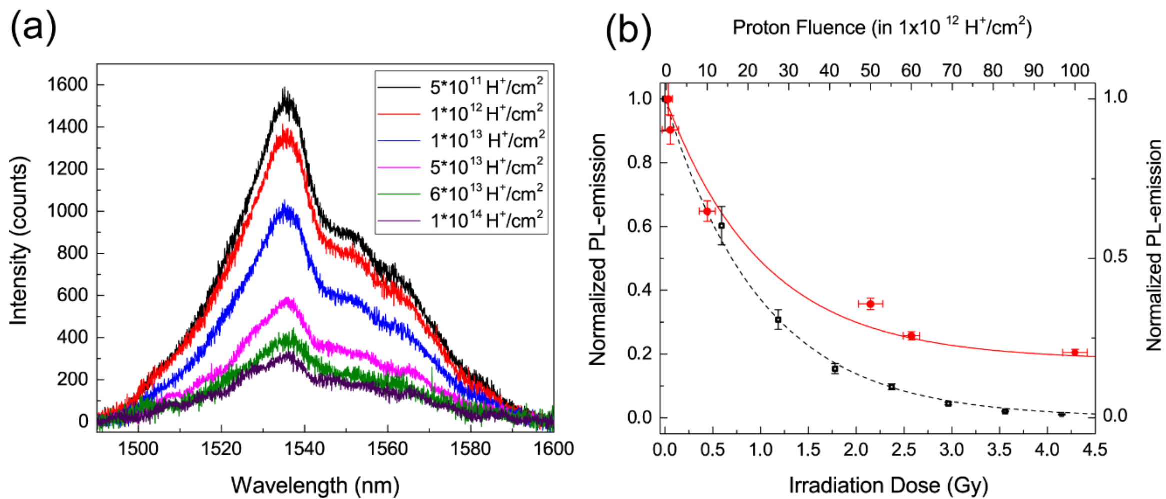

Figure R11 **Évolution de l'émission spectrale de PL NIR des systèmes hybrides Er/Si synthétisés à 1100°C sous irradiation de protons (a), avec la dépendance du signal intégré à la dose (cercles rouges pleins) et la décroissance de la puissance de PL attendue dans les systèmes individuels (carrés noirs vides) (b).**

Des expériences d'irradiation ont été menées sur des échantillons co-implantés de Si/Er recuits à 1100°C. Les spectres de PL dans le NIR en fonction de la fluence de protons sont présentés sur la figure R11a. Une diminution continue du pic à 1,54 µm est observée

en fonction de la dose d'irradiation, jusqu'à 60,4 Gy, qui est calculée pour une fluence de protons de $1,0\times10^{14}$ H^+/cm^2. Les fluences de protons de 5×10^{11}, 1×10^{12}, 5×10^{12}, 1×10^{13}, 5×10^{13}, 6×10^{13} et 1×10^{14} H^+/cm^2 correspondent aux conditions d'irradiation en GEO/OTB pendant ~100 jours, 200 jours, 3 ans, 5 ans, 27 ans, 32 ans et 55 ans, respectivement. Sur la figure R11b, l'intensité spectrale normalisée pour chaque pic de PL mesuré, intégrée entre 1480 et 1600 nm après soustraction de la contribution du fond optique, est rapportée en fonction de l'irradiation de protons (cercles rouges pleins). Ainsi, la diminution de l'émission de PL peut être directement liée aux dommages causés par les protons, responsables de la formation de centres colorés qui entraînent de l'absorption optique. En supposant que le nombre de centres émetteurs diminue selon une séquence géométrique pour une irradiation avec un flux de particules constant, la décroissance du signal de PL devrait suivre une simple fonction de décroissance exponentielle en fonction de l'irradiation. Cependant, l'intensité du signal de PL mesurée dans les systèmes Er-np/Si-nc ne suit pas la tendance prévue de destruction progressive des centres émetteurs lors de l'irradiation. Cela s'explique par le fait que les pertes optiques générées par les protons dans le NIR peuvent être compensées par une plus grande génération de photoporteurs, qui sont transférés du Si-nc vers les niveaux d'émission Er^{3+}: *4f*.